Diélectrophorèse de nanoparticules en système microfluidique étude par vidéo-microscopie numérique et application à l'analyse par spectroscopie optique

Clyde Midelet

UNIVERSITE BRETAGNE LOIRE MATHSTIC

école normale supérieure rennes

THESE DE DOCTORAT DE

L'ECOLE NORMALE
SUPERIEURE DE RENNES
COMUE UNIVERSITE BRETAGNE LOIRE

ECOLE DOCTORALE N° 601
Mathématiques et Sciences et Technologies de l'Information et de la Communication
Spécialité : *Électronique*

Par

Clyde MIDELET

Diélectrophorèse de nanoparticules en système microfluidique: étude par vidéo-microscopie numérique et application à l'analyse par spectroscopie optique.

Thèse présentée et soutenue à Bruz, le 28/11/2019
Unité de recherche: Systèmes et Applications des Technologies de l'Information et de l'Energie (CNRS UMR 8029)

Rapporteurs avant soutenance:

Gaëlle Charron	Maître de conférences, Laboratoire MSC, Université Paris-Diderot
Laurent Malaquin	Directeur de recherche CNRS, LAAS, Toulouse

Composition du Jury:

Président:	Ronan Sauleau	Professeur des universités, IETR, Université de Rennes 1
Examinateurs:	Gaëlle Charron	Maître de conférences, Laboratoire MSC, Université Paris-Diderot
	Laurent Malaquin	Directeur de recherche CNRS, LAAS, Toulouse
	Rozenn Piron	Maître de conférences, Institut FOTON, INSA Rennes
	Bruno Palpant	Professeur des universités, LPQM, CentraleSupélec Paris
Dir. de thèse:	Martinus Werts	Chargé de recherche CNRS, Laboratoire SATIE, ENS Rennes

Remerciements

Je souhaite, tout d'abord, remercier très sincérement mon encadrant de thèse Martin Werts pour son accueil, sa disponibilité, ses conseils, sa bonne humeur tout au long de ces trois années de thèse. Cela a été pour moi un véritable plaisir de discuter tant d'un point de vue scientifique que de choses plus diverses et variées. C'est en partie grâce à tout cela que durant ces trois années j'ai pu m'épanouir professionnellement.

Je souhaite adresser mes remerciements à Ronan Sauleau, d'avoir accepté de juger la qualité de mon travail en participant et en présidant mon jury de thèse. Je remercie tout particulièrement Laurent Malaquin et Gaëlle Charron d'avoir acceptés de rapporter ce mémoire et pour l'ensemble des retours constructifs qu'ils ont pu m'apporter. De même, je remercie Rozenn Piron et Bruno Palpant qui m'ont fait l'honneur d'accepter d'évaluer ce travail de thèse.

Je tiens aussi à remercier particulièrement l'ensemble des personnes qui ont accompagné ces trois années à l'ENS Rennes. Je remercie tout particulièrement les personnes du département de mécatronique. Encore plus particuliérement je tiens à remercier mes anciens collègues doctorant et post-doctorant: Antoine, Melaine, Amaury, Pierre D., Pierre P., Donatien, Thomas, Gurvan, Marvin, Tsung, Nitin, Lancelot.

Je tiens aussi à remercier les personnes avec qui j'ai pu travailler durant divers projets de recherche, Johanna Midelet, Anne Débarre, Guillaume Laurent, Bruno Le Pioufle, Wolfgang Fritzsche, Andrea Csaki, Sophie Thamm, Andreas Kleiber, Lisa Stolle. "Danke"

Je remercie aussi tout simplement mes amis pour leur soutien et leur joie de vivre. Ils se reconnaitront.

Enfin, je souhaite terminer cette partie en remerciant mes parents ("Les petits parents"), mon grand frère Christopher ("Grandaim"), ma grande soeur Johanna ("Patafoin") ainsi que leurs belles pièces rapportées Dr.Alastair et Anne. Je remercie enfin tout spécialement Coralie Verdier pour tout ce qu'elle m'apporte, notamment depuis que j'suis avec toi le soleil renaît dans ma vie.

Publications in relation to this thesis

Parts of the work in this thesis have been published in peer-reviewed journals.

Publications related to chapters of this thesis:

[1] **Midelet C.**, Le Pioufle B., Werts M. H. V. Brownian motion and large electric polarizabilities facilitate dielectrophoretic capture of sub-200 nm gold nanoparticles in water. ChemPhysChem, **2019**, 20, 3354.

[2] Chen C., **Midelet C.**, Bhuckory S., Hildebrandt N., Werts M. H. V. Nanosurface Energy Transfer from Long-Lifetime Terbium Donors to Gold Nanoparticles. J. Phys. Chem. C, **2018**, 122, 17566–17574.

[3] **Midelet C**, Lin J.-Y, Tsang S, Sun C.-L, Midelet J, Kanaras A. G, Le Pioufle B, Français O, Werts M. H. V. Effects of Biomolecules on the Electrokinetics of Colloidal Nanoparticles in Liquid Suspension. Proc.SPIE, **2017**,10078, 100780T.

Publications related to techniques used in this thesis:

[4] Loumaigne M., **Midelet C.**, Doussineau T., Dugourd P., Antoine R., Stamboul M., Débarre A., Werts, M. H. V. Experimental Determination of Optical Extinction and Scattering Cross Sections of Plasmonic Nanoparticle Dimers in Aqueous Suspension. Nanoscale, **2016**, 8, 6555–6570

Résumé en français

Cette thèse s'inscrit dans les domaines de la microfluidique et de la bio-nanotechnologie. Elle vise le développement de méthodes pour extraire des informations sur l'état chimique et biologique d'un échantillon donné. Elle concerne l'étude du comportement de nanoparticules métalliques individuelles soumises à des champs électriques, à l'échelle microscopique, caractérisées par spectroscopie optique. L'objectif ultime serait de construire un système permettant la détection de très faibles quantités de biomarqueurs en solution dans un système microfluidique.

La science et les avancées technologiques ont permis de façonner et d'étudier des matériaux à l'échelle nanométrique. À cette échelle de nouvelles propriétés électriques,[1] optiques[2] et catalytiques[3] apparaissent en comparaison aux matériaux bruts. Les techniques de synthèse et de caractérisation de nanoparticules améliorent les connaissances et ouvrent la voie vers des applications dans des domaines divers comme la médecine (produits de contraste, ciblage de cellules cancereuse),[4] les systèmes nano-électromécanique,[5] ou bien encore les technologies de commmunication (nanoparticules pour écran OLED).[6]

Les nanoparticules individuelles peuvent être utilisées comme des briques de base pour la construction de structures plus grandes et complexes possédant des propriétés spécifiques. Les possibilités sont quasi infinies suivant l'organisation des particules en deux ou trois dimensions, ouvrant la porte à de multiples applications. Pour cela, il est important de contrôler la manipulation de la particule unique afin de créer et

manipuler à son tour un ensemble consistant de plusieurs particules. Les approches pour arriver à cet objectif peuvent être classifiées en deux catégories.

La première catégorie concerne la manipulation "active" de nanoparticules individuelles, utilisant des champs de force externes comme par exemple le piègeage optique,[7] magnetique,[8] ou électrique. En particulier, les champs électriques permettent des manipulations très diversifiées dépendantes du champ appliqué. Des champs électriques continus (appliqués à des particules chargées) ou des champs alternatifs (appliqués à des particules neutres) conduisent à différents phénomènes. Cela permet la création de force d'électrophorèse et de diélectrophorèse utiles à la manipulation des nanoparticules. La diélectrophorèse génére le mouvement des nanoparticules polarisable par l'utilisation d'un gardient de champ électrique. Pour illustrer cela, il peut être cité les travaux permettant de déposer des particules en couches atteignant une épaisseur du diamètre de la particule unique par nanoxerography.[9] Mais aussi, la création de nanofils formés par des particules,[10] ou des dépôts multi-couches complexes.[11] Ou bien encore, de la rotation contrôlée de nanoparticules en milieu liquide.[12] Ces effets ne sont présents que si le champ externe est actifs: ces effets peuvent donc être considérés comme réversibles.

La deuxième catégorie d'organisation de nanoparticules est de former des assemblages complexes de nanoparticules controlés par auto-assemblage.[13, 14] La reconnaissance biomoléculaire est un outil puissant pour l'auto-assemblage et permet de former des assemblages stables. Certaines particules possédent la particularité d'être fonctionnalisées en surface par des molécules biologiques. Cela permet leur auto-assemblage par reconnaissance biomoléculaire. Dans ce cas, le défi est de construire des structures bien définies ayant des propriétés supplémentaires comparées à la particule unique. Ceci nécessite de bien caractériser les objets formés en solution avec des techniques

simples.

Dans ce cas la spectroscopie couplée à la microfluidique pourra s'avérer très utile pour étudier les nanoparticules d'or en solution dans la fenêtre optique de l'UV-visible-NIR.[15]

Cette thèse est orientée vers l'analyse et la détection par microscopie optique et spectroscopie de nanoparticules en système microfluidique sous l'influence du champ électrique. Un système electromicrofluidique est adapté à un microscope inversé. Deux techniques de suivi de particules ont été développées, la videomicroscopie par champ sombre et la spectroscopie d'extinction. Le suivi du piègeage de particules d'or est alors réalisé pour des tailles inférieures à 200 nm dans un champ électrique alternatif.

L'état de l'art sur les principaux points utilisés dans ce travail est décrit dans le chapitre 2. La littérature sur les micro- et nano systèmes est extrêment riche. J'ai choisi de me limiter aux points essentiels, et de viser notamment les travaux menés sur les nanoparticules d'or.

Le chapitre 3 introduit la caractérisation de nanoparticules d'or de formes variées par spectroscopie optique.[2, 15, 16] La spectroscopie optique (extinction et diffusion de lumière) a d'abord servi à étudier la stabilité des suspensions colloidales dans différentes solutions tampon. Additionnellement, la spectroscopie par photoluminescence a été utilisé pour étudier l'interaction biotine-streptavidine-terbium à la surface de nanoparticules d'or. Il en a été deduit que les biomolécules à la surface interagissent entre elles mais cette intéraction ne conduit pas à la création d'assemblages complexes

avec plusieurs nanoparticules d'or.

Le chapitre 4 décrit la création et la reproductibilité de fabrication d'un système électro-microfluidique installé sur un microscope optique inversé. Le système permet la mesure d'analytes en solution via différentes voies d'illumination (champ sombre ou champ clair) et différents moyens de détection (videomicroscopie, spectroscopie). Ce système est de permet l'application d'un champ électrique alternatif non uniforme dans un canal microfluidique pour étudier la force diélectrophorétique appliquée à des nanoparticules en solution aqueuse.

Le chapitre 5 décrit l'utilisation du système électro microfluidique pour l'analyse de la diélectrophorèse de nanoparticules par videomicroscopie en champ sombre. La réponse diélectrophorétique des nanoparticules d'or soumises à un champ électrique non uniforme est analysée. Ces particules sont piégées au niveau des électrodes lorsqu'un champ électrique est appliquées. Le système a été préalablement validé par l'étude des réponses en fonction des fréquences du champ appliqué des nanoparticules de latex. Celles-ci bien connues dans la littérature.[17] Une simulation décrivant le mouvement Brownian et la capture par diélectrophorèse a été développé pour être comparée aux données expérimentales pour des particules de taille comprise entre 80 nm et 150 nm. Cependant, cette méthode est limitée à des particules ayant des sections efficaces de diffusion assez importantes pour pouvoir être détectées.

Le chapitre 6 une autre méthode combinant la diélectrophorèse et la spectroscopie d'extinction optique dans un microcanal. Grâce à cette méthode nous pouvons analyser la diélectrophorèse de particules d'or de plus petites tailles (jusqu'à 40 nm). Cette technique a été comparée et valide le résultat du chapitre 5. Une solution contenant

un mélange de particules d'or de 40 nm et de 80 nm a aussi été étudiée. Cela a permis de démontrer qu'il est possible via cette méthode de différencier deux entités mélangées dans une solution grâce à la modulation en concentration des deux entités par diélectrophorèse.

Les principaux résultats de ce travail donnent des informations sur le comportement de nanoparticules d'or sous l'influence de forces diélectrophorétiques.

Dans un premier temps, une étude spectroscopique de la stabilité de nanoparticules d'or fonctionnalisées en surface par des molécules de biotine dans différentes solutions tampon a été menée. Cela dans le but d'étudier l'intéraction de ces particules avec des molécules de streptavidine liées à des atomes de terbium. Cela dans le but de déterminer ou non de leur auto-assemblage par intéractions inter-moléculaire. Il a été constaté uniquement un greffage en surface des streptavidines sur les nanoparticules d'or.

Suite à cela la fabrication d'un système permettant l'application de champs électriques en microcanal a été réalisée, démontrant une bonne reproductibilité notamment les étapes de microfabrication.

La videomicroscopie par champ sombre a été ensuite utilisée pour mettre en évidence la linéraité de la susceptibilité diélectrophorétique des nanoparticules d'or ($\geq$ 80nm) en fonction de leur diamètre.

Enfin la spectroscopie en microcanal a permis d'étudier cette même susceptibilité pour des particules inférieures à 80 nm de diamètre. L'utilisation de cette technique pour permettre la décomposition de solutions complexes grâce à la diélectrophorèse a été aussi démontrée.

Table of contents

List of figures

List of tables

Nomenclature

ϕ_{cap} Dielectrophoretic capture ratio

a nanoparticle radius

$R_{capture}$ radius of the dielectrophoresis capture area under analysis

$R_{depletion}$ radius of the dielectrophoresis depletion area under analysis

E electric field (vector field)

AC alternating current

AFM atomic force microscopy

AuNP(s) gold nanoparticles

CMF Clausius-Mossotti factor

FG function generator

fps frames per second

ITO indium-tin oxide

NSET nanosurface energy transfer

PCB printed circuit board

PDMS poly(dimethylsiloxane)

RLS resonant light scattering

rpm rotations per minute

Tb-sAv terbium-labelled streptavidin

UV ultra-violet

Chapter 1

Introduction

Progress in science and technology has provided the tools to shape and to study materials at the nanometric scale. At this level, new electrical,[1] catalytic[3] and optical[2] properties are discovered compared to bulk materials. The synthesis and characterisation of nanoparticles makes it possible to enrich the knowledge and potential applications in a myriad of specialised fields, including medicine (contrast agents, targeting of cancerous cells)[4] nano-electromechanical systems (NEMS),[5] and communication technologies (nanoparticles for OLED screens).[6]

Recently, a new system called "programmable atom equivalent" has been proposed. Within this system, nanoparticles are considered to be like atoms and can be organised in a periodic table according to composition, shape and dimensions.[18] These objects can be used as building blocks to assimilate into larger structures which exhibit unique properties. Due to the quasi-infinite possibilities for organisation in either two or three dimensions, there are many possibilities for applications.[19–21]

The controlled manipulation of single particles for creating increasingly complex entities is still a challenge. Methods for achieving this goal can be divided into two

different approaches.

The first approach is the "active" manipulation of individual nanoparticles using external fields such as optical trapping[7], a magnetic field or[8] electric fields.[22, 23] Particular electric fields offer varying possibilities depending on their types. Continuous electric fields (applied to charged particles) or alternating electric fields (applied to neutral particles) have different effects on nanoparticles properties. This allows the creation of electrophoresis and dielectrophoresis forces which are useful for the manipulation of small nanoparticle assemblies. An example of this is the precise deposition of a single layer of particles.[9] It is also possible to create nano-electronic structures ("nanowires"),[10] or complex multi-layered deposits,[11] as well as the monitored rotation of nanoparticles in solution.[12] With this first approach, external perturbations are applied with time limits. This is a key element on the resultant product realised. Furthermore, these changes can be reversible, depending on the external forces. Here, the challenge is to understand the physical phenomena underlying these forces.

The second route, using self-assembly, allows more complex assemblies of several nanoparticles to be created in a controlled and designed manner. Bio-molecular recognition is an example of self-assembly and is a useful tool which ensures the stability of assemblies. Some particles have the advantage of being easily functionalised on their surface by biological molecules (*e.g.* streptavidin, biotin or DNA). This allows their self-assembly by bio-molecular recognition.[13, 14] Another potential application which has been developed by active manipulation of nanoparticles includes the fluorescence quenching of a fluorophore link to the surface of gold particles.[24] Other methods are based on the use of the bulk materials properties, for example, magnetic hydrogel particles for the observation and manipulation of micro-assemblies.[25] With these

methods, assemblies are mostly non reversible. In this case, the challenge is to build well defined structures showing extra properties compared to single objects. Allowing the discrimination of entities in solution with simple technical characterisations.

Understanding and manipulating these assembly mechanisms may give rise to new applications. To do this, the development of specific systems and analytical methods to measure physical and chemical properties are required. Parallel to particle manipulation and synthesis of particle assemblies, detection and characterisation techniques should be developed. Spectroscopic measurements are very useful for the characterisation of gold nanoparticles. Solutions containing assemblies can be characterised using their optical properties in the UV-visible-NIR region of the electromagnetic spectra.[15]

This thesis is in the domains of microfluidics and bio-nanotechnology. The aim is to develop methods for extracting information on the chemical and biological state of microfluidic samples (*e.g.* the presence of biomarkers) by analysing the behaviour of individual metallic nanoparticles injected into the sample. These particles are characterised by their optical signal and their response to the microscale electric field.

This thesis can be split in three different parts of study. The first part is the interaction of gold nanoparticles with biomolecules and the second is the assembly of particles using bio-recognition. Both parts give information on colloidal stability and on bio-interactions. The third (and largest part) part is the study of samples in a microfluidic channel using an electric field to manipulate particles. This part gives information on the susceptibility of metallic nanoparticles to be controlled by an electric field. This part develops a specific analysis method, using spectroscopy in a microfluidic system and videomicroscopy using dark field illumination. The ultimate

goal is to develop a microfluidic system coupled with micro-electrodes, in which analytes can be detected in minimal quantities of sample bio-assay using gold nanoparticles functionalised with biomolecules may be realised in this manner. (see Figure 1.1)

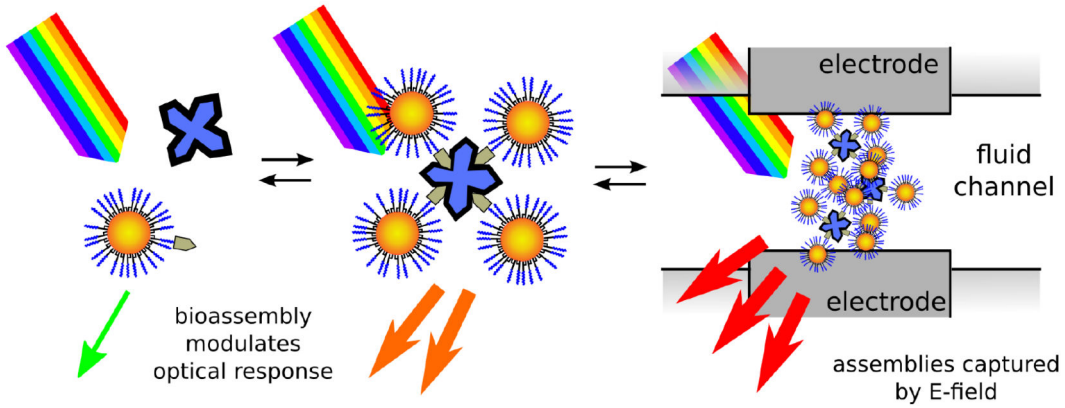

Figure. 1.1 Example of potential biosensing scheme that may be realised using knowledge developed in this thesis.

This chapter is followed by six additional chapters.

Chapter 2 describes the scientific background and main principles used for this work.

Chapter 3 introduces the characterisation of different shapes of gold nanoparticles using spectroscopic techniques such as extinction, light scattering and photoluminescence. Furthermore, these techniques were employed to study the biotin-streptavidin biomolecules interaction on the surface of gold nanoparticles.

Chapter 4 describes an electromicrofluidic system installed on an inverted optical microscope. The main goal of this system was to explore the dielectrophoretic forces for nanoparticles.

Chapter 5 investigates the use of the set-up described in Chapter 4 to analyse the response of gold nanoparticles subjected to dielectrophoretic forces. This system was first validated using spherical latex particles whose DEP response is known. A

physical model describing Brownian motion and DEP was developed to analyse the experimental data for dielectrophoresis on sub-200 nm particles.

Chapter 6 introduces the combination of dielectrophoresis and optical spectroscopic analysis of particles in a microfluidic channel. This leads to a new powerful analytic method for analysis of more complex systems containing several sizes of gold nanoparticles.

A summary of the results obtained in this thesis and suggestions for future work are described in Chapter 7.

Chapter 2

Nanoparticles and microfluidics

This chapter summarises the current applications of nanoparticles in microfluidic systems, particularly potential ways to manipulate and organise these small particles with high precision. First we will revisit nanoparticles, and the specific properties and potential applications they offer compared to bulk materials. One purpose of this thesis is to understand the behaviour of nanoparticles in liquid medium, in order to find a way to capture them and to measure their optical properties at the same time. This yields analytical information on the structure of nanoparticles, their state and their liquid environment. It also provides opportunities to use these nanoparticles as "colloidal sensors" which can recognise and quantify analytes in small liquid samples. This may have application in *in vitro* medical diagnostics.

2.1 Micro- and nanoparticles

Particles with sizes in the 10 nm ... 10 μm range have been produced and can be created at will by chemical or physical processes. Their sizes are comparable to the sizes of biomolecular entities such as proteins and viruses. (see Figure 2.2) They show particular optical,[26] electrical,[27] and catalytic properties.[28–30] On one hand, they

offer opportunities for the development of materials for applications. On the other hand, micro- and nano particles might (in certain cases) constitute a serious danger for human health and the natural environment, as illustrated by the unfortunately famous example of plastic degradation to small particles (microplastics and nanoplastics) dispersed in the oceans and seas.[31]

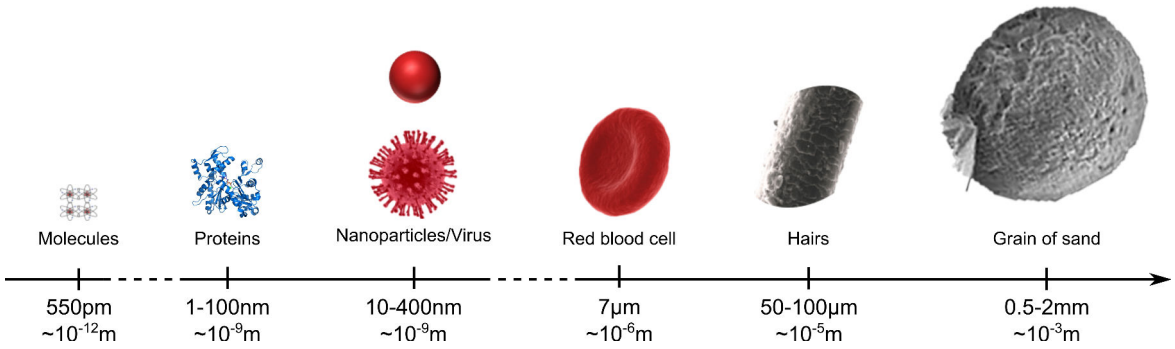

Figure. 2.1 Scale of nanoparticles compared to biological entities and objects of our scale scope.

2.1.1 The structure of nanoparticles

The synthesis of small particles is now a mature field; many shapes and sizes are now accessible.[32–36] In most cases, however, the particles are spherical. This is explained by physical explanations: the spherical shape minimises the surface energy. Synthetic approaches can be divided into two categories "bottom-up" (from atoms and seeds to the particle) or "top-down" (from the bulk material to the particle).

There is a large variety of synthetic methods as a function of the particle type. For instance, polystyrene nanoparticles are synthesised by emulsion polymerisation,[37] emulsifier free polymerisation,[38] and dispersion polymerization.[39]

Chemical precipitation methods are used to synthesise particles such as cadmium sulfide (CdS) in aqueous solution.[40]

Redox reactions are used to synthesise particles such as gold nanoparticles. The most famous examples are the Brust-Schiffrin,[41] the adapted Turkevich method,[42] and the seeded growth method.[43]

This illustrates that there is a large variety of different nanoparticles and synthesis methods as a function of the composition, size and shape of particles.[44] (see Figure 2.2)

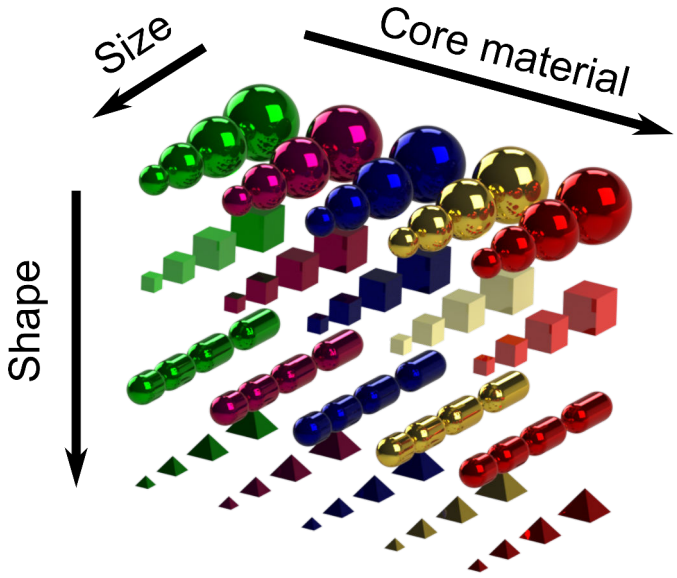

Figure. 2.2 Schemes of particles organised as bulk materials, size and shape.

The system in the Figure 2.2 describes classification particles for cores composed of one material. It is possible to make more elaborate particles, named "core-shell" particles. These are a class of particles which contain a core and a shell. The core particles are synthesised first and the shell is then formed on the core particle via different methods, depending on the type of core and shell materials and their morphologies.[45] Core–shell particles are usually synthesized by a two-step or multi-step process.

The core and the shell can be different materials or the same materials with different structures. Figure 2.3 resumes the schematic representation of core shell particles structures. The core may be a single sphere (Figure 2.3 a)) or an aggregate of several

small spheres (Figure 2.3 b)). The shell structure can be a continuous single atomic layer or can contain multiple shells. (Figure 2.3 c))[46–48] It can also be an attachment of smaller spheres onto a big core sphere. (Figure 2.3 d))[49] Both the core and the shell can be non-porous solid or have desirable porous structures. The size of the core particle, the shell thickness and the porosity in the shell are tuned to suit different types of chromatographic applications.[50]

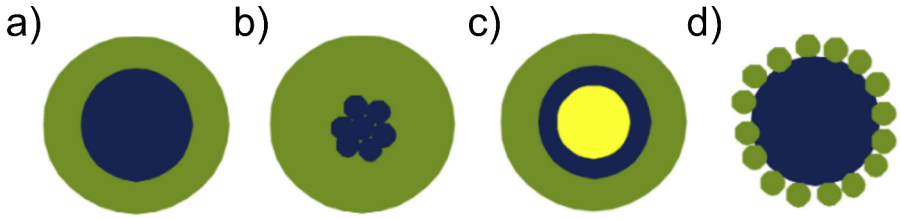

Figure. 2.3 Schematic representation of different types of core–shell particles. The core and the shell are illustrated in different colours.

These complex structures display phenomena such as photonic up-conversion,[51] or can be biodegradable and have the possibility to deliver medically active molecules inside the human body.[52]

Particles have high volume/surface ratio showing an interesting feature. They present the possibility of being coated with molecules following different interactions (covalent, ionic, Van der Waals). The surface of gold nanoparticles in water is considered to be of negative charge due to the charges of $AuCl_2^-$ ions. Similarly, citrates can contribute to a negative surface charge when synthesised using, other methodologies.[53] The surfaces of gold nanoparticles can be coated with different types of ligands such as amines, carboxylic acids, phosphines or thiols. Specific exchange mechanisms give the possibility to replace ligands at the surface of particles without deterioration of the sample. The structure of the molecular coating of nanoparticles can be schematised as in Figure 2.4.

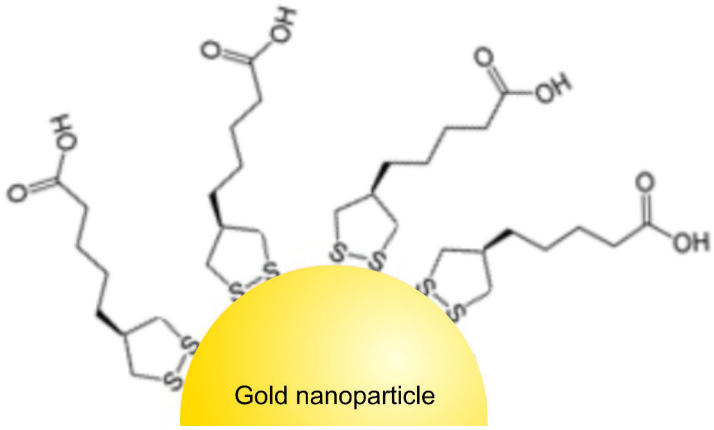

Figure. 2.4 Schematic of a gold nanoparticle and its molecular coating on the surface, in this case lipoic acid molecules.

Thiol ligands are often used in combination with gold nanoparticles because of the affinity of the thiol group to gold, offering a good stability of particles in solution.[54–56]

2.1.2 Classification of nanoparticles according to the electrical properties of their core material

Nanoparticles can be organised as a function of the electrical properties of their core materials. they are organised in three categories: insulating particles, semi-conducting particles and conducting particles. Figure 2.5 illustrates the band structures of these different types of materials.

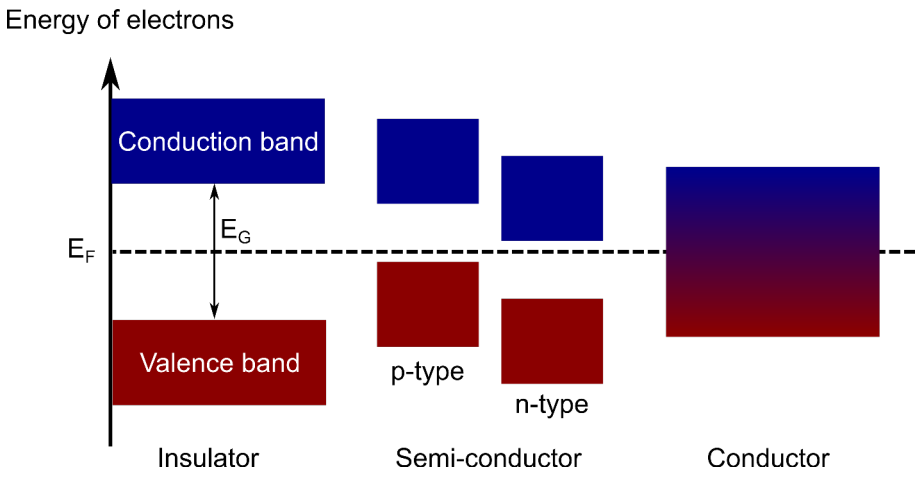

Figure. 2.5 Schemes of the valence band (E_0) and the conduction band for an insulator, semi-conductor and conductor. The Fermi level (E_F) is represented with a dotted line, this last is highly dependent on the temperature. E_G is the band gap energy between the valence band and the conduction band.

Insulating materials have a low dielectric permittivity and conductivity: they do not display electronic transition in the optical spectrum, and are not intrinsically photoluminescent. Examples of insulator nanoparticles are polystyrene latex spheres,[57] PMMA nanospheres,[58] and inorganic materials such as silica (SiO2).[59] These particles may be made luminescent by doping them with luminescent centres,[60] or by adding fluorescent dyes.[61]

Semi-conducting materials are based on crystalline insulating materials (such as silicon), to which impurities are added in a controlled manner ("doping"). Semiconductors doped with donor impurities (excess in electrons) are called n-type, while those doped with acceptor impurities (deficit in electrons) are known as p-type. Often used, semi-conducting nanoparticles (also called "quantum dots") can have varied compositions and properties.[62] Semi-conducting particles, are most famous for their photoluminescence. An example of these are quantum dots of CdSe that show a variability of the electronic band gap (E_G) as a function of the particle size. By decreasing the size of the particle, the band gap increases, which induces a blue-shift in the photoluminescent

spectra.[63] These particles can be detected at very low concentration in liquid.[64] Other types of semiconductor particles (*e.g.* TiO_2 or ZnO) is solar-to-chemical energy conversion.[65–67]

Conducting materials have high dielectric permittivities and conductivities. Conductor nanoparticles and more precisely metallic nanoparticles show interesting optical properties, due to specific resonance in their interaction with an electromagnetic wave.

The work in this thesis mainly focuses on nanoparticles with a golden core. We will discuss the electromagnetic properties below.

2.1.3 Interactions with light

In the case of metallic nanoparticles (*e.g.* gold), the conduction electrons oscillate due to the interaction with an electromagnetic field (light). At a specific frequency, this resonance is called the plasmon resonance. This gives rise to optical effects: light scattering and light absorption. (see Figure 2.6)

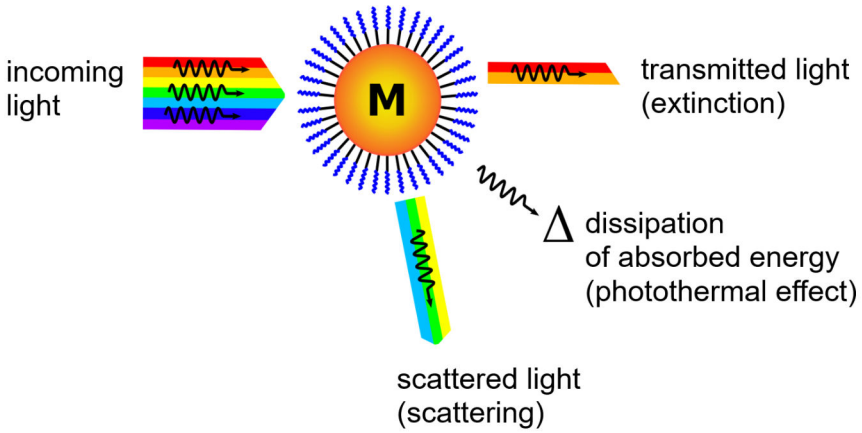

Figure. 2.6 Scheme of a metallic particle illuminating with white light showing the energy transfer as excitation and scattering light.

Applying energy conservation with respect to the incoming light, extinction is given as the sum of the light absorption and the light scattering. Extinction and

scattering spectra of gold nanoparticles are characterised by one or multiple bands in the UV-visible-NIR window. Various optical and spectroscopic measurements can be done to characterise the physical properties of nanoparticle:

- UV-Vis extinction spectroscopy to measure the extinction cross section as a function of the wavelength;
- dynamic light scattering (DLS)[68, 69] to measure the size dispersity of the colloidal suspension;
- resonant light scattering (RLS)[2, 70] spectroscopy to measure the light scattering cross section as a function of the wavelength.

2.2 Colloidal dispersions

Many nanoparticles can be readily dispersed in a liquid solution, as exemplified by dispersions of gold nanoparticles in a liquid. (see Figure 2.7)

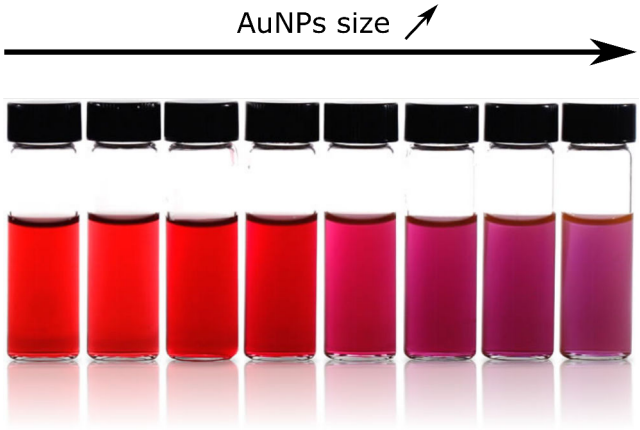

Figure. 2.7 Photo of gold nanospheres with different diameters in solution

Having a liquid environment for nanoparticles is common and practical. Particles are often synthesised directly in a liquid medium. This permits stocking of particles for a long time while avoiding aggregation into bigger clusters.

2.2.1 Electric double layer

In general, a surface immersed in an aqueous solution carries a net electrical charge which comes about either through dissociation of the chemical groups on the surface or by adsorption of ions or molecules from the solution onto the surface. This also holds for the surface of nanoparticles. As an example, gold nanospheres are negatively charged by the presence of negative ions on their surface.[71] The negative or positive charges create an electrostatic potential Φ_0 surface. When a particle or an electrode is immersed in an electrolyte, the surface charge is balanced by an equal amount of opposite charges in the solution near the surface. The net result is that the counter charge from the solution effectively screens the surface charge so that for a macroscopic observer the particle and its surrounding solution is electroneutral.

The surface electrostatic potential leads to the attraction of ions of opposite charge (counterions) from the solution and repulsion of ions with the same charge (co-ions). Very close to the surface, the counter ions are firmly bound. This very thin layer near the surface is generally referred to as the Stern layer.[72] Further away from the surface there is still a higher density of counterions and a lower density of co-ions than the bulk. This layer is called the diffuse layer. The combination of the Stern layer and the diffusive layer is called the electric double layer. The electric double layer is the generally accepted model of the (counter) ion cloud near a charges surface in aqueous solution.

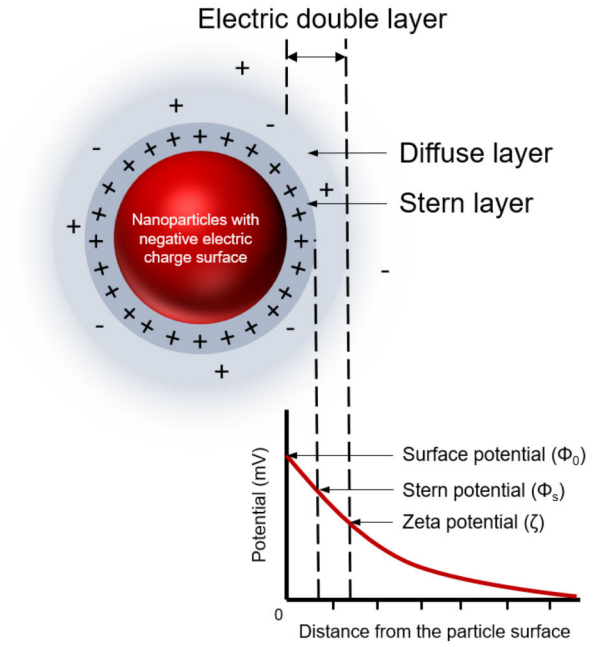

Figure. 2.8 Double electronic layer representation of a gold nanoparticle in solution

The characteristic thickness of the electric double layer is the Debye length. It is reciprocally proportional to the square root of the ionic strength.

$$\lambda_D = \sqrt{\frac{\varepsilon RT}{2F^2 I}} \quad \text{with} \quad I = \frac{1}{2}\sum_i c_i z_i^2 \tag{2.1}$$

$\varepsilon = \varepsilon_0 \varepsilon_r$ is the dielectric permittivity of water, ε_0 is the dielectric permittivity of free space, and ε_r is the relative permittivity or dielectric constant of water (78.3 at ambient temperature). F is Faraday's constant, R is the ideal gas constant. I the ionic strength, z_i is the valence of dissolved ions i, and c_i is the bulk aqueous molar concentration of those ions. In aqueous solutions it is typically on the scale of a few nanometers and the thickness decreases with increasing concentration of electrolyte.[73]

Electrical double layer discussions are now well described and detailed.[74–76] The double layer plays a fundamental role in defining the electrokinetic behaviour of sub-micrometre particles, and also in the colloidal stability.

2.2.2 DLVO model

In solution, interactions between particles can be described theoretically by the Derjaguin–Landau–Verwey–Overbeek model (DLVO).[53, 73, 76–79] This theory is employed to understand the colloidal stability. A plot of potential energy vs interparticle distance is shown in the Figure 2.9 a). It shows that the energy is minimal for zero interparticle distance: thermodynamically, nanoparticles in liquids should be aggregated. This is however prevented from happening by an energy barrier which separates the dispersed and aggregates states of the colloidal solution. Depending on the height of the barrier (compared to thermal energy kT), colloidal dispersions are stable, or aggregate at a certain rate. The barrier depends on the ionic strength (*i.e.* the concentration of added salts, or the salinity) of the solution, see Figure 2.9 c) the diameter of the particles, and the concentration of particles.

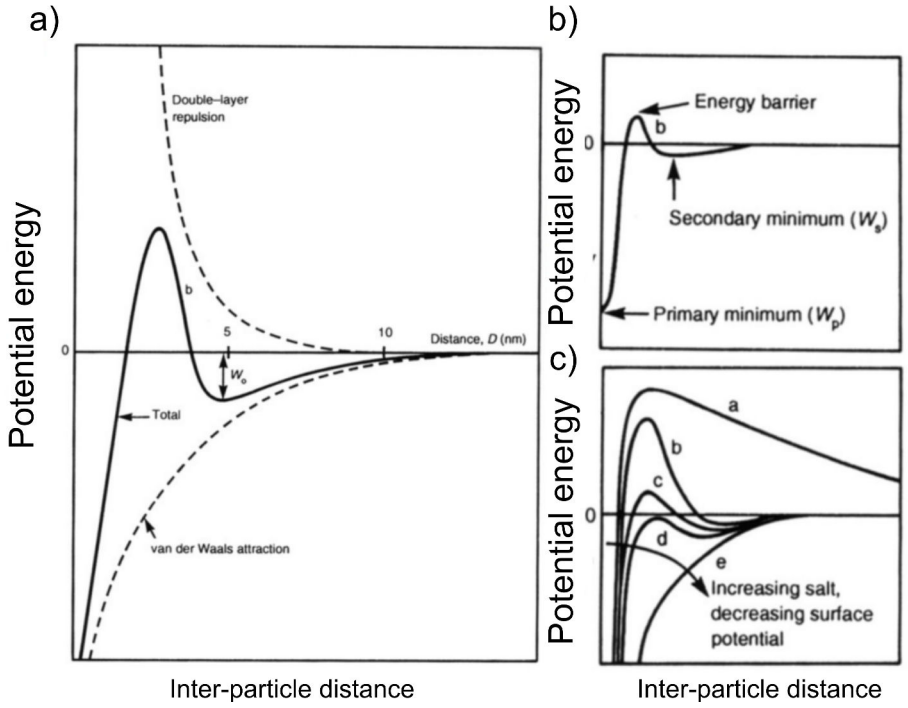

Figure. 2.9 a) Interaction energy of a system composed of two charged particles in water as a function of the distance between both using the DLVO theory. b) Energy minima and energetic barrier. c) Effect of the ionic strength on the potential curves

The chemical composition of the aqueous medium in which particles are suspended is important with respect to the application specifications. In the present thesis, particles are required to be stable in biological mediums and in aqueous solutions. Biological media are characterised by a high ionic strength (salinity) and the presence of a variety of biochemical compounds. To avoid this complexity we choose to work with nanoparticles dispersed in aqueous solutions of controlled salinity, pH and composition. Additionally the surface of the nanoparticles may be coated with different kinds of (bio)functional molecules (bovin serum albumin, streptavidin) for analytical detection schemes.[80]

2.2.3 Brownian motion

Particles suspended in solution are subjected to a random force. These forces are the result of collisions with the molecules composing the liquid, and particles move incessantly as a result of their thermal energy.

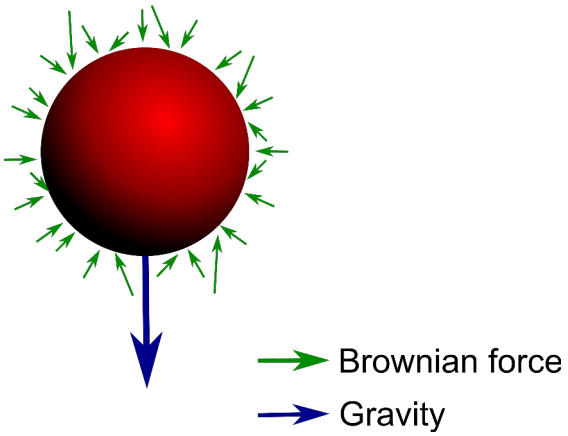

Figure. 2.10 Gravity tends to direct dense particles to the bottom, whereas the random Brownian forces tend to disperse the particles throughout the entire volume

Robert Brown first observed this random motion in 1827, studying the movement of pollen in liquid. Einstein published the theory describing Brownian motion in 1905, giving the distribution in probability of finding a single particle at any point after a

given time. The theory assumes that the impacts of the molecules are statistically independent and extremely frequent, and also that the molecules are much smaller than the particle, allowing the fluid to be treated as a continuous medium. Brownian motion is a stochastic process, *i.e.* the random movement of the particle does not depend on its past. Assuming that the particle starts from a position x_0 at time t = 0 s, and at some time t later it has moved to position x_t. Then, if the displacement of the particle is averaged over a large number of steps, the average displacement is zero, *i.e.* $< x_t - x_0 >= 0$. However, the root mean square of the displacement, Δ, is not. This is

$$\Delta = \left\langle |x_t - x_0|^2 \right\rangle^{\frac{1}{2}} \tag{2.2}$$

Einstein gave the value of Δ as $\sqrt{2Dt}$ per degree of freedom, so that the RMS displacement is $\sqrt{6Dt}$ for movement in three dimensions. Here, D is given the diffusion coefficient for the particle, by:

$$D = \frac{RT}{N_A f} \tag{2.3}$$

R is the universal gas constant, N_A the Avogadro number and f is the friction factor defined for a spherical particle with a radius a as

$$f = 6\pi\eta a \tag{2.4}$$

η is the viscosity of the solution. The viscosity of a fluid is a measure of its resistance to deformation at a given rate. Perrin (1909) carried out a detailed analysis of particle trajectories and confirmed the predictions made by Einstein. Moreover, Perrin used his observations to determine Avogadro's number N_A. (see Figure 2.11)

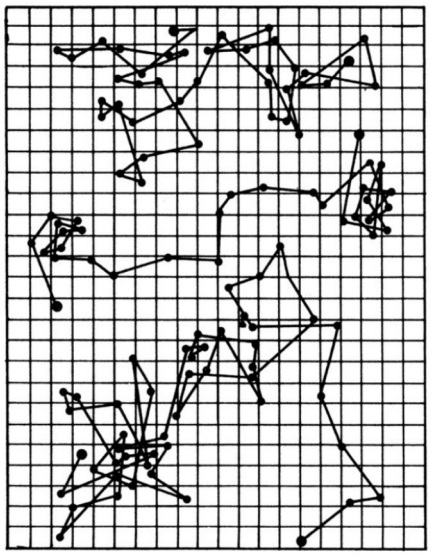

Figure. 2.11 Displacement of three particles: using a camera lucida Perrin marked the successive positions of each particle at regular intervals of time.[81]

2.3 Manipulation of gold particles at microscale

For small particles (smaller than 200 nm), Brownian motion can dominate particle dynamics. The manipulation of sub-micron particles requires a force sufficient to overcome the Brownian motion. Trapping can be realised by two distinctive types of strategies. On one hand, particles can be trapped by applying external perturbations. These have the advantage of being reversible and of being controllable in time. On the other hand, it is possible to capture particles using functionalised or modified surfaces, to which the particles adhere. These methods are generally irreversible. Here, three of the main strategies for exclusively trapping gold nanoparticles were described.

2.3.1 Surface trap

By using a specific coating on the surface,[82] particles can be made to adhere to the surface. The layers deposited have a thickness going from one particle to several particles.

One method for trapping particles at a surface is nanoxerography. Nanoxerography is developed using an AFM tip to inject electric charges into an electret (*e.g.* PMMA). The sample is then submerged into a colloidal suspension. Particles stick to the surface where charges have been printed. This method offers the possibility to trap particles with a very high spatial precision.[9, 83] Another method is layer-by-layer deposition.[84] Methods with multiple steps of layer deposition are used with a coating of the surface with dendrimers.[85]

2.3.2 Optical trap

The optical trap (also named optical tweezers) offers another method to manipulate nanoparticles on the microscale. Optical traps[86] require a high power laser beam focussed by a microscope objective with a high numerical aperture. Optical tweezers typically use infrared lasers with wavelengths significantly longer than the resonance wavelength of gold nanoparticles. Particles are trapped towards the region with the higher electromagnetic field gradient of the focused laser beam. In fact, the high electromagnetic gradient is localised at the centre of the focus. Trapping of gold particles (diameter d $\simeq$ wavelength λ) with diameters of 0.5 - 3 μm was restricted to two-dimensions,[87] because of the high extinction of the particles. Later, three-dimensional (3D) trapping of 36.2 nm gold nanoparticles was first reported by Svoboda and Block.[88, 89] Subsequently, the trapping range of the AuNPs was expanded to span 18 to 254 nm by Hansen and al.[89]

2.3.3 Electric trap

By applying an electric field using microelectrodes, it is also possible to manipulate nanoparticles. Most commonly used electrokinetic phenomena to manipulate gold nanospheres are dielectrophoresis and electrophoresis.

Electrophoresis is often used for the purification of DNA.[90] Also, electrophoresis is used to purify nanoparticle samples,[91] or to determine the global charge at the surface of particles.[92] In particular, in the domain of particles coated with DNA, electrophoresis is very useful to verify the conjugation between particles and DNA.[93]

Dielectrophoretic traps are used to manipulate small amounts of particles. For example, gold nanospheres can be organised as nanowires between two electrodes using dielectrophoresis.[94] Dielectrophoresis will be described in more detail in section 2.4.3.

2.3.4 Advantages and drawbacks

The drawbacks and advantages for the three methods of trapping particle are summarised in Table 2.1.

	Surface Trap	Optical trap	Electric trap
Fast implementation	yes	yes	yes
Trap (reversible/irreversible)	irreversible	reversible	reversible
Force (orientation)	attractive	attractive	attractive or repulsive
Number of particle trapped	high	low	medium
Adaptable to microfluidics	yes	yes	yes
Size area of capture	high (cm^2)	small (0.1 μm^2)	medium (10 μm^2)

Table 2.1 Drawbacks and advantages on key issues of trap techniques.

Now I will focus on trapping using electric fields and more precisely on the dielectrophoretic capture of gold nanoparticles.

2.4 Electrokinetic effects on colloidal dispersions

When an electric field is applied to a colloidal dispersion several electrokinetic effects may appear depending on the frequency and strength of the field.[95, 96] Electrokinetic effects

are divided into forces acting directly on particles (electrophoresis, dielectrophoresis) and into forces which include the motion of the fluid medium (electrohydrodynamics, EHD). EHD takes place easily in confined environments such as a microfluidic channel. The electrohydrodynamic phenomena electro-osmosis and electrothermal effect are detailed in the following section before introducing electrophoresis and dielectrophoresis.[97–100]

2.4.1 Electro-osmosis

Electro-osmosis can be obtained using DC potential (DCEO) or AC potential (ACEO).[17, 101–104] Both DCEO and ACEO are based on the migration of ions within the electric double layer of ions at the interface of an electrolyte and a solid. The layer of charges will migrate under the influence of electric fields tangential to the interface. Because of fluid viscosity, the moving ions carry along their surrounding fluids, leading to overall fluid motion.

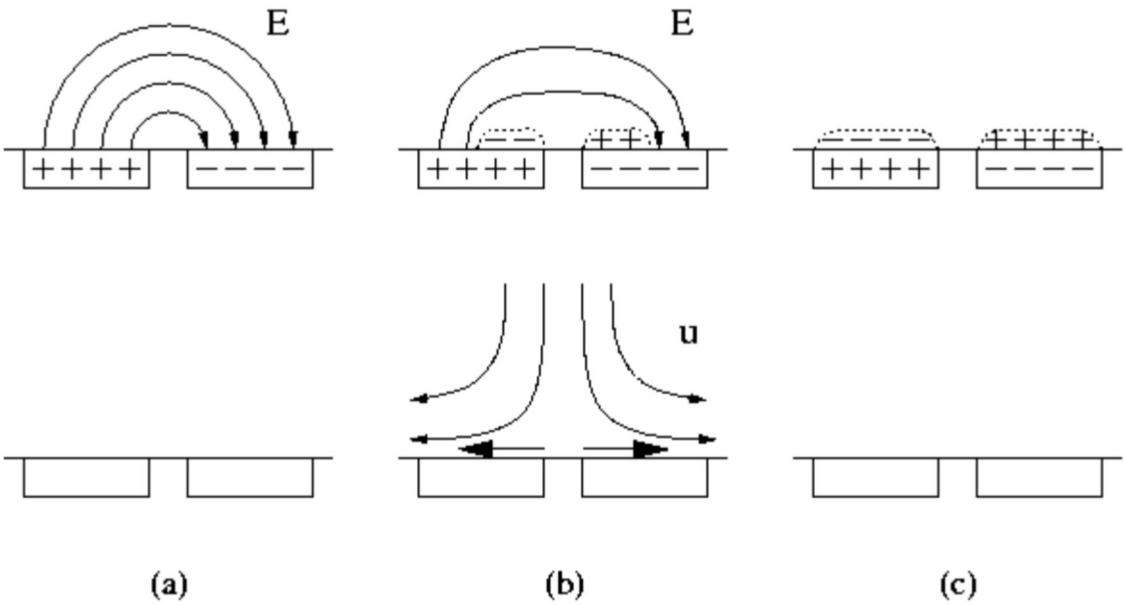

Figure. 2.12 The basic mechanism of AC electro-osmosis: electric field and charge distribution (*top*) corresponding electro-osmotic flow (*bottom*) in response to a suddenly applied voltage across an electrode pair. (a) polarisation of the electrodes giving rise to an electric field. Ions can start moving to this field. (b) Capacitive double-layer charging leads to the motion of ions and can come out of an electro-osmotic flow; the result is EO flow directed away from the electrode gap. (c) After the charging time passes, the electrodes are fully screened, leaving no electric field and thus no flow. An AC voltage can drive a steady time-averaged flow, similar to (b), if its period is comparable to the charging time.

Figure 2.12 shows an AC electro-osmotic (ACEO) flow, directed outward from the interelectrode gap. The flow is independent of the sign of the applied voltage. If the polarity were reversed, then the field and induced charges would both change sign, resulting in the same EO flow. Under AC forcing, the flow becomes strong when the oscillation period is comparable to the charging time. (see Figure 2.12 (b)) ACEO flow decays at higher frequencies, since there is not enough time for charge relaxation. (see Figure 2.12 (a)) It also decays at lower frequencies, since there is enough time to completely screen the bulk electric field. (see Figure 2.12 (c)) The velocity of the fluid is directly proportional to the electric field strength, and the charge density of the surface. The interelectrode gap also has a role on the fluid velocity.[105] At high

frequencies the potential across the double layer and the induced charge are both zero, and again there is no AC electro-osmotic flow.[105]

Globally, at low frequencies (<100 kHz), the dominant fluid flow is AC electro-osmosis. At higher frequencies the magnitude of the AC electro-osmotic flow decreases, and the dominant effect becomes an electro-thermally induced fluid flow (ETE).

2.4.2 Electrothermal effect

ETE refers to fluid motion induced by temperature gradients in the fluid in the presence of AC electric fields. Electrothermal motion (ETE) is created when the electric field acts on gradients in permittivity and conductivity produced by non-uniform heating of the fluid. When an electric field **E** is applied over a fluid with electrical conductivity σ, Joule heating of the fluid takes place. The heating of the sample is described by:

$$\rho C_p \frac{\partial T}{\partial t} = k_m \nabla^2 T + \sigma |\mathbf{E}|^2 \tag{2.5}$$

T is temperature, $|\mathbf{E}|$ is the magnitude of the electric field, k_m and σ are the thermal and electrical conductivities, ρ is the mass density, and C_p is the specific heat (at constant pressure) of the fluid. Motion of the fluid does not substantially affect the distribution of the temperature, implying that the temperature and velocity problems are decoupled. The electric field is also independent of the fluid velocity, so that the electric field can be calculated independently.

For microsystems, convective heat transport is small compared to heat transfer by diffusion.[17, 106] The temperature gradient due to Joule heating leads to a gradient in the permittivity and conductivity. For aqueous solutions, we can estimate the temperature dependence of the permittivity and conductivity.[107–109] The permittivity and conductivity gradients in the applied electric field lead to the time averaged electrostatic body force given by equation 2.6.[98, 110]

$$\mathbf{F}_{ETE} = -\frac{1}{2}\left(\frac{\nabla\sigma_m}{\sigma_m} - \frac{\nabla\varepsilon_m}{\varepsilon_m}\right).\frac{\varepsilon_m|\mathbf{E}|^2}{1+(\omega r)^2} - \frac{1}{4}\nabla\varepsilon_m|\mathbf{E}|^2 \tag{2.6}$$

where σ_m and ε_m are the electrical conductivity and permittivity of the medium. The fluid flow is described by the time-averaged Stokes equation subject to the electrostatic body force.[111] (see equation 2.7)

$$-\nabla P + \nabla\cdot(\mu_m(T)\nabla\mathbf{u}) + \mathbf{F}_{ETE} = 0 \tag{2.7}$$

where μ_m is the dynamic viscosity of the fluid, P the pressure, $\mathbf{u}$ its velocity. In the approximation of small temperature gradients, the changes in fluid properties are also assumed to be small.[112]

ETE is highly dependent on the topology of the electric field. In many cases, with a relative low voltage at high frequency of the applied electric potential, no or undetectable fluid motion is observable, showing the possibility to minimise this effect.[113–115]

An outline of the frequency range in a microfluidic system is represented from calculations with an interelectrode gap of 25 μm and an applied potential of 1 Volt of electric field-induced fluid flow.[105]

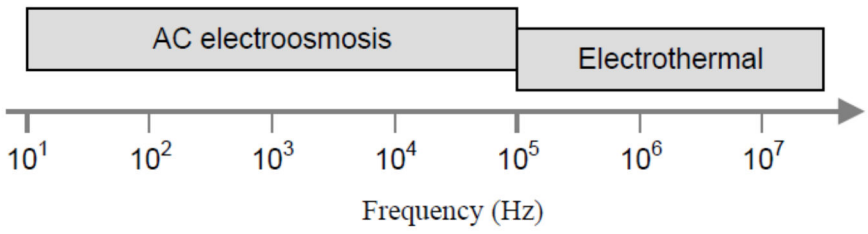

Figure. 2.13 Frequency ranges in which the different types of electric field-induced fluid flow are observed in AC electrokinetic microsystems. The magnitude of the applied potential was 1 Volt and the separation of the two coplanar electrodes was 25 μm. AC electro-osmosis dominates in the lower frequency range (<100 kHz) and electro-thermal fluid flow at higher frequencies.[105]

2.4.3 Dielectrophoresis

As mentioned above, electrophoresis and dielectrophoresis are the main phenomena by which an electric field induces forces directly on nanoparticles in a fluid. Electrophoresis is applicable to particles with a non-zero net charge.

Dielectrophoresis takes place for particles with a zero net charge submitted to a non-uniform electric field. Dielectrophoresis can be induced both by DC and AC electric fields, as long as a non-uniform field is used. Particles submitted to an AC electric field are subjected to a force and move due to the polarisation of the particles' material bulk itself, but also to the polarisation of the electrical double layer. Electric polarisability is the relative tendency of a charge distribution, like the electron cloud of an atom or molecule, to be distorted by an external electric field. When the polarisability of the particle is greater than the surrounding medium, there is more induced charge just inside the particle than outside.[116] This means that there is a difference in the charge density on either side of the particle, which gives rise to an effective or induced dipole across the particle, aligned with the applied field. When the particle is less polarisable than the surroundings, the net dipole points in the opposite direction. The magnitude of the dipole moment depends on the amount of charge moved and the size of the particle.

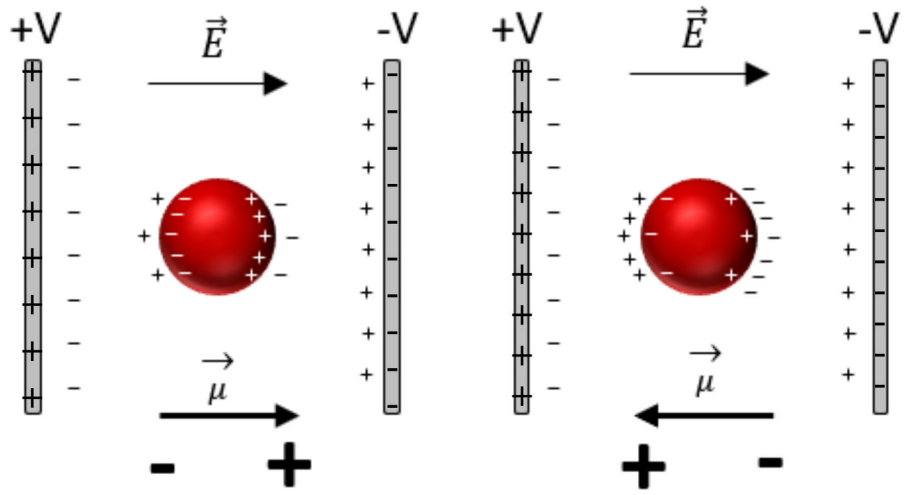

Figure. 2.14 Schematic diagram of how different dielectric particles polarise if they have a higher (*left*) or lower (*right*) polarisability than the suspending fluid medium.

If the polarisability is higher, more charges are produced on the inside of the particle/fluid interface and there is a net dipole across the particle which is parallel to the applied field. If the polarisability is lower, more charges are produced on the outside of the interface and the net dipole points in the opposite direction. The case of a non uniform electric field is studied by calculations done on COMSOL software. (see Figure 2.15)

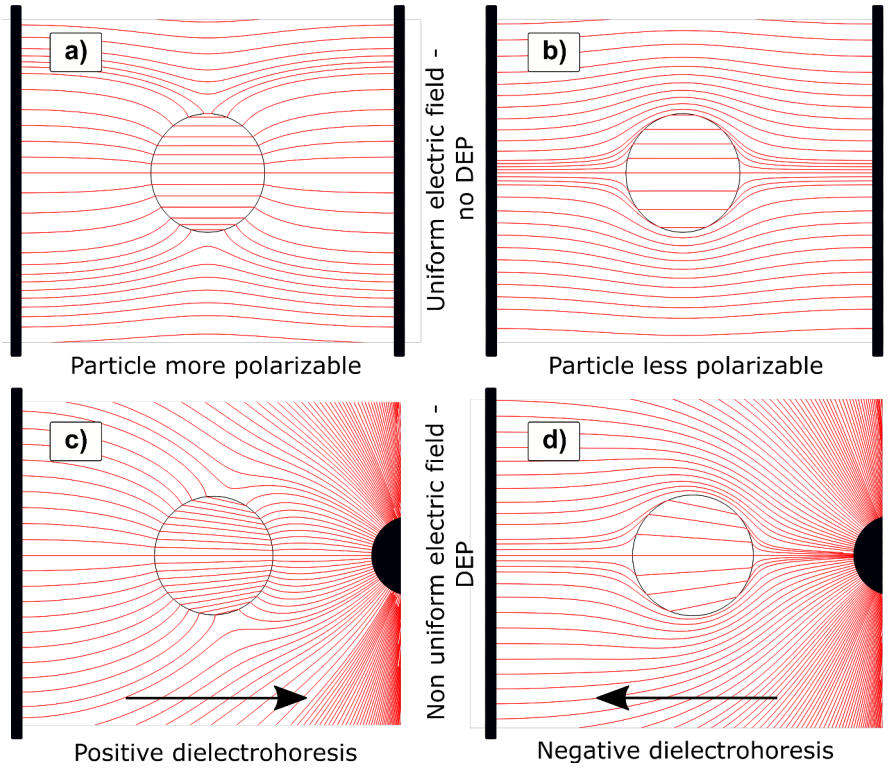

Figure. 2.15 Numerically calculated (COMSOL) electric field lines for four different cases, defined by a particle that is more polarisable (permittivity of the particle, ε_p = 5000 F m^{-1}) or less polarisable (ε_p = 5 F m^{-1}) than the suspending medium (ε_m = 78.5 F m^{-1}), in a uniform or a non-uniform DC electric field (U = 15 V). For the more polarisable particle (a) and (c), the field lines are drawn to the surface of the particle, and the field strength inside the particle is high. For the less polarisable particle (b) and (d), the field lines are bent around the particle and the field strength inside the particle is low. The arrows show the direction of the force and movement in each case.

The time-averaged DEP force experienced by a polarisable particle of arbitrary size, shape and composition in a medium of different polarisability in a divergent AC electric field is well known.[105] A general dielectrophoretic force is given by Equation 5.14.

$$< \mathbf{F}_{DEP} >= \frac{1}{4} V_p \mathrm{Re}\left[\tilde{\alpha}\right] \nabla |\mathbf{E}|^2 \tag{2.8}$$

In this expression, V_p is the volume of the particle, and $\tilde{\alpha}$ is the effective complex polarisability of the particle in the medium, of which the real part translates into the

DEP force when acted upon by the gradient $\nabla|\mathbf{E}|^2$. The effective complex polarisability is frequency dependent.

Calculations have been reported which analyse the predominance of each electrokinetic effect in a system with well-defined and relevant characteristic. (see Figure 2.16).[113]

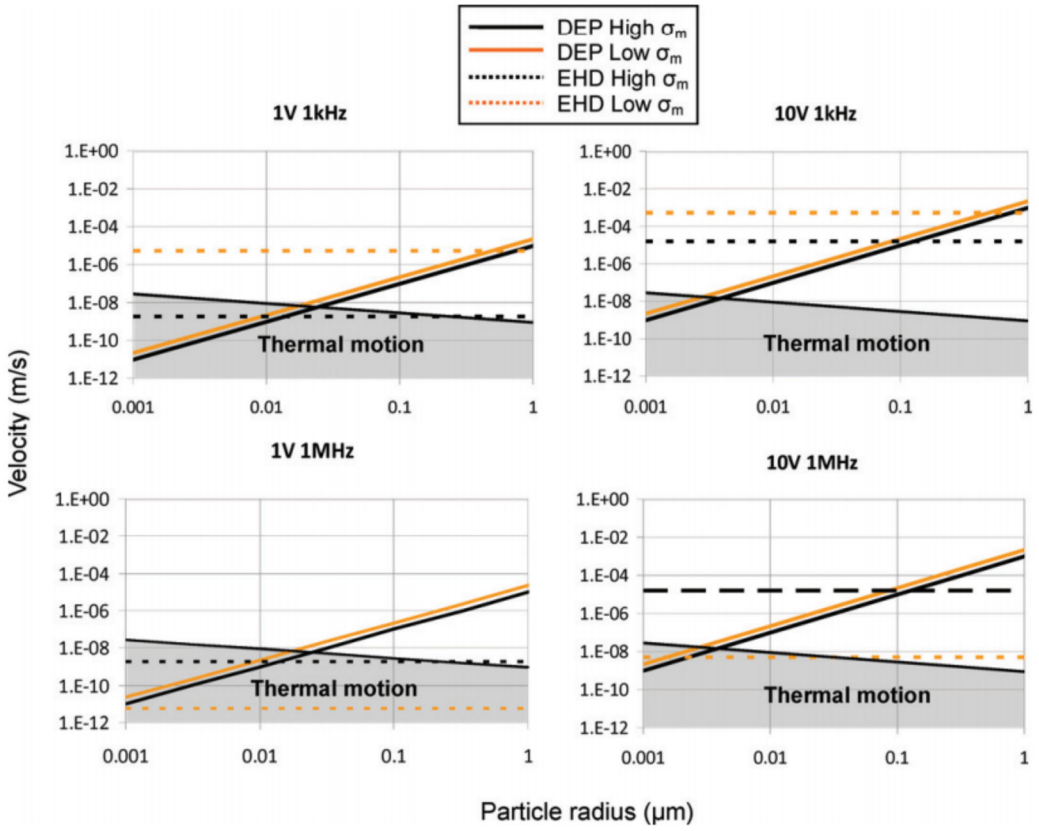

Figure. 2.16 The magnitude of velocity for particles experiencing DEP and drag are shown as a function of particle radius for four frequency and voltage settings (displayed on each graph). The system is defined by Oh.J et al.[114] The force is averaged for all x, 1 mm above the electrode surface. It must be stressed that only general relationships can be determined from such analysis. Velocity caused by DEP was found by equating drag force and DEP force and solving for velocity. The region in grey shows the area where deterministic particle organisation by AC electrokinetics is overcome by thermal motion.

Figure 2.16 shows that at low conductivity (shown in grey), an increase in voltage does not greatly change the point at which DEP force overcomes the EHD force. This is because at this conductivity ACEO is the predominant EHD force and both DEP and ACEO forces have the same relationship with amplitude of the applied signal (proportional to V^2). In fact, the relationship between DEP and ACEO can change slightly since the fluid pattern caused by ACEO is not perfectly constant with voltage. At higher conductivities, however, the balance of forces can change since ETE, which is proportional to V^4, becomes more important to the hydrodynamic force.

2.5 Conclusion

I first described nanoparticles in a broad sense, gradually focussing on gold nanoparticles in aqueous solution, which are the heart of this thesis. The main optical properties of the gold nanoparticles were explained. These results from the plasmon resonance of these particles with an electromagnetic wave. Then, I focussed on the behaviours of gold nanoparticles in liquids and described some of methods which can be used to manipulate nanoparticles in microfluidic systems.

Contactless capture forces as electrokinetics offer the possibility to manipulate very small particles. Micro-fabrication gives access to a very high electric field gradient, adaptable to microfluidic systems. Applying an AC electric field with the right frequency and amplitude as parameters, it is possible to avoid undesirable electrohydrodynamics effects (ACEO and ETE). This gives the possibility to study "pure" dielectrophoresis.

Chapter 3

Formulation and "bulk" spectroscopic characterisation of colloidal dispersions of gold nanoparticles

In this chapter, spectroscopic characterisation of gold nanoparticles in colloidal dispersion will be described. Furthermore, systems in which NPs interact with biological molecules were also characterised. This "macro" study in spectroscopic cuvettes is the prelude to studies of gold nanoparticles in microfluidic systems. Light scattering spectroscopy and fluorescence spectroscopy were used. These two techniques are complementary for the analysis of particles and their interactions in aqueous solution. Light scattering spectroscopy will be mainly used to monitor the stability of particles in solution as a function of the composition of the solvent. But it can also be used to identify the clustering of particles into bigger entities. Fluorescence spectroscopy

was used to analyse the interaction of nanoparticles and biomolecules describing the photoluminescent mechanism between particles and terbium.

First, the choice of the nanoparticles will be explained and the spectroscopic analysis for such particles will be detailed. Then, the interaction between particles and biomolecules will be studied using fluorescence spectroscopy and lanthanide resonance energy transfer.

3.1 Optical properties of gold nanoparticles

The small sizes of metallic gold particles confine the conduction electrons and lead to specific optical properties. The conduction electrons oscillate in response to the electromagnetic wave and at specific frequencies there is a resonance. This results in a peak in the extinction spectrum of the particles which is dependent of the particle environment, size and shape.

3.1.1 Surface plasmon resonance

When the electromagnetic field of the light interacts with metallic NPs, a charge separation occurs and a resonant oscillation of the free metal electrons of the conduction band is observed (see Figure 3.1). This phenomenon is named localised surface plasmon resonance (LSPR) and generates strong extinction of the light due to absorption and scattering light.

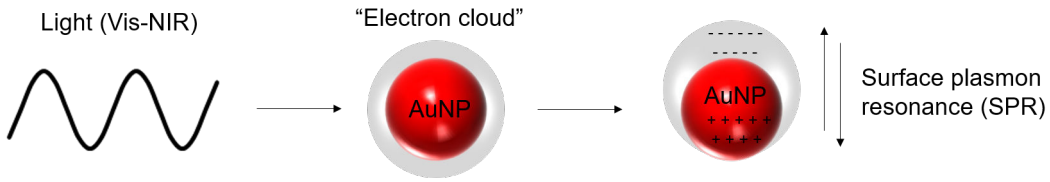

Figure. 3.1 Model of the localised surface plasmon resonance (LSPR) of gold nanoparticles

For particles bigger than 20 nm light scattering becomes a non-negligible contribution to the extinction spectra. (see section 3.2)

3.1.2 Calculation of optical spectra of nanoparticles using theory

In this thesis, Mie theory [117–119] was used to calculate the optical spectra of ideal gold nanospheres in water. This calculation gives access to the quantitative extinction and scattering light spectra of gold nanospheres. This model has some limits: it is representative of spectra for monodisperse colloidal dispersion of perfectly spherical nanoparticles. In contrast, real solutions are polydisperse and particles are not perfectly spherical. By comparing theoretical values from Mie model and experimental spectra, we can have a quick overview of the quality of the colloidal dispersion. The Mie calculations were done using a script implemented in Python (with the Scipy and Numpy libraries).[2]

3.2 Optical spectroscopic methods

Optical spectroscopy is often used to characterise nanoparticles in solution. UV-visible absorbance spectroscopy (here referred to as extinction spectroscopy), dynamic light scattering, Raman spectroscopy and fluorescence correlation spectroscopy are the most commonly used. Additionally, light scattering spectroscopy of metallic nanoparticles permits the analysis of these nanoscale objects with a simple set up. By working at low concentration of particles in solution (where it is often impossible to detect significant signal in extinction spectroscopy), resonant light scattering enables a high sensitivity of detection. Here, a simple analysis method and treatment to study different samples of gold nanoparticles (nanorods and nanocubes) is presented. Employing a

perfect Rayleigh scatterer as a reference (Ludox), the resonant light scattering of gold nanoparticles can be compared quantitatively using the quantum efficiency normalised light scattering (QENLS) of gold particles.[2, 15] In many biological analyse, very small quantities of analytes are used. This method allows the following, in real time the evolution of metallic colloidal solution at low concentration, for many different shapes and sizes of nano-objects.

3.2.1 Extinction spectroscopy

UV-visible extinction spectra were measured using an optical fibre-based system (Ocean Optics) incorporating a USB4000-VIS-NIR CCD spectrometer and a LS-1 tungsten halogen light source (6.5 W, 3100 K). Optical spectroscopy was carried out at ambient temperature on air-equilibrated samples contained in standard 1 cm quartz or plastic (PMMA) fluorescence cuvettes as see in the Figure 3.2.

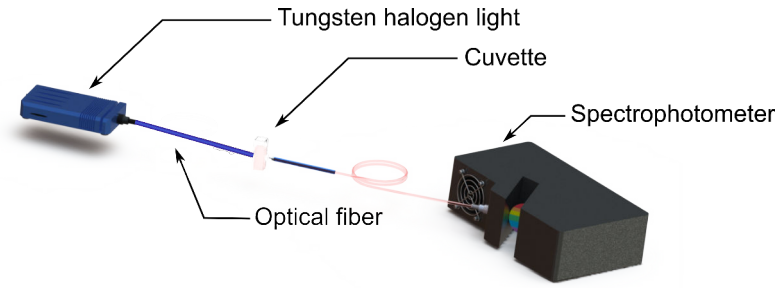

Figure. 3.2 Set-up used to record extinction spectra

Typically, spectra were recorded with an exposure time of 5 ms and averaged over 400 spectra. This corresponds to an equivalent exposure time of 5 ms x 400 spectra = 2 seconds.

At given wavelength, the light extinction by gold nanoparticles is the sum of the light absorbed and the light scattered at this wavelength. The extinction coefficient (M^{-1} cm^{-1}) is related to the total extinction cross-section (in cm^2) of the nanoparticles.

$$\sigma_{ext} = 1000\ ln(10)\ \frac{\varepsilon(\lambda)}{N_A} \tag{3.1}$$

Measurements are done in order to determine the maximum optical density (OD) at the resonance wavelength of the colloidal solution, and directly link this measurement to the concentration of the gold nanoparticles in solution. This can be descried using Beer-Lambert-Bouguer law:

$$OD = \varepsilon_{max}\ l\ c \tag{3.2}$$

Extinction coefficient for gold nanospheres are collected in the table 3.1.

AuNP diameter (nm)	ε_{max} (M^{-1} cm^{-1})
20	9.24E+8
30	3.52E+9
40	9.10E+9
50	1.90E+10
60	3.47E+10
80	8.96E+10
100	1.39E+11
150	2.53E+11

Table 3.1 Maximal extinction coefficient for gold nanospheres as a function of the diameter.

3.2.2 Light scattering spectroscopy

The light scattering spectra consist of the localised surface plasmon resonance of AuNPs, which is sensitive to the environment of the particles. For resonant light scattering (RLS) measurements, the samples were diluted to an optical density below 0.05 and

illuminated with white light (Avantes, Avalight HAL mini). The scattered light was collected at a fixed angle of 90°, and analysed using a CCD spectrograph (Ocean Optics QE65000) (Figure 3.3).[2, 15, 120]

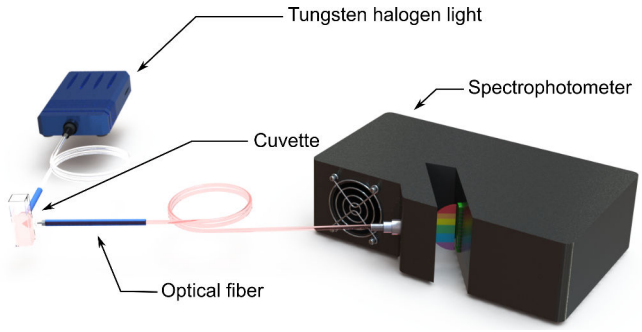

Figure. 3.3 Schematic representation of the resonant light scattering set up using optical fibres to guide. Scattered light is collected at a fix angle (90°) and analysed using a CCD spectrograph

Typically, the acquisition time for RLS spectra is 10 seconds. The CCD array-based spectrometer device allows the acquisition of data at many wavelengths simultaneously. To reduce the acquisition time and follow a faster kinetics reaction, it is possible to use more powerful light sources such as halogen lamps or high-power LEDs.

3.2.3 Scattering reference sample

Raw spectra were first corrected by subtracting the spectrum of the water background. Then a reference spectrum was recorded using a sample of 200× diluted Ludox solution in 50 mM aqueous NaCl as a perfect Rayleigh scatterer.[121]

Three Ludox reference samples were used for each measurement session. The Ludox samples were the supernatant of a Ludox SM30 (Aldrich) suspension centrifuged for 1 h at 9700 x g (9990 RPM), diluted 200 times in 0.05 M NaCl. Before measuring the light scattering, the extinction spectrum was measured and the following equation was fit to the data.

$$OD_{Ludox}(\lambda) = p_0 \ \lambda^{-4} + p_1 \tag{3.3}$$

The baseline value p_1 must be very close to zero. The value p_0 is a measure of the density both optical and chemical of the Ludox dispersion.

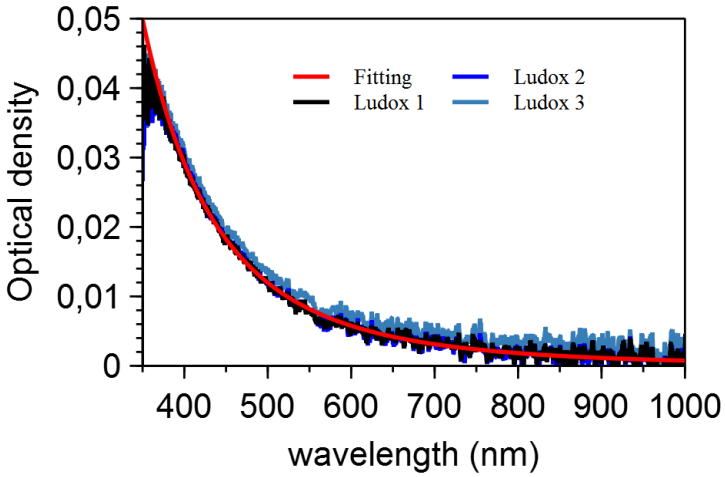

Figure. 3.4 Extinction spectra of Ludox solution, checked with the fitting of $p_0 \ \lambda^{-4}$

The density parameter p_0 is a diagnostic for checking the quality of the ludox sample. Additional study was realised to analyse the stability of the p_0 value during the three years of this thesis.

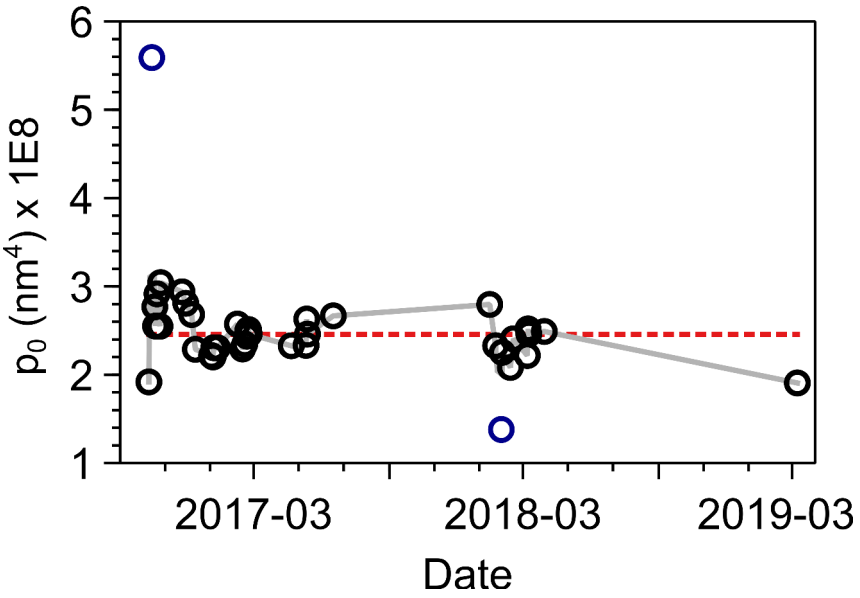

Figure. 3.5 Results of the p_0 value determined as a function of the date during the three years of this thesis. Blue points correspond to Ludox samples not used for measurements of light scattering spectroscopy measurements.

A mean value of the p_0 was determined as 2.41 x 10^8 ± 1.21 x 10^7 nm^4 (95% confidence interval).

Once this p_0 factor was obtained, light scattering spectra of the reference Ludox solutions were recorded. It was verified that all three Ludox samples gave identical raw scattering spectra, and the average of its p_0 was used. Subsequently, the raw light scattering spectra of the nanoparticle solutions were recorded. The corrected light scattering spectra were obtained according to equation 3.4 by calibration of the spectrum against the Ludox reference, taking also into account the coefficient p_0 specific to the experimental set-up.

$$I_{LILS} = p_0 \lambda^{-4} \frac{I_{raw}(\lambda)}{I_{Ludox}(\lambda)} \tag{3.4}$$

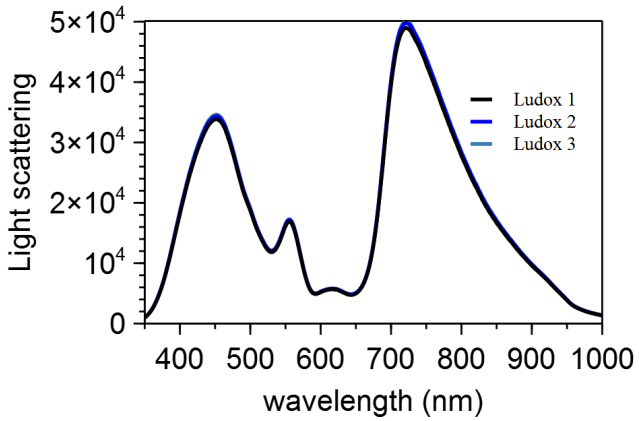

Figure. 3.6 Light scattering spectra of three different samples of Ludox

The subscript 'LILS' signifies 'Ludox-independent light scattering', meaning that the spectrum has been corrected using Ludox and taking into account the density of the Ludox (p_0 parameter).

To compare the light scattering spectra of different samples, normalisation with respect to the concentration (or optical density) of particles is necessary. This was achieved by using the maximum value of the extinction spectrum of the RLS sample. (see Equation 3.5)

$$I_{QENLS} = \frac{I_{LILS}(\lambda)}{OD(\lambda_{max})} \tag{3.5}$$

3.3 Gold nanoparticles

This work uses gold nanoparticles. These particles are stable in aqueous medium, easily characterisable in the UV-Vis range, and can be functionalised with biological molecules.[2, 15, 122–125]

3.3.1 Particles in liquid solutions

Aqueous colloidal dispersions of gold nanospheres were obtained from a commercial source (BBInternational, Cardiff, Wales, UK). They are provided stabilised by the presence of carboxylic acids, mainly citric acid. The size distributions of these particles are well known. However, the unknown composition of the suspension solution represents a drawback. To fix this, the suspension medium was replaced by a home-made solution of well-defined composition. An aqueous solution of 0.2 mM sodium lipoate (NaLA) and 1 mM NaOH was prepared using racemic (±)-α-lipoic acid (LA, Sigma, 0.2 mM) and NaOH (1.2 mM) in pure water. The conductivity of this solution was determined to be 1.8 x 10^{-2} S m^{-1}.

The colloidal gold particles were coated with lipoate by mixing them with the aqueous NaLA-NaOH solution. Samples were centrifuged (Mikro 220R, Hettich) for 30 min with specific rotation speed depending on the particle diameter, as shown in table 3.2.

AuNP diameter (nm)	g (30 minutes)	rpm (Mikro220R)
20	4495	6800
30	3049	5600
40	2259	4820
50	1595	4050
60	1127	3405
80	603	2490
100	389	2000

Table 3.2 Rotation per minute to centrifugate gold nanoparticles in order to keep the stability of the colloidal solution.

The centrifugation concentrated particles as a pellet at the bottom of the Eppendorf tube. Then, the supernatant was removed and replaced (90% of the volume) by the

aqueous NaLA-NaOH solution. This centrifugation-redispersion was repeated three times, and dispersions of lipoate-coated gold nanoparticles were obtained and called Au"XX"-LA ("XX" is the diameter of the particles in nanometer). The nanoparticle samples were stored for 24 hours before characterisation using optical microscopy in order to confirm their integrity. By studying the stability of particles in this solution, over the time of this thesis, it was demonstrated that particles are stable in this solution for over one year.

3.3.2 Gold nanospheres

Stock gold nanoparticle solutions were functionalised with sodium lipoate (as described in section 3.3.1) and then analysed by optical spectroscopy (extinction and light scattering) in order to be characterise check the stability and determine the optical density of all solutions used in this thesis' experiments. (see Figure 3.7)

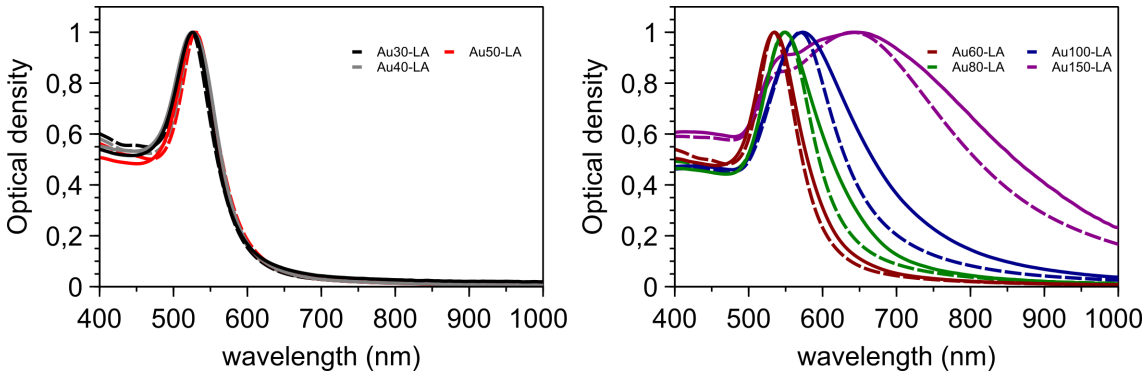

Figure. 3.7 Normalized extinction spectra of gold nanospheres, dotted curves are coming from Mie calculations.

Normalised extinction spectra of AuNPs showed good agreement with the Mie theory. This confirmed the good dispersion of AuNP in solution. It was also further validated by the attendance of a band of extinction and light scattering with defined maximal wavelengths, and width.

Light scattering spectra were plotted to determine the wavelength of maximal scattering by the particles and the stability of particles in diluted solution.

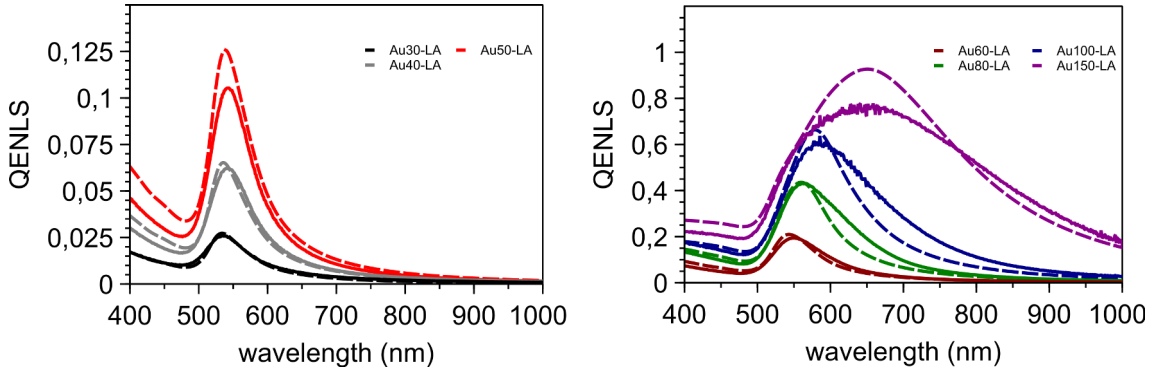

Figure. 3.8 Quantum efficiency normalised light scattering spectra of gold nanospheres. Experimental spectra are solid lines. Theoretical spectra are dotted lines.

QENLS spectra are more sensitive to the dispersion of particles into the aqueous solution. All data (λ_{max}^{ext}, λ_{max}^{sca}, optical density, QENLS) are recorded as references for stock solutions to be in good agreement with future analysis before each experiment.

AuNP diameter (nm)	λ_{max}^{ext}	OD	λ_{max}^{sca}	QENLS$_{max}$
30	525.6	1.17	535.5	0.027
40	525.7	2.27	542.2	0.062
50	528.5	1.90	542.8	0.105
60	534.9	1.95	550.0	0.194
80	549.6	1.19	563.3	0.434
100	573.2	1.03	584.1	0.596
150	646.2	0.61	656.7	0.764

Table 3.3 Optical spectroscopic data for the gold nanoparticle solutions prepared.

3.3.3 Gold nanorods and nanocubes

In this section, spectroscopic analysis was applied to non spherical particles as an illustration of how particle shape effects the optical properties. Extinction and scattering light were recorded for these particles. This study highlights the great potential of non spherical particles for optical detection at longer wavelengths (their resonance peak is red shifted) opening the possibility to characterise particles using specific light sources for the detection of only one type of particles in solution.

Gold nanorods

Gold nanorods (GNRs) were provided by Laurent Guillaume from the PPSM laboratory (Cachan, France).[126] Gold nanorods were synthesized using seeded-growth method.[34, 127, 128] In which two different surfactants are used ensuring a decrease of the GNRs polydispersity and give access to higher aspect ratio. Another method consists to use one-pot radiolytic reduction in CTAB-micellar solutions.[129] From the intrinsic characteristics of their synthesis, GNRs particles are coated with multi layers of CTAB (hexadecyltrimethylammonium bromide).

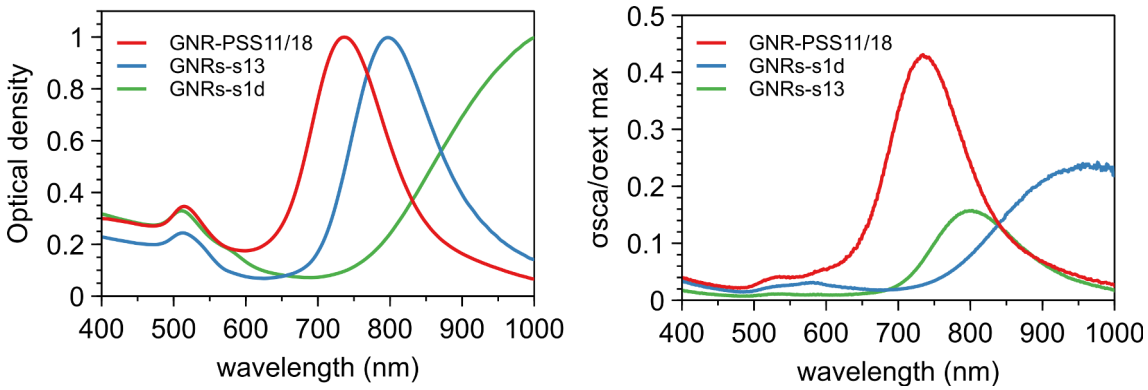

Figure. 3.9 (*left*) Normalised extinction spectra (*right*) Quantum efficiency normalized light scattering spectra of gold nanorods, PSS 01/11/18, GNRs-s13 and GNRs-s1d

Optical responses of gold nanorods particles are specific to their shape. On spectra, the presence of two bands is clearly visible on each (extinction and light scattering).

The distance between bands depends on the size of the rods and more importantly on their aspect ratio (length/width). Light scattering efficiency is more dependent of the aspect ratio rather than the size of the nanorod. Results were compiled in the Table 3.4.

Samples	Length (nm)	Width (nm)	Aspect ratio	$\lambda_{max}(OD_{max})$	QENLS
GNR-PSS11/18	79	25	3.2	743.5	0.431
GNRs-s13	60	15	4	798.5	0.157
GNRs-s1d	97	15	6.5	960	0.239

Table 3.4 Structural and optical spectroscopic data of gold nanorods solutions received

Gold nanocubes

Gold nanocubes were provided by Lisa Stolle from the IPHT (Jena, Germany) in the department of nanobiophotonics. The synthesis method was developed by Matthias Thiele.[130] It uses a microfluidic synthesis which provides advantages in terms of reproducibility. From the sample and spectroscopy characterisation a theoretical calculation was proposed and compared to experimental data.

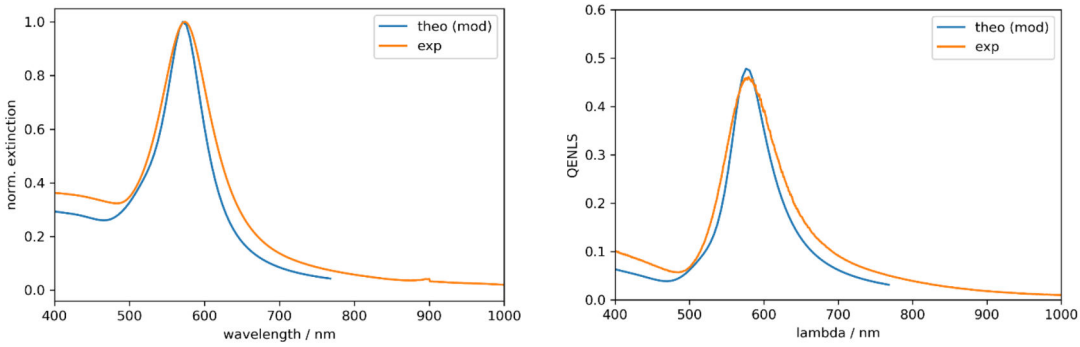

Figure. 3.10 (*left*) Normalised extinction spectrum (*right*) Scattering spectra of AuNC-62 nm, experimental sample in water (with 0.4 mM CTAB), applying factors to the wavelength (0.96) and the intensity (0.94) of the theoretical result.

Cubes spectra show a unique band of extinction and light scattering, to compare with spherical particles with the same typical size (60 nm), the signal is a lightly red shifted. And the quantum efficiency normalised light scattering is higher than spheres. These particles can be interesting for the study of multi-components solutions compared to spheres.

3.4 Interactions between proteins, biomolecules and nanoparticles

The ultimate goal to which this thesis aims to contribute is the development of bioanalytical methods based on the analysis of nanoparticles in microfluidic systems. Some important questions concerning the interaction between biomolecules and nanoparticles are still under deep investigation. One of them is what type of assemblies are obtained when biotin coated particles interact with streptavidin.

The affinity of streptavidin for biotin is the strongest noncovalent biological interaction known, with a dissociation constant ($K_d = 10^{-13}$ M^{-1}) in the femtomolar range.[131, 132] Each streptavidin monomer can bind one biotin molecule, allowing a streptavidin protein to maximally bind four biotins. The biotin-binding pocket is hydrophobic, and there are numerous van der Waals force-mediated contacts and hydrophobic interactions made to the biotin when in the pocket, which is also thought to account for the high affinity. In addition to the strength of the interaction, the binding of streptavidin to biotin provides several further advantages. The bio-interaction is highly specific, rapid on-rate, resistant to changes in temperature or pH (in a reasonable range for biomolecules). Streptavidin also has the capability to be labelled with fluorescent markers which help the detection of the biomolecule.[133, 134]

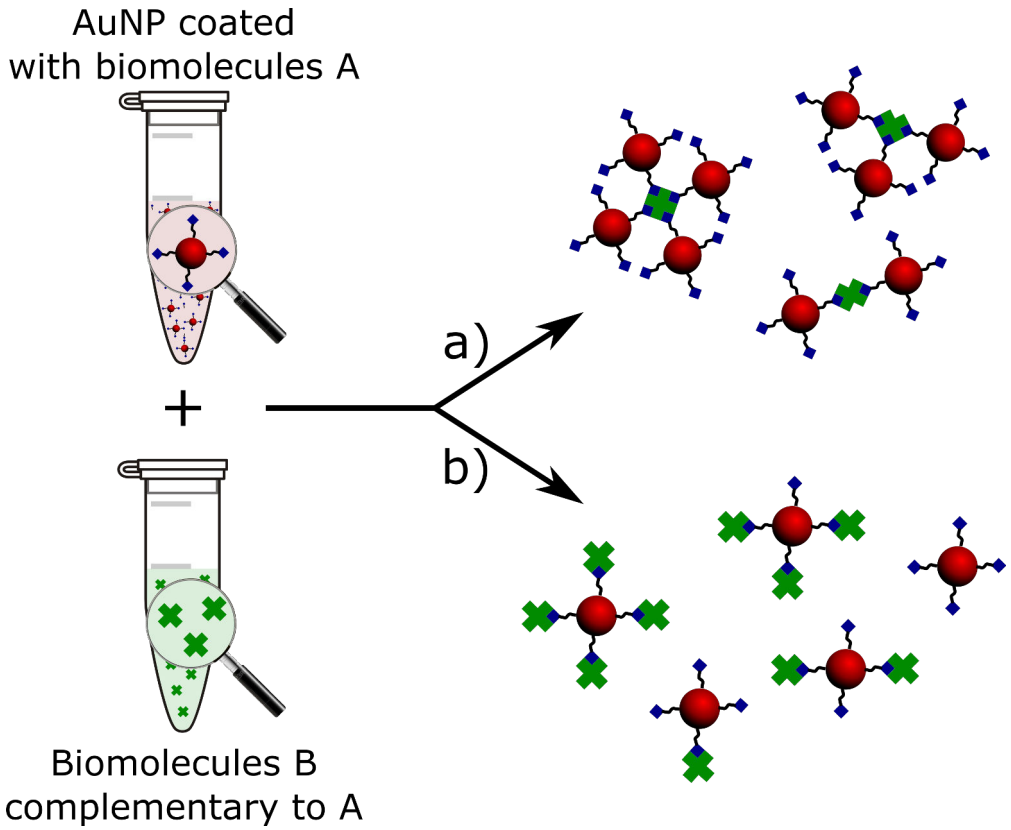

Figure. 3.11 Schematic representation (not to scale) of the assemblies of AuNPs with biomolecules "A" and biomolecules "B" combined to "A" leading to the self-assembly of the nanoparticles. a) Case of self-assembly with particles and biomolecules creating bigger entities in solution. b) Case of assembly between biomolecules A and B but without the creation of bigger (multi-particle) entities.

It is understood that the solutions are stable, *i.e.* the nanoparticles are dispersed as isolated entities, and also the biomolecules are well dissolved. Two cases are possible.

a) Gold nanoparticles are clustered around biomolecules B and form bigger entities in solution. This case is very interesting in the sense that bigger entities show a possible large change in the optical spectroscopic signal. This can help in distinguishing free particles from clusters.

b) The biomolecules bind to the nanoparticle, but no bigger entities are assembled in solution. This result presents an interesting way to detect biomolecules but necessitates more elaborate spectroscopic analysis to confirm interactions.

3.4.1 AuNPs-biotinyled and streptavidin labelled terbium

We chose to analyse the case of bio-nano-assemblies incorporating gold NPs and luminescent lanthanides complexes as an illustration of nano-bio interactions of relevance for biosensing applications. Here, we investigated the interactions between AuNPs functionalised with biotin units at their surface and streptavidin. The streptavidin is luminescently labelled with Tb complexes (Tb-sAv). The biotinylated AuNPs (biot-AuNPs) have diameters of 5, 30, 50, and 80 nm. Interactions in this nano-bio system are schematically represented in the Figure 3.12.

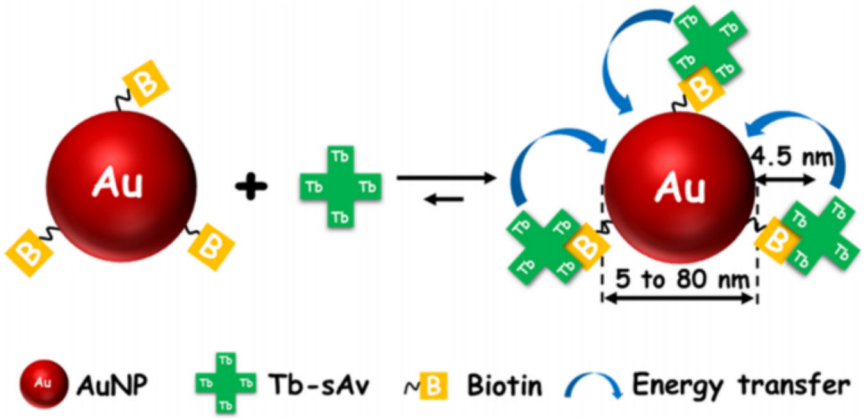

Figure. 3.12 Schematic representation (not to scale) of the assemblies of Tb-labelled sAv (Tb-sAv) and biotinylated AuNPs (biot-AuNPs). For clarity, only 3 biotins are shown. The actual number of biotins attached to the surface of each AuNP was determined to be ca. 25, 900, 2500, and 6400 for the 5, 30, 50, and 80 nm diameter AuNPs, respectively. A distance of 4.5 nm was estimated using a radius of 3 nm for sAv (size of sAv in the solid state: 5.4 nm × 5.8 nm × 4.8 nm in the solid state) plus 1.5 nm for the biotin and linker attached to the AuNP.

In the objective to follow the interaction between streptavidin and biotin the light scattering of the gold nanoparticles was studied. In addition, the terbium labelling offers some distinctive photoluminescence features such as long excited-state lifetimes (in the micro- to millisecond range) and multiple narrow emission bands in the visible region of the spectrum, which can be reliably detected with specific fluorimetric equipment.

The study presented here was carried out in close collaboration with Chi Chen and Niko Hildebrandt, who performed the photoluminescence experiment.

3.4.2 Chemical and physical properties of the biotinylated nanoparticles

The biot-AuNPs were purchased from Sigma-Aldrich (30, 50, and 80 nm diameter, biotin-terminated PEG mol. wt. 5000, dispersion in H_2O). For the measurements of 30 nm and 50 nm Au NPs, 2 mM Tris-HCl (pH 8.5) was used as a solvent, for the measurements of 80 nm Au NPs, pure water was used as a solvent. Black Costar Half Area 96 well microtitration plates were purchased from Corning Inc. (Corning, NY, USA), and Tb complexes (Lumi4-Tb) functionalised to sAv at a ratio of 4 Tb/sAv were provided by Lumiphore Inc. (Berkeley, CA, USA).

The number of binding sites for sAv on each nanoparticle is of the same order of magnitude as the number of biotins per particle. In principle, sAv can bind up to four biotins. The number of biotins per biot-AuNP were given by the supplier as a number density of approximately 0.5 nm^{-2} at the AuNP surface. At the same time, the surface areas were given as 78.5, 2830, 7850, and 20 100 nm^2 for the 5, 30, 50, and 80 nm AuNPs, respectively, which led to 39 biotins per 5 nm AuNP, 1415 biotins per 30 nm AuNP, 3925 biotins per 50 nm AuNP, and 10 050 biotins per 80 nm AuNP. Because no explanation of this estimation was provided, we applied our own estimation based on the number of Au surface atoms, which we calculated to be 500 for 5 nm biot-AuNPs, 18 000 for the 30 nm biot-AuNPs, 50 000 for the 50 nm biot-AuNPs, and 128 000 for the 80 nm biot-AuNPs. Assuming the number of available biotins on the surface to be ca. 5% of the number of Au surface atoms led to 25 biotins per 5 nm biot-AuNP, 900 biotins per 30 nm biot-AuNP, 2500 biotins per 50 nm biot-AuNP, and 6400 biotins per 80 nm biot-AuNP, which were in good agreement with the estimates of the supplier.

Taking into account that four biotins from the biot-AuNP will be able to bind one sAv, and ignoring any steric effects, the number of sAv that can bind to one nanoparticle is anticipated to be 6 for 5 nm biot-AuNPs, 225 for 30 nm biot-AuNPs, 625 for 50 nm, and 1600 for 80 nm biot-AuNPs.

3.4.3 Colloidal stability as a function of the buffer

Optical extinction and light scattering spectra were measured of solutions containing the biot-AuNPs in a selection of aqueous buffers. These spectroscopic measurements enabled determination the long-term stability of biot-AuNPs in these buffers. Colloidal stability is a requirement for reliable results when forming donor-acceptor assemblies. Aggregation of unstable AuNPs would lead to clearly observable changes in the optical spectra. (see Figure 3.13)

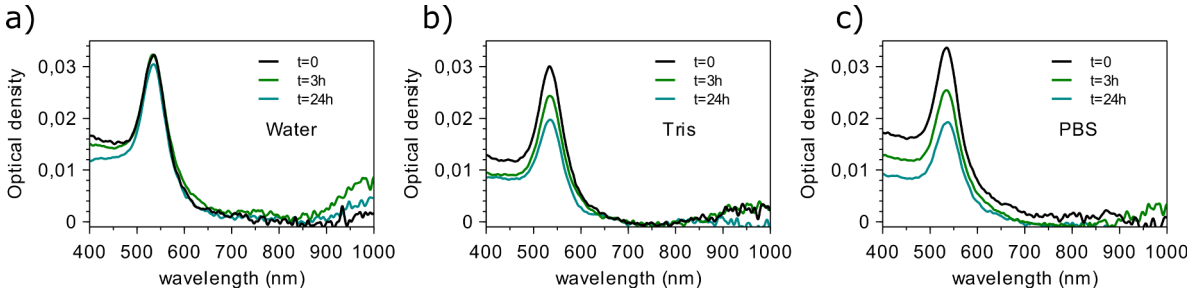

Figure. 3.13 Extinction spectra of 50 nm biot-AuNP at t=0 min, at t=3 hours and t=24 hours in the three different buffers: (a) water, (b) Tris-HCl, (c) PBS

Light scattering spectroscopy is particularly sensitive towards even slight changes in the chemical environment of plasmonic AuNPs.[2, 15] (see Figure 3.14)

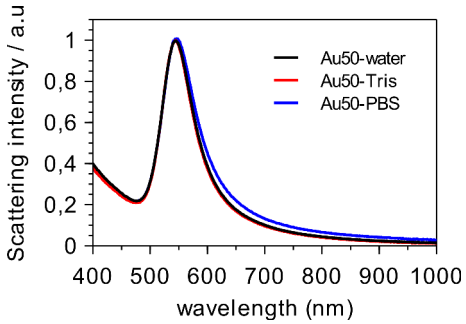

Figure. 3.14 Light scattering spectra of 50nm biot-AuNP after 24 hours in buffers.

From these measurements, it was concluded that 2 to 4 mM Tris-HCl buffer at pH 8.5, and pure water were the most suitable media for the experiments. An alternative buffer, phosphate-buffered saline (10 mM phosphate, pH 7.2, 137 mM NaCl, 2.7 mM KCl) also yielded stable nanoparticle solutions (no shift of the localised surface plasmon resonance maximum) but led to more pronounced “sticking” of the biot-AuNPs to the spectroscopic cell walls.

3.4.4 Resonant light scattering study

To follow the binding of streptavidin to the biotinylate particles the maximum wavelength is analysed by light scattering spectroscopy. The position of the maximum of the resonant light-scattering band λ_{max} in each recorded spectrum was determined by fitting a parabola through the data points in a narrow spectral window ($\Delta\lambda = 10$ nm) around the numerical maximum. The maximum of the parabola obtained from this first fit was then used as the centre point for a second parabolic fit through the measured spectral data points over a narrow window ($\Delta\lambda = 10$ nm), from which a refined determination of the position of the maximum was deduced. This procedure yielded stable and reproducible measurement of the position of the resonant light-scattering maximum λ_{max} RLS and mitigates background noise on the measured spectrum.

The interaction of Tb-sAv with biot-AuNPs was investigated by monitoring the light-scattering spectra of the biot-AuNPs and introducing Tb-sAv into the solution. Immobilisation of biomolecules at the nanoparticle surface leads to small changes (a few nm) in the position of the maximum of these resonance bands. Larger shifts in the plasmon maximum (> 10 nm) are in general the result of clustering of AuNPs into aggregates, which leads to a strong coupling between the localised plasmon resonances of the individual particles. The particular sensitivity of the resonant light-scattering spectrum toward the environment of the AuNPs provides a tool for monitoring the state of the biot-AuNPs when interacting with Tb-sAv.

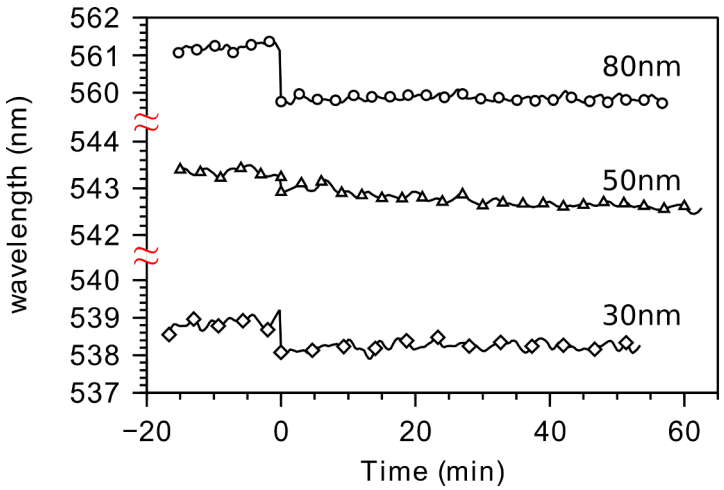

Figure. 3.15 Wavelength evolution of the maximum of the resonant light-scattering band of biot-AuNPs (30, 50, and 80 nm diameter AuNPs) as a function of time. At t = 0, Tb-sAv (25% with respect to biot-AuNP binding sites) was added.

Figure 3.15 shows the evolution of the wavelength of the maximum λ_{max} of the resonant light-scattering spectrum of biot-AuNPs (30, 50, 80 nm diameter) over time, before and after adding Tb-sAv to the solution. The light scattering of 5 nm AuNPs was too weak and not studied. The amount of TbsAv added was 25% of the amount needed to cover all binding. sites on the AuNPs. The position of the maximum did not change over time before adding Tb-sAv, which was in line with the stability of the biot-AuNPs in the buffer. A prompt, small wavelength shift was observed

in the light-scattering resonance of the biot-AuNPs when Tb-sAv was added to the solution. Subsequently, there was virtually no evolution of λ_{max} at longer times after adding Tb-sAv. The observed evolution of λ_{max} is consistent with the binding of Tb-sAv to the biot-AuNPs. The absence of changes in λ_{max} after binding of Tb-sAv to the biot-AuNPs indicates that no significant clustering of Tb-sAv/biot-AuNPs into multi-AuNP aggregates occurred, and that under the experimental conditions, the only biotin-streptavidin assemblies are based on single AuNPs.

This indicates that under the conditions used the nano-bio assembly corresponds to case (b) of Figure 3.11. In order to corroborate this finding, a photoluminescence analysis was done.

3.4.5 Photoluminescence study

Gold nanoparticles are known to be efficient quenchers for luminophores very close to their surface.[24, 135–137] The slowly decaying PL emission from Tb enables a clear distinction of the Tb signal from other, short-lived background fluorescence, while still being subject to electric dipole-dipole energy transfer.[138] This system is a good candidate to be analysed by PL spectroscopy. PL spectroscopy was employed to characterise the different Tb-sAv-biot-AuNP assemblies at various streptavidin/biotin ratios.

PL titration experiments provided further insight in the interaction between Tb-sAv and biot-AuNPs. As the concentration of biot-AuNPs was increased in solutions of constant Tb-sAv concentration, the integrated time-gated Tb PL intensity decreased sharply (Figure 3.16 a), until a certain concentration ratio, after which no further decrease took place. The decrease in overall intensity was accompanied by the appearance of a short PL decay component in the Tb PL decay curves (Figure 3.16 b-d), at

the expense of the long-lived Tb decay from the initial Tb-sAv, which indicates energy transfer from Tb to AuNP

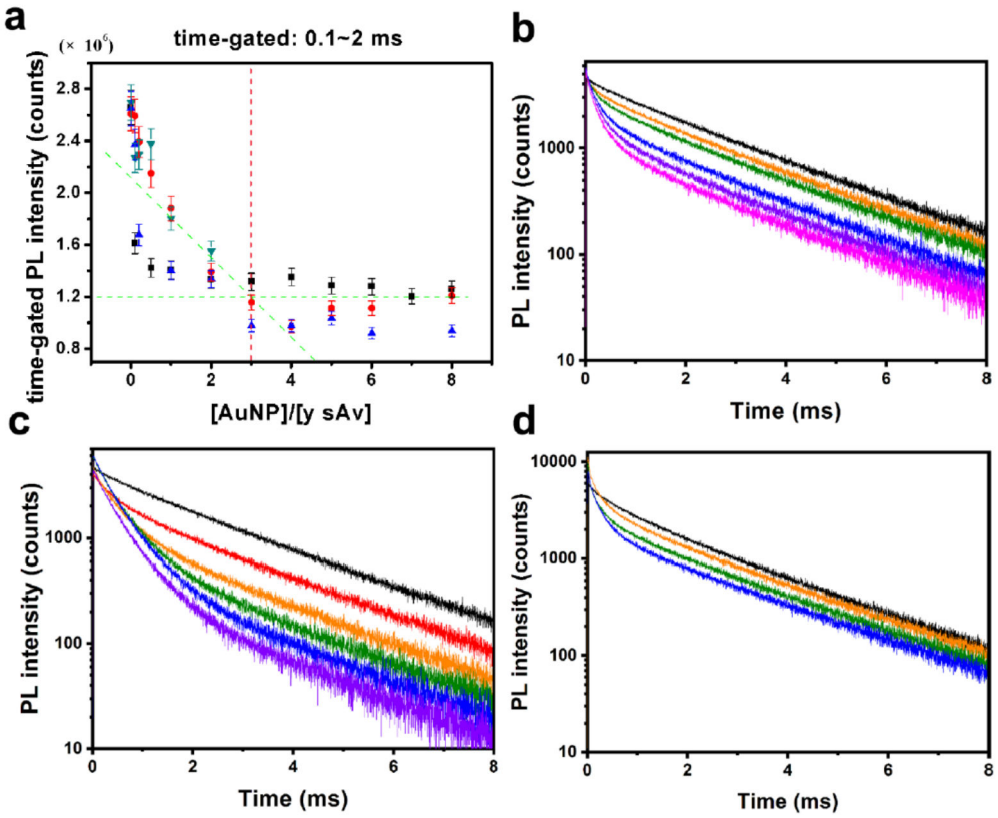

Figure. 3.16 PL titration of Tb-sAv with biot-AuNP (a) Integrated time-gated (0.1 – 2 ms) PL intensities of the PL decay curves (black: 5 nm biot-AuNPs; red: 30 nm biot-AuNPs; blue: 50 nm biot-AuNPs; green: 80 nm biot-AuNPs). Crossing of the green dotted lines (at 3 [biot-AuNP]/ [y Tb-sAv] with y = 6 for 5 nm biot-AuNPs, y = 225 for 30 nm biot-AuNPs, y = 625 for 50 nm biot-AuNPs, and y = 1600 for 80 nm biot-AuNPs) indicates the maximum number of Tb-sAv per biot-AuNP (6/3=2 for 5 nm biot-AuNPs, 225/3 = 75 for 30 nm biot- AuNPs, 625/3 = 208 for 50 nm biot-AuNPs, and 1600/3 = 533 for 80 nm biot-AuNP (b-d): Selected PL decay curves detected within the Tb donor channel for increasing ratios of (x biot-AuNPs) per (y Tb-sAv). (b) 30 nm biot-AuNPs with y = 225 Tb-sAv; (c) 50 nm biot-AuNPs with y = 625 Tb-sAv; (d) 80 nm biot-AuNPs with y = 1600 Tb-sAv. Black: x = 0; red: x = 0.2; orange: x = 0.5; green: x = 1; blue: x = 2; violet: x = 3; pink: x = 4.

The PL titration behaviour can readily be interpreted in terms of the formation of Tb-sAv/biot-AuNP assemblies. Taking into account the results from the resonant light scattering spectroscopy, we can infer that these assemblies exist as isolated biot-AuNPs,

bearing one or more Tb-sAv entities. The concentration ratio [biot-AuNP]/[Tb-sAv] beyond which the PL intensity remains constant, is the concentration ratio at which all (active) Tb-sAv are bound to biot-AuNP. This happened in all cases at approximately 3 times the initially estimated concentration of biot-AuNP necessary to bind all Tb-sAv. This common factor of 3 demonstrates the similarity in binding behaviour of the four diameters of particles, since the initial estimates were based on the same assumptions for each particle diameter. According to the PL titration, the binding capacity was 2, 75, 208, and 533 Tb-sAv per biot-AuNP, for 5 nm, 30 nm, 50 nm, and 80 nm AuNPs, respectively. Using the surface areas of the different AuNPs (vide supra) and the size of sAv in the solid state (5.8 nm x 5.4 nm x 4.9 nm),[139] which would lead to a surface footprint of 24.6 nm^2 (π x 2.9 nm x 2.7 nm), the simple geometrical estimates for coverage of sAv per AuNP are 3 (5 nm AuNPs),115 (30 nm AuNPs), 319 (50 nm AuNPs), and 817 (80 nm AuNPs). When taking into account the curved surface of the AuNPs, the hydration layer of sAv, and possible steric hindrance in sAv binding to biotin in very close proximity, the 35% lower values determined by PL titration are very close to full surface coverage in the simple geometric surface approximation. At [biot-AuNP]/[TbsAv] ratios below the equivalence point, biot-AuNPs carry the maximum number of Tb-sAv. At excess biot-AuNP compared to Tb-sAv, the number of Tb-sAv per biot-AuNP decreases.

3.4.6 Time-resolved PL decay analysis

To investigate the energy transfer mechanism in the Tb-AuNP assemblies, the PL decay curves of solutions containing Tb-sAv and TbsAv/biot-AuNP assemblies was analysed. The PL decay of unbound Tb-sAv in buffer slightly deviates from mono-exponentiality (Figure 4a), which can be attributed to the conjugation of several Tb complexes ($\sim$4) per sAv. The heterogeneity in the local environment experienced by each Tb ion at the

different sAv sites gives rise to a distribution of decay rates. A straightforward approach for analysing the PL decay of such a heterogeneous system is to use a Kohlrausch ('stretched exponential') decay law as it describes the overall relaxation of systems with an underlying distribution of relaxation rates using a minimal number of adjustable parameters.[140–143] The Kohlrausch decay law is given by Equation 3.6.

$$I(t) = A\ exp\left[-(t/\tilde{\tau})^{\beta}\right] \tag{3.6}$$

For $\beta = 1$, a mono-exponential decay is obtained; the underlying distribution is then a Dirac function centred at the decay time constant. For β going from 1 toward 0, the underlying distribution becomes increasingly broad. The average decay time constant for a Kohlrausch decay law is given by Equation 3.7, where Γ is the gamma function.[141]

$$< \tau >= \tilde{\tau}\Gamma\left(1 + \frac{1}{\beta}\right) \tag{3.7}$$

The experimental PL decay of Tb-sAv in buffer is well described (Figure 3.17 a) by the Kohlrausch decay law Equation 3.7, with $\tilde{\tau}_D = 2.07$ ms and $\beta_D = 0.88$, which yields average decay time $< \tau > D = 2.19$ ms.

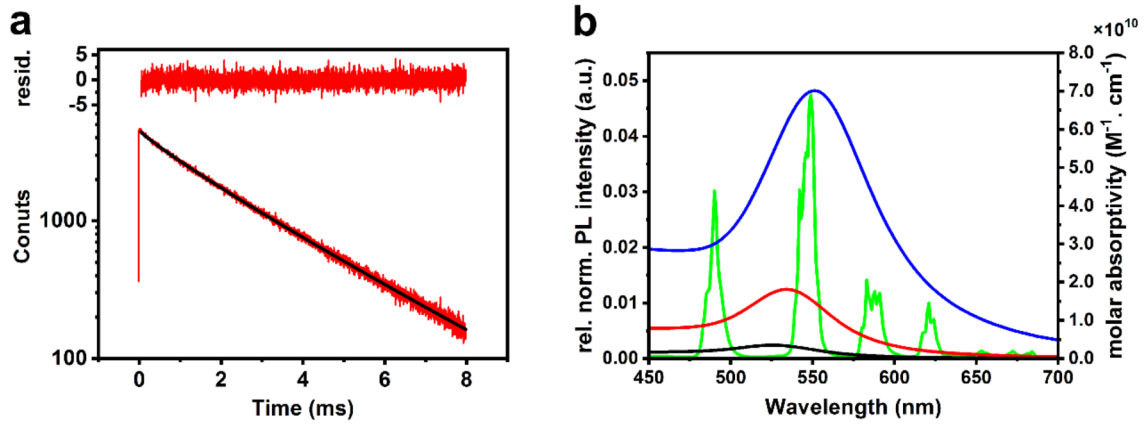

Figure. 3.17 (a) PL decay (λ_{ex} = 337.1 nm; λ_{em} = (490±20) nm) of Tb-sAv in buffer (red) and fit (black) using a single Kohlrausch (stretched exponential) decay law; yielding an average lifetime of $< \tau > = 2.19$ ms. On top: weighted residuals indicating a good fit between model and experimental data, reduced $\chi^2 = 1.26$. (b) Overlap between extinction spectra of 30 nm (black), 50 nm (red), and 80 nm (blue) biot-AuNP acceptors and emission spectrum of the Tb-sAv donor (green).

When biot-AuNPs are added to the solution, Tb-sAv/biot-AuNP donor-acceptor assemblies are formed leading to a mixture of free (excess) Tb-sAv donors and Tb-sAv/biot-AuNP assemblies. The overall PL decay can thus be considered to be the sum of the individual decays of these two species, each described by a Kohlrausch decay, with the subscripts D and DA referring to the free donor and the donor-acceptor assemblies, respectively (Equation 3.8).

$$I(t) = A_D \; exp\left[-(t/\tilde{\tau}_D)^{\beta_D}\right] + A_{DA} \; exp\left[-(t/\tilde{\tau}_{DA})^{\beta_{DA}}\right] \tag{3.8}$$

For the values of $\tilde{\tau}_D$ and β_D we used the values obtained from the measurement of the pure TbsAv donor, and we keep these fixed throughout our analysis, leaving only A_D, A_{DA}, $\tilde{\tau}_{DA}$ and β_{DA} to be determined by curve fitting. This was achieved by fitting the model Equation (3) to the data using the 'lmfit' package [144] in Python, by minimizing the sum-over-squares of the residuals with the Levenberg-Marquardt algorithm. The residual for each time bin was weighted by $1 \propto \sqrt{N_{counts}}$, where N_{counts}

is the number of photons counted in the time bin. Reduced χ^2 values for the fits obtained were in the range of 1.25 to 1.45. The analysis of the PL decay titration of Tb-sAv with biot-Au50-NP are shown in Figure 3.18 . In presence of increasing biot-AuNP concentrations, the PL decay of the Tb-sAv donor is gradually replaced with a shorter PL decay component. This shorter component is attributed to the PL of Tb-sAv attached to the biot-AuNPs.

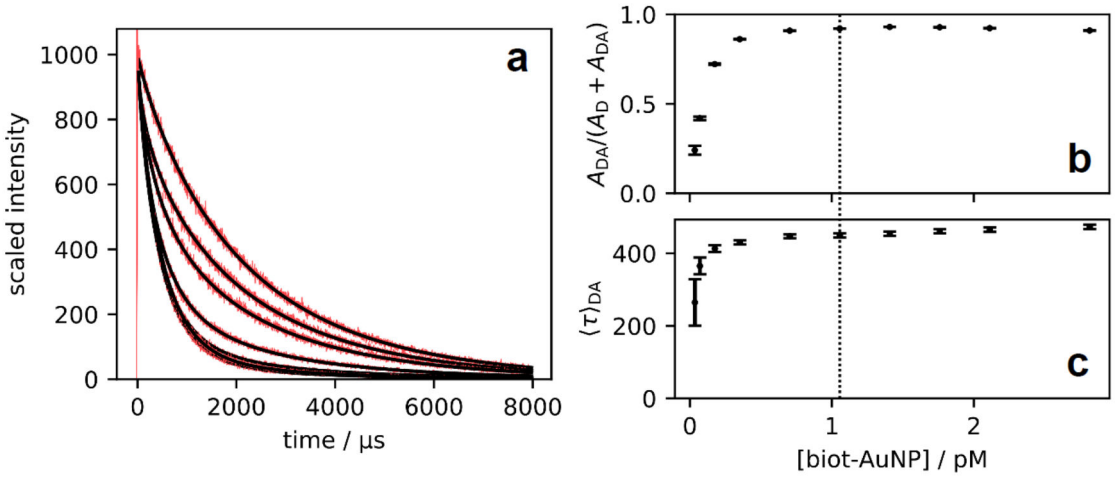

Figure. 3.18 Analysis of PL decays of Tb-sAv (0.22 nM) in the presence of increasing amounts of 50 nm biot-AuNP in buffer. (a) Experimental decay traces (red), with fitted two-component Kohlrausch decay laws (black, Equation 3.8). The traces were scaled to equal initial amplitude for clarity. (b) Amplitude fraction of the Tb-sAv/biot-AuNP donor-acceptor assembly PL decay in the total PL decay as a function of biot-AuNP concentration, obtained from the curve fits. (c) Average PL decay times for the Tb-sAv/AuNP assemblies. The dotted line indicates the minimal biot-AuNP concentration to bind all available Tb-sAv (*i.e.* 208 Tb-sAv per biot-AuNP). The error bars indicate 95% confidence intervals.

From the fits of the model to the data, we obtained the amplitudes of the donor and the donor-acceptor assemblies (A_D resp. A_{DA}), as well as the kinetic parameters for the donor-acceptor assemblies, $\tilde{\tau}_{DA}$ and β_{DA}, as a function of 50 nm biot-AuNPs concentration. From $\tilde{\tau}_{DA}$ and β_{DA}, we obtained the average decay time constant $< \tau >_{DA}$ using Equation 3.7. The donor-acceptor amplitude A_{DA} and average decay

time $< \tau >_{DA}$ are plotted in Figure 3.18 b and c, as a function of biot-AuNPs concentration.

The amplitude fraction of the signal of the Tb-AuNPs donor-acceptor assemblies gradually increased with increasing concentration of biot-AuNPs and reached a plateau near 0.9, indicating a small fraction of Tb-sAv that are inactive in terms of binding to biotin. The luminescence decay due to this non-binding fraction contributes to the signal of the donor-only decay (described by amplitude A_D and lifetime $< \tau >_D$) but does not affect the determination of lifetime $< \tau >_{DA}$ of the donor-acceptor assembly in the curve fits since the model used, effectively separates donor and donor-acceptor contributions.

The average PL decay time of the donor-acceptor assemblies remains constant when excess biot-AuNPs is present, *i.e.* in the cases where only few Tb-sAv are attached to each biot-AuNP. In contrast, the PL decay becomes shorter when the density of Tb-sAv per biot-AuNPs is higher (conditions of excess Tb-sAv). We tentatively ascribe this to energy transfer interactions between Tb-complexes at the surface of the nanoparticles at high Tb-sAv loading levels. Another, less likely, explanation may be that a dense packing of Tb-sAv at the biot-AuNP surface changes the structure of the PEG-biotin ligand shell in such a way as to reduce the average distance between Tb complexes and AuNP surface. In order to avoid contributions of these effects at high loading level, only the measurements at low loading (higher biot-AuNPs concentrations – where $< \tau >_{DA}$ remains constant) are included in energy transfer analysis. In these cases we are approaching the idealised situation where one Tb-complex interacts purely with one AuNP. Similar behaviour was observed with the 5 nm, 30 nm and 80 nm biot-AuNPs. Using the analysis procedure based on the Kohlrausch decay law, we are able to find the average decay times $< \tau >_{DA}$ of Tb(III) luminescence in the donor-acceptor complexes. The results of this Kohlrausch-decay analysis for all AuNP

diameters have been collected into Table 3.5. We consider the average decay time constants for the Tb-sAv/biot-AuNP at low Tb-sAv loading (*i.e.* high biot-AuNPs concentrations) in order to evaluate the energy transfer efficiency from the Tb complex to the gold nanoparticle, using Equation 3.9.

$$\eta = 1 - \frac{< \tau >_{DA}}{< \tau >_{D}} \tag{3.9}$$

	Kohlrausch decay model		
AuNP diam. (nm)	$< \tau >_D$	$< \tau >_{DA}$	η
5	2.17	0.8	0.63
30	2.23	0.19	0.91
50	2.2	0.46	0.79
80	1.66	0.14	0.92

Table 3.5 Tb donor and Tb-sAv/biot-AuNP donor-acceptor decay times obtained from fits of decay models to the experimental Tb(III) luminescence decay.

In all cases, the energy transfer efficiency was larger than 50%, but less than 95%, leaving some Tb(III) luminescence available for detection. In spite of the giant oscillator strengths of the localised plasmon resonance, luminescence quenching is incomplete, and incorporation of photoluminescent entities into assemblies of plasmonic particles for fluorescence tracking and sensing purposes remains feasible.

The energy transfer efficiencies indicate that PL quenching takes place by non-radiative energy transfer, and also that this quenching is incomplete, leaving some emission to be detected. The mechanism for this quenching has been attributed to NSET mechanisms.[145–152] In collaboration with C.Chen. S.Bhuckory and N.Hildebrandt this question was studied in detail. However, this falls outside of the scope of this thesis and only the main conclusion is mentioned here. The energy transfer mechanism is of

the NSET type. The NSET theory enables us to estimate the distance between the streptavidin and the gold NP surface and obtain structural information on assemblies of gold nanoparticles and protein.

3.4.7 NSET mechanism: structural information on protein-nanoparticle interaction

NSET is a nonradiative dipole-dipole energy transfer, the acceptor is a nanometric surface modelled as a collection of many dipoles. In NSET, the efficiency is inversely proportional to the fourth power of the distance between the donor and the acceptor surface of a metallic nanoparticle (NP) (in most cases AuNPs). Research showed that NSET model was in good agreement with the experimental data on small-size AuNPs (below 3 nm) in combination with organic dyes and quantum dots (QDs) as donors. NSET behaviour with energy transfer efficiencies independent of the NP size or number of donors was also demonstrated for larger-size AuNPs. For NSET analysis, the R_0 is calculated by Equation 3.10.[145, 146]

$$R_0^{NSET} = \left[0.225 \frac{\Phi_D}{\omega_D} \frac{1}{\omega_F \kappa_F} c^3\right]^{1/4} \tag{3.10}$$

where ω_D is the angular frequency resonant with the donor electronic transition, ω_f and $\kappa_{\bar{f}}$ are the angular frequency and the Fermi vector for bulk gold, respectively, and c is the speed of light. The calculated R_0^{NSET} was 7.2 nm for all three different sizes of AuNPs (Table 3.6). In NSET, R_0 is independent of nanoparticle diameter, since the energy transfer is assumed to be to a flat surface, which is a good approximation for a small emitting dipole in proximity to the surface of a much larger sphere.

c (m s^{-1})	3.00E+08
ϕ_D	0.64
ω_D (s^{-1})	3.80E+15
ω_F (s^{-1})	8.40E+15
k_F (m^{-1})	1.20E+10
R_0 (nm)	7.20E+00

Table 3.6 Parameters used in the NSET model evaluation of resonance energy transfer from Tb to AuNPs

The Tb-AuNP distance (r) was subsequently calculated using Equation 3.11.[153]

$$r = R_0^{NSET} \left(\frac{\tau_{DA}}{\tau_D - \tau_{DA}} \right)^{1/4} \tag{3.11}$$

With the PL decay times for the donor and the donor-acceptor assemblies as determined above, and the R_0 determined using NSET theory, Tb-AuNP distances r were obtained that are collected in Table 3.7. All distances found are in the 4.0 to 6.4 nm range, and do not show a strong dependence on the acceptor AuNP diameter. Moreover, these distances are well in line with the estimated average distance of the Tb complexes conjugated randomly to the sAv binding via biotin to the surface of the AuNP (see Figure 3.12).

	Kohlrausch decay model	
AuNP diam. (nm)	r/R_o	r (nm)
5	0.87	6.3
30	0.55	4.0
50	0.72	5.2
80	0.55	4.0

Table 3.7 Tb-AuNP surface distances r calculated from the experimental luminescence decay times and the NSET theory. Distance were calculated from both the Kohlrausch PL decay analysis and the multiexponential decay results.

When considering the overall uncertainty on the donor-acceptor distances r derived from the experimental luminescence decay measurements, we distinguish two main sources of uncertainty, the first being the experimental error on the experimental decay times, the second the uncertainty on the value on R_0^{NSET}. In order to separate these two contributions to the overall uncertainty, we have included the ratio r/R_0 in Table 3.5. This ratio thus depends solely on the uncertainty of the experimental measurements, which is relatively small. The uncertainty on R_0^{NSET} was estimated to be 10% and represents a systematic uncertainty. The NSET model afforded a set of donor-acceptor distances that are similar for the various AuNP diameters studied and consistent with the expected structure of Tb-sAv/biot-AuNP assemblies. Thus, we show here that it is possible to functionalise gold nanoparticles with biotins that bind streptavidin, without clustering into larger entities.

3.5 Conclusion

In this chapter we explained and illustrated the formulation and spectroscopic characterisation of gold nanoparticles in solution. Light extinction and light scattering

spectroscopies give access to information on the quality and stability of gold nanoparticle dispersion. Light scattering provides enough sensitivity to work at very high dilution.

With this spectroscopic background, we studied the interaction between biotin and streptavidin using gold nanoparticles. Light scattering measurements gave access to information on the assembly of biotinylated particles with streptavidin. It was shown that particles functionalised with biotins bind streptavidin, but did not assemble in bigger entities.

The photoluminescence analysis showed complementary information. It was demonstrated that biotins on the surface of particles interact with streptavidins, leading to the binding of sAv to the NPs.

By these two complementary spectroscopic analyse of particle interactions with biomolecules, we conclude that the assembly flows case b) in the Figure 3.11.

In brief, we have been able to formulate and characterise dispersion of gold nanoparticles of different composition. These formulations were used in the experiments described in the following chapters.

Chapter 4

Design and development of the electromicrofluidic device and the microfluidic workstation.

In this chapter, the microfluidic device used for the analysis of nano-objects undergo dielectrophoresis forces in microfluidic channels will be described starting from its design, manufacturing and characterisation to its operating instructions. The system is composed of several parts, each one requiring specific attention and skills from different fields: electronics, microfabrication, optics, chemistry. First, each of these parts will be addressed in this chapter. Then, the characteristics of the full device and surrounding test equipment will be presented. Image and video analysis methods will be described from video-microscopic observations of dielectrophoresis to the underlying physical chemistry of these observations.

4.1 Overview of the complete system

The electromicrofluidic system was designed to be easily built and versatile. The overall system is composed of subsystems parts. One subsystem takes care of the control and synchronisation of all parts of the electromicrofluidic system. The second subsystem is designed to contain and manipulate the samples' solution. The third is constituted of the signal detection and the following of the physical phenomena.

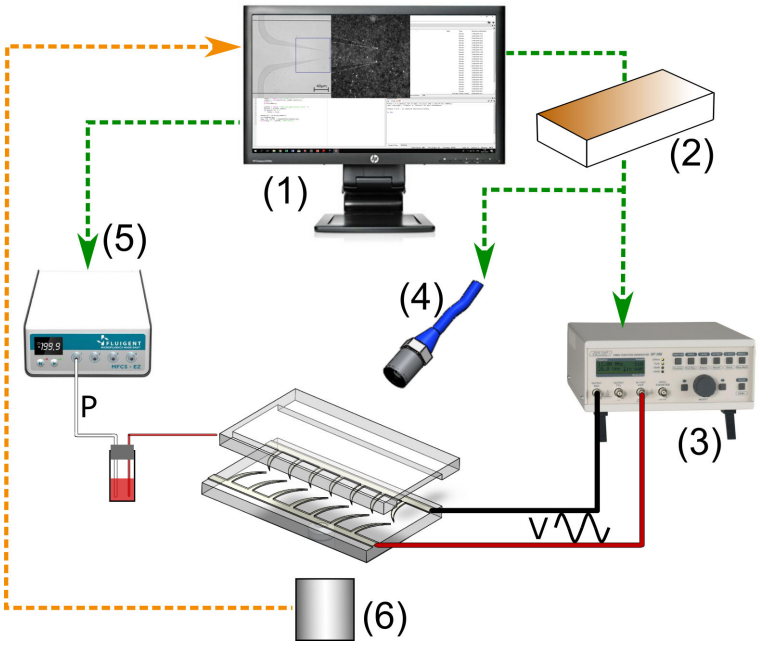

Figure. 4.1 Experimental set-up for dielectrophoresis measurements in microfluidic systems. (1) PC workstation for global control of experiment and recording of video-microscopy. (2) Arduino single board controller. (3) Electronic function generator used to polarise electrodes. (4) High-power LED coupled into fibre and focused inside the microchannel. (5) Fluigent pressure controller. (6) Optical microscope with attached camera and spectrometer.

Using a Fluigent pressure controller, nanoparticles solution is injected into the microfluidic channel in which micro-electrodes array was positioned at the centre of the channel. Particles are individually observed by microscopy and followed by imaging with a camera. The light source of the system is dependent on the detection method. For dark field images, high power white LED was chosen and light was injected by the

side of the microfluidic system (dark field videomicroscopy). For bright field images, the microscope light source was used and illuminates the microfluidic channel by the top (bright field videomicroscopy and extinction spectroscopy). Light illumination was synchronised with the function generator using an Arduino single board controller.

4.2 The electromicrofluidic device

4.2.1 Fabrication of thin-film ITO micro-electrodes

A single design pattern was used for the thin-film microelectrode. (see Figure 4.2) This choice was made with the aim to always have the same topology of electric field.

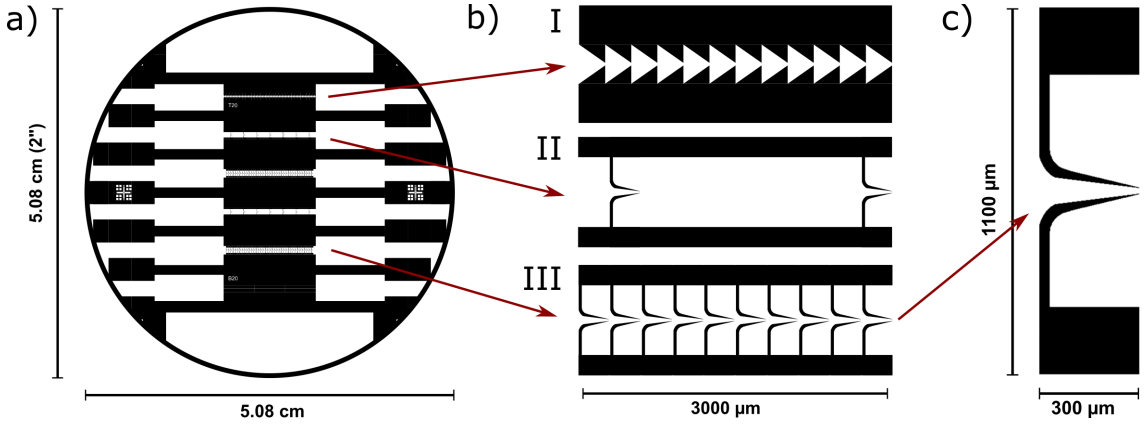

Figure. 4.2 a) Architecture (and lithography mask) of the hook electrodes chosen for the electromicrofluidic device. b) I- Christmas tree row of electrodes. II- Hook row of electrodes spaced by 1400 μm between each pair. III- Hook row of electrodes without spacing between each pair. c) Building brick of the micro puce

The electrodes' design is composed of four linear arrays of pairs of hook shaped electrodes. Two arrays have 1400 μm spacing between electrode pairs and two arrays have 300 μm spacing between electrode pair.

These electrode architectures were chosen for the capability to exhibit a high electric field gradient localised in a very small area near the top of their tips. The gap between both to electrode tips gradually diminishes to reach 20 μm at the top. By having a

linear array of electrodes pairs there is the possibility of using microfluidic flow along the electrodes.

The full mask also contains triangular "Christmas tree" electrodes, but these were not exploited. "Christmas tree" electrodes were not used in this thesis but some exploratory experiments observations were done. First, it is important to note that during microfabrication "Christmas tree" electrodes are most robust to wet etching, compared to the hook electrodes: this is an advantage. Nevertheless, the gaps between electrodes are larger (30 μm), and limit the gradient of the electric field. To be able to use them as an efficient alternative these type of electrodes should be redesigned.

The electrodes were patterned on indium tin oxide (ITO) thin film. Two types of glass slides were used. First, soda-lime glass slides of 1.1 mm thick (Solems, S.A., Palaiseau, France) covered with an ITO layer, approximately 80 nm thick. The other type of glass slides were 170 µm thick fused silica slide (ACM, Viliers St Frédéric, France) and had a 100 nm thick layer of ITO. ACM glass slides are superior optically which is beneficial for our optical microscopy application, but they are also more fragile.

The electrodes microfabrication procedure consists of five steps (see Figure 4.3).

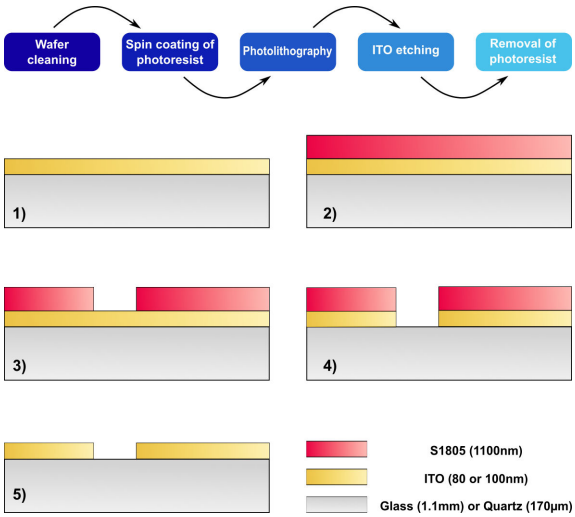

Figure. 4.3 Steps of the ITO electrodes microfabrication. (1) original state, (2) resin photosensible deposited on, (3) non-exposed resin light removed, (4) etching of ITO, (5) electrodes ready for use

First, (1) the wafer was cleaned by rinsing subsequently with acetone, isopropanol and Milli-Q water, and further dried.

(2) Positive photoresist "S1805" (Rohm and Haas, USA) was deposited onto the substrate by spin coating for 30 s at 1000 rpm with 100 rpm s^{-1} acceleration. The resist layer was subsequently dried on a hot plate at 115 °C for 60 s. The thickness of photoresist obtained was near to 1100 nm. (see section 4.2.2)

(3) The photoresist was exposed to UV (i-line-365 nm; 180 mJ cm^{-2} dose) on an MJB4 (Süss MicroTec, Germany) mask aligner using a chrome quartz mask (JD Photo-data, UK) containing the electrode design. The exposed resin was removed from the ITO substrate (70 s, in pure developer "MF319" Rohm and Haas).

(4) Wet etching of the ITO layer was achieved using concentrated hydrogen chloride (HCl)(aq) (25%, Sigma-Aldrich) for 110 to 115 s at 40 °C for 80 nm thick of ITO (etching rate 0.71 nm s^{-1}). To verify the success of this step, the conductivity at the surface was measured to ensure that no short-circuit was detected where the ITO needed to be removed. Etching was furthermore characterised using profilometry (see

section 4.2.2), the results obtained were 1080 nm of S1805 resin and 80 nm of ITO, for a total height 1160 nm.

(5) The last step consisted of removing the unexposed resist from the ITO substrate with an acetone cleaning step. After this, the thickness of the ITO layer was determined using profilometry: the expected 80 nm was confirmed (see section 4.2.2). A final cleaning by a series of solvents (acetone, isopropanol, water, drying with air jet) was done in order to obtain a clean substrate with ITO electrodes.

Before assembling the complete microfluidic system, ITO electrode substrates were cleaned from any organic molecules using a low-pressure air plasma for 5 minutes (Harrick Plasma Cleaner, Sterilizer PDC-002, USA). Additionally for previously used electrode substrates any deposited gold nanoparticles from prior experiments were removed by treatment with diluted gold etch solution (151 mM potassium iodide, 25 mM I_2 in water) during 4 min at clean-room temperature (19 °C). Finally, they were thoroughly rinsed with deionized water and dried under a filtered air compressed stream.

4.2.2 Characterisation of thin-film ITO micro-electrodes

To analyse the different steps of microfabrication the Alpha-Step IQ (KLA-Tencor) profilometer was used. This technique was used to precisely determine the thickness of each of the layers. The surface was scanned with a diamond tip on a determined length l, following the x axis. The coordinates (x, z) were recorded. Typical measurements were recorded for 1 to 180 μm with a speed of 5 μm s^{-1} and a frequency of 50 Hz, in duplicates.

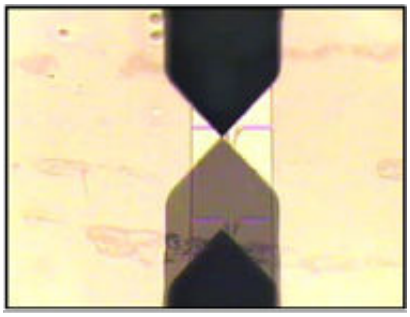

Figure. 4.4 Micrograph of the diamond tips of the profilometer analysing hook electrodes

Profilometric analysis was done at each microfabrication steps in the ITO electrode fabrication process using previous method. The results were resumed in the Figure 4.5. First, the thickness of the deposited resist S1805 was checked on several wafers to determine precisely, the deposited thickness (red curve) as a function of the spin coating speed. The error on the thickness of the layer was determined to be lower than 1%. Then after etching of the ITO, the thickness of the ITO removed is checked looking at the height difference with the previous step (green curve). Last, the layer on the quartz was checked after all fabrication steps and must correspond to the height of the ITO deposited previously by the industrial supplier (blue curve).

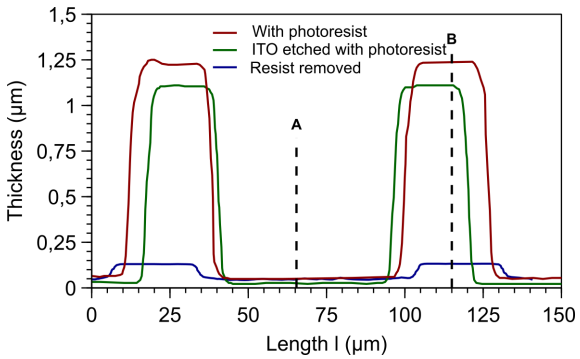

Figure. 4.5 Profilometry of the electrode substrate at different stages of microfabrication

As expected, the profile of each measurement is very flat with steps edges indicating the absence of side effects of the wet etching. This validates the durations of etching for ITO and verifies the absence of etching under the resist. (see Table 4.1)

Layers	Height (B-A) (nm)
ITO	80
Resin	1083
Resin-ITO	1163

Table 4.1 Resume of the layer deposited on the quartz substrate

In addition to profilometry, optical microscopy (transmitted light, bright field) was used to identify microfabrication problems issues. The use of a digital camera and digital contrast enhancement is an easy and very helpful way to observe the ITO electrodes. (see Figure 4.6)

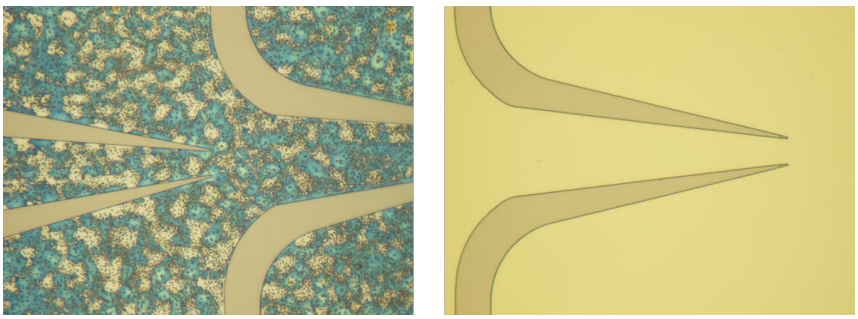

Figure. 4.6 Microscope pictures (50X) of ITO electrodes. (*left*) Insufficient developed substrate (resist incompletely removed). (*right*) Properly developed sample (no resist remaining)

The resin shows a colourful thin layer on the ITO when an insufficient time of development was applied.

4.2.3 Fabrication of microfluidic channels

Microfluidic circuits were made using soft lithography.[154, 155] They were molded into an optically transparent silicone elastomer (PDMS Sylgard 184 - Dow Corning). For fabrication of the mold, an SU-8 layer (Microchem SU-8 3025) was spin-coated on top of a 2" silicon wafer (10 s at 500 rpm with 100 rpm s^{-1} acceleration followed by 30 s at 2000 rpm with 300 rpm s^{-1} acceleration for a 20 μm thick layer). The wafer was then slowly baked for 10 minutes at 95 °C. A Süss-MicroTec MJB4 mask aligner was used for the photolithography step, using our design masks, drawn with the software CleWin (4.3.7.0; WieWeb software) and printed by JD Photo-data,UK. The photoresist was exposed to UV-light (365 nm) during 10 s using a photo mask aligner from suss microtech. A post-exposure bake was done at 65 °C for 1 min followed by 3 min at 95 °C. Then the resist was developed in a specific developer, made for SU-8 resins, with a time dependent on the thickness of the resist layer (typically 3 min for 20 μm). After the rinsing and the drying of the mold a hard bake (cure) was realized at 150 °C.

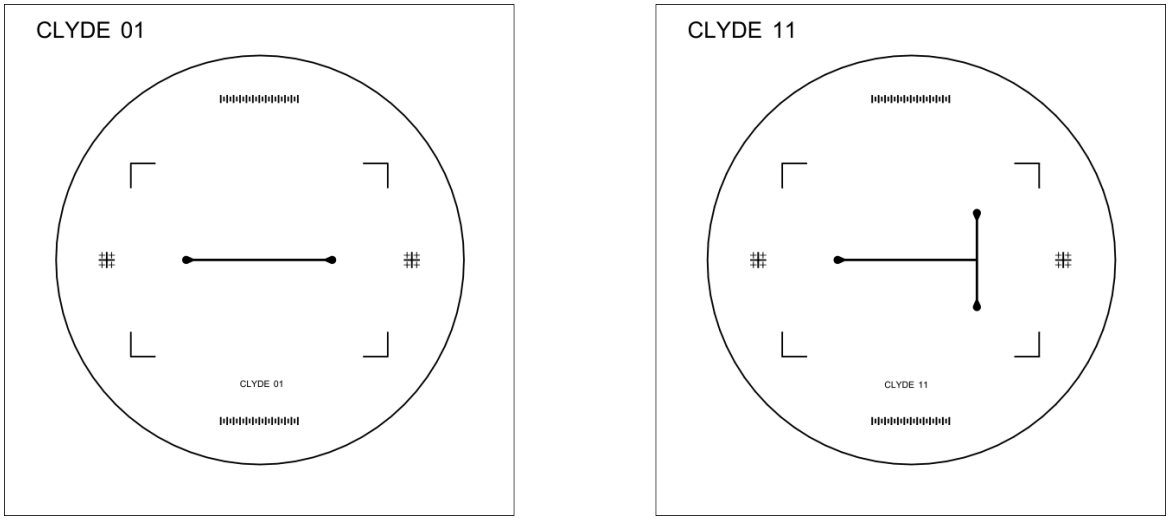

Figure. 4.7 Design masks 1 and 11 drawn using CleWin software and used to create SU-8 molds

4.2.4 Characterisation of SU-8 molds using profilometry

Each SU-8 mold was analysed using the profilometer in order to check the microchannel height. (see Figure 4.8)

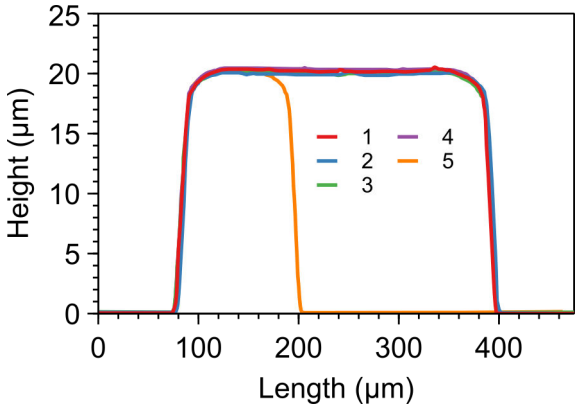

Figure. 4.8 Thickness of SU-8 deposited by spin coating on silicium wafers. 1 to 4: Profilometric scans of four different molds with a 300 μm width channel. 5: microchannel of 100 μm of width.

As shown in the graph, all SU-8 molds characterised had the desired height of 20 μm. The error in thickness of microfabrication was found to be $\pm 1\%$ for more than fifteen molds manufactured. The reproducibility of the SU-8 resin deposit method and molds fabrication for PDMS microchannel was very good.

4.2.5 Pouring of PDMS and electro-microfluidic assembly

A 10:1 mix of PDMS and curing agent was prepared and carefully degassed under reduced pressure (1 hour, 0.1 bar). The mix was then carefully poured on top of the SU-8 mold in a plexiglass holder. (see Figure 4.9) The plexiglass holder, with the PDMS was placed at 70 °C for one hour for the PDMS to cure. Microfluidic chips were obtained, by peeling off the PDMS from the mold. Finally, inlet/outlet holes were punched into the PDMS.

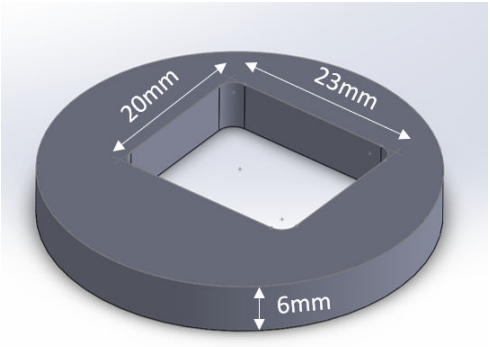

Figure. 4.9 Plexiglass holder produced using laser cutting to embrace the ideal size of the PDMS slab. It provides PDMS systems with smooth edges that allow for clean injection of the light from the side of the slab

The microsctructured PDMS slab, were placed on the electrodes surface and aligned to the selected array of electrodes. For assembling the electromicrofluidic device, the bottom of the PDMS slab was wetted with a small quantity of ethanol (3 drops) which enables slab to slide over the substrate. Positioning was then achieved manually in the clean room, monitoring alignment of the microfluidic channel and the electrode structure using an optical microscope. Once aligned, the device was left to dry, and microfluidic tubing was connected. The PDMS were not stuck to the substrate with plasma binding but simply laid out over substrate. The adhesion was strong enough to sustain low microfluidic flow, and weak enough to be reversible.

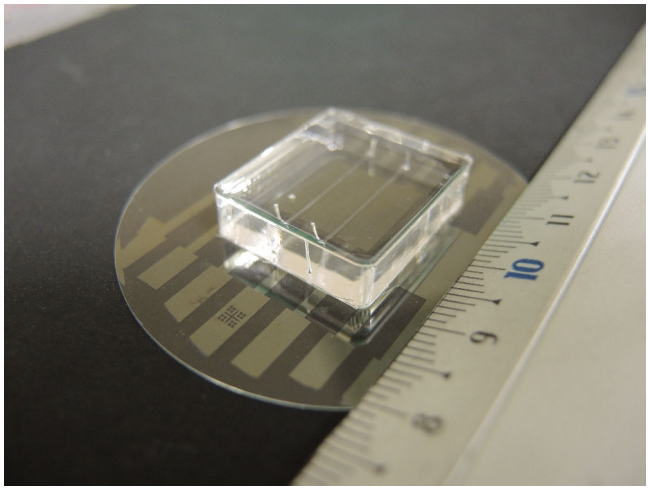

Figure. 4.10 Pictures of a PDMS double channels stucks on the quartz wafer and aligned to the ITO electrodes ranges

4.3 Installation of the electro-microfluidic device on the optical microscope

4.3.1 Mechanical support

The microfluidic videomicroscopy and spectroscopy workstation was built around and inverted optical microscope (Olympus IX-71). The microscope was equipped with a motorised stage (Märzhäuser Wetzlar, Germany) that positions the sample in the x and y direction ($i.e$ in the microscope object plan). The electromicrofluidic device was mounted onto this motorised stage using a custom designed sample holder.

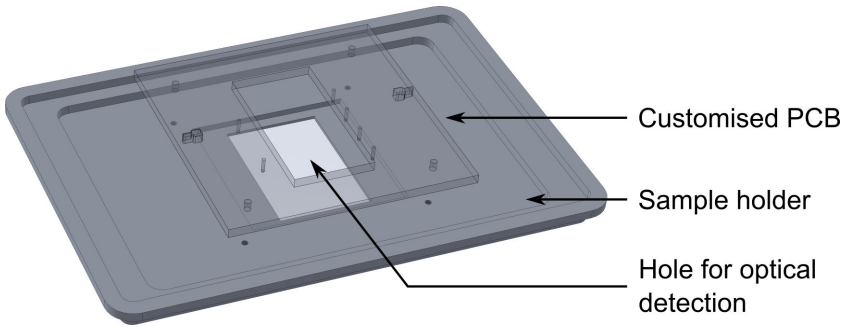

Figure. 4.11 Sample holder for mounting the electromicrofluidic device on the microscope, including the placement for electrical and optical system

This custom sample holder was designed using Solidworks software.

4.3.2 Electrical and mechanical assembly

The ITO electrodes of the devices were connected using a specific printed circuit board assembly containing spring loaded electric contacts. Jumpers are integrated onto the printed circuit board (PCB) to select to which electrode pairs the potential was applied. Connection to the function generator was ensured by an SMA connector.

PCB allowed the use of two inches wafers (square or round) carrying our electrode design. A hole was made in the centre to allow observation of the system with the optical microscope.

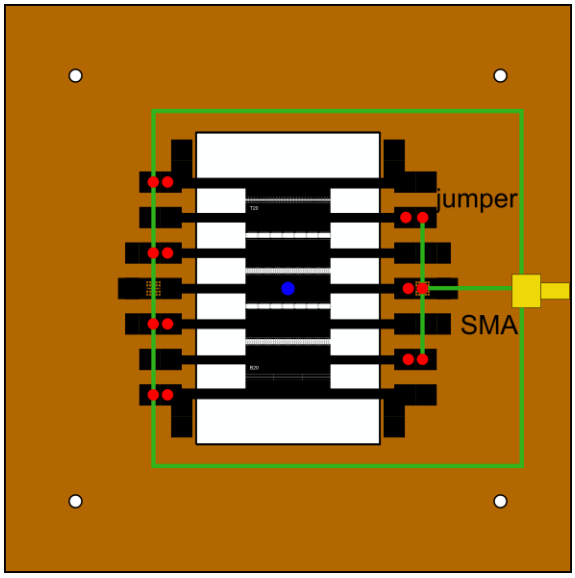

Figure. 4.12 PCB created for the electromicrofluidic devices. Jumpers are used to select the specific electrode pairs to be connected.

To summarise the microfluidic device used for the dielectrophoresis consisted of one electrodes chip, a PDMS microchannel and a mechanical support adaptable on an inverted optical microscope. (see Figure 4.13)

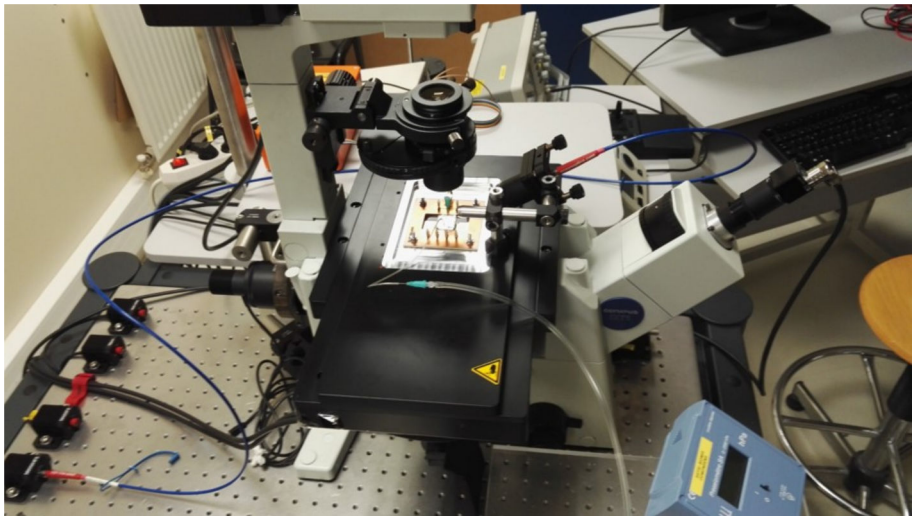

Figure. 4.13 Photo of the dielectrophoretic system mounted on the microscope system coupled to the image detection

4.3.3 Dark field configuration

The IX-71 inverted microscope used was easy to modify and adapt. After several iterations the final configuration for dark-field video microscopy was described in Figure 4.14.

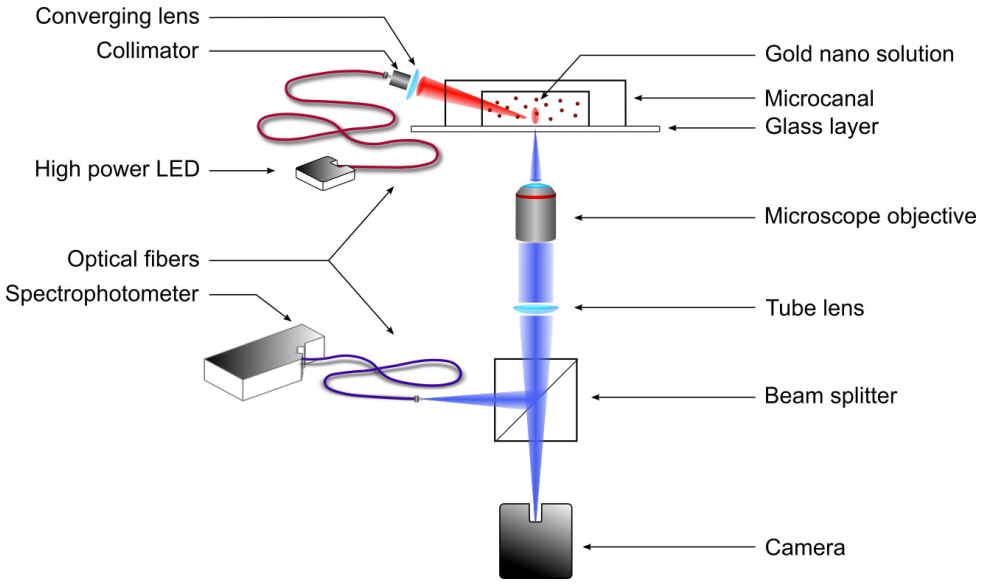

Figure. 4.14 Scheme of the microscope optical path of the high power LED light source of the colloidal solution samples, and the light emitted by the samples to both detectors, the spectrophotometer and the camera. This setting recorded dark field video-microscopy or scattered light emitted.

Figure 4.14 showed how the illumination and the detection chain was built around the inverted microscope. Both parts were perfectly fitted to use with the microscope optical configuration. The high power LED can be changed easily and can be commercially bought. In the thesis only a white LED was used, but a green LED (in resonance with the LSPR of gold nanoparticles) could also be used. The compromise was to choose between the maximal power and the wavelengths emitted. The detection exit was already included on the microscope, only a fibre entry was placed and the camera was positioned on the binocular port.

4.3.4 Fluorescence configuration

To test our microfluidic system experiments were done using fluorescent latex spheres. For the observation of these particles, standard wide-field fluorescence microscopy was used. Aqueous colloidal suspensions of fluorescent latex spheres of 200 nm (yellow-green fluorescence), 500 nm ("polychromatic red" fluorescence) diameter were obtained from a commercial source (Polysciences). Rhodamine-dyed latex particles of 810 nm were a gift from R. Antoine (ILM Lyon). The latex particles are referred to as PS200, PS500 and PS810, respectively. The concentration of latex spheres in the stock solution was 5.68 x 10^{12} particles mL^{-1} for PS200 and 3.64 x 10^{11} particles mL^{-1} for PS500. In the DEP experiments, latex spheres were diluted in order to have concentration of particles similar to Au100-LA. The dilution was achieved, using 0.2 mM lipoate in 1 mM NaOH in pure water to work with the same physico-chemical environment as the gold nanoparticles. The optical path of the microscopic observation is depicted in Figure 4.15.

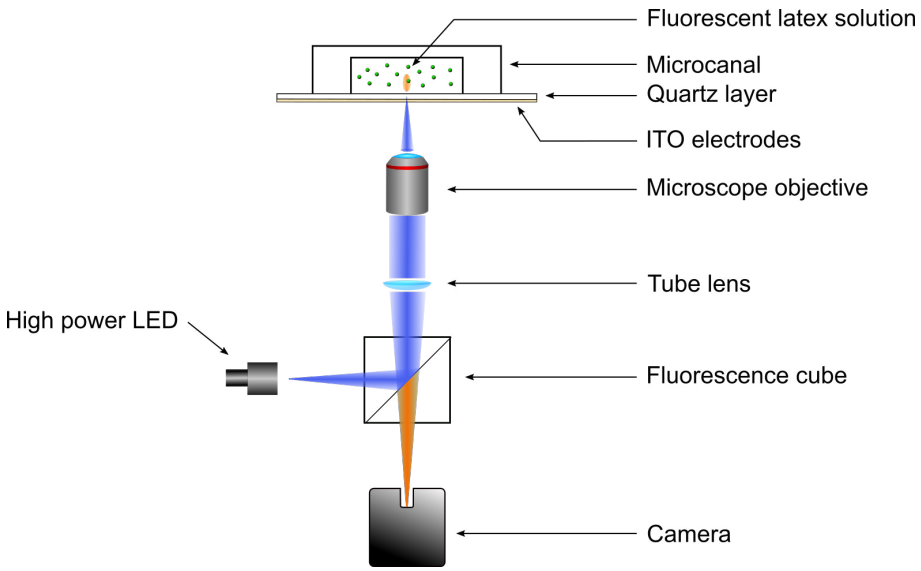

Figure. 4.15 Schematic of the fluorescence microscope that was used to observe fluorescent latex spheres inside the electro-microfluidic system.

The choice of the high power LED M470-L from Thorlabs (λ= 470 nm) as the excitation source was done in agreement with the optical properties of the latex fluorophores (YG: Yellow-Green, PCR: PolyChromatic Red). The choice of fluorescence filter cube (U-MSWB2, Olympus) is important to maximise the intensity of the signal. The cube consists of one excitation filter (BP420-480), one emission filter (BA520IF) and one dichromatic mirror (DM500). Figure 4.16 collects the transmission and reflection spectra of the fluorescence cubes of the microscopes, together with the fluorescence emission spectra of the latex spheres.

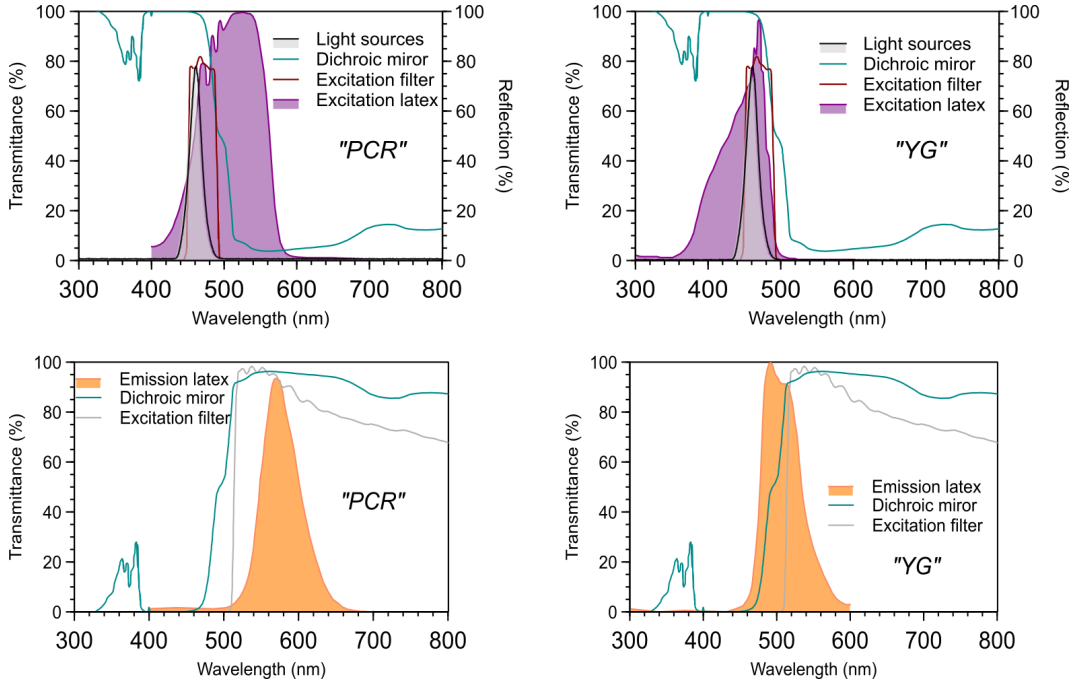

Figure. 4.16 (*top*) Spectra of the light source M470-L (λ_{max} = 470 nm) superposed on the spectra of the excitation filter (BP420-480), dichroic mirror (DM500) reflection and excitation latex. (*bottom*) Emission spectra of latex spheres superposed on the spectra of the dichroic mirror (DM500) and the emission filter (BA520IF). (*left*): Latex with "polychromatic red" (PCR) fluorophores. (*right*): Latex with "Yellow-Green" (YG) fluorophores.

4.3.5 Microscope and camera calibration

The video camera was installed on binocular port of the microscope using a home-built opto-mechanical adapter.

Calibration using a calibration target (Olympus) gave the correspondence between the size in the digital image (pixels) and the physical size of a feature in the object plane. A typical image of the calibration target is shown in Figure 4.17.

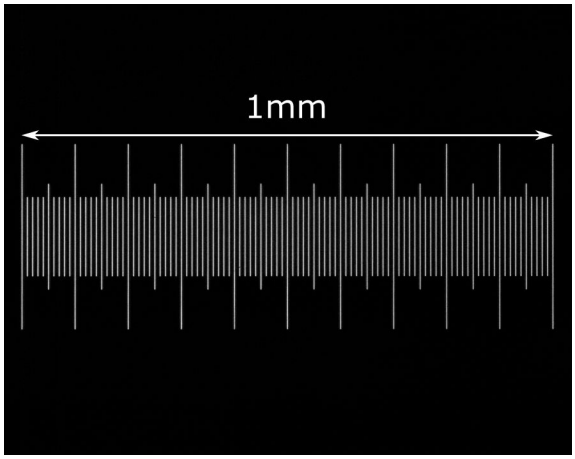

Figure. 4.17 Digital camera image of the calibration target obtained using a 10x magnification objective.

Calibration as a function of the microscope objective led to the table below giving the transformation between the number of pixels and the physical real size. Measurements were done using the monochrome Ximea camera "xIQ, MQ013CG-ON" (CMOS, 2048x2048 px, pixel size: 5.5 μm).

Objective	Reference	Measured (nm/px)	Calculated (nm/px)
60x	LCPlanFi, NA0.70	90.8	91.7
40x	LCPlanFi, NA0.60	136.2	137.5
20x	MPlanN, NA0.40	267.9	275
10x	CPlanFL, NA0.30	546.5	550
4x	PlanN, NA0.10	1354.4	1375

Table 4.2 Table summarising the objective used and the corresponding size of one pixel. The calculated values were obtained for the (square) pixel width of the camera (5.5 μm) and the magnification of the objective.

The microscope will be used in this thesis using two detection channels. The digital camera installed on the binocular port and an optical spectrometer installed on the side port.

4.4 Dark-field illumination in PDMS microsystems

In view of the efficient light scattering by gold nanoparticles of sufficient diameter (>60 nm), the set up was mainly used with dark-field light illumination. The light was injected through the side of the PDMS which acted as a "light guide" for side illuminated dark-field.

4.4.1 Optical properties of PDMS

In this work, PDMS was selected for its several specific advantages not in the least for its optical properties. First, it enables the rapid prototyping of new systems. Furthermore, it is compatible with aqueous solutions and biological materials. PDMS is optically transparent, and has reasonable optical quality. This facilitates optical microscopic and optical spectroscopy observations.

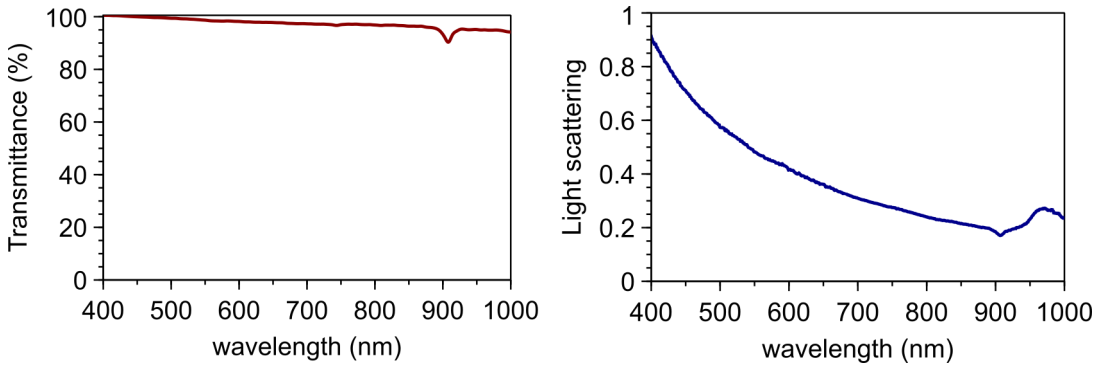

Figure. 4.18 (*left*) Transmittance spectrum of PDMS polymerised directly in 1 cm spectroscopic cuvette. (*right*) Light scattering spectrum of PDMS in the same cuvette.

These specific optical properties offer an excellent material to use for optical measurements. As seen in the Figure 4.18, the window of transparency is ideal in the UV-Vis range and have a low light diffusion.

4.4.2 Optical modelling of side illuminated dark-field

A model of the optical path used was designed with Optgeo software (Version 2.20) which does geometrical optics (ray tracing). It uses Snell's law $n_1 sin(i_1) = n_2 sin(i_2)$; with n_1, refractive index of the first medium; n_2, refractive index of the second medium; i_1, angle of incidence relative to the normal; i_2, angle of the refracted beam relative to the normal.

Light rays are considered individually at varying angles of incidence and their propagation through the microsystem device was studied. The refractive index chosen is 1.00 in air, 1.40 in PDMS, 1.33 in water and 1.52 in glass. Limiting cases of total reflection inside the PDMS slab can be determined for each incidence angle θ_1 between 0° and 90° (Figure 4.19). Three cases were taken into account (1) The light enters via the side of the PDMS and is directed to the glass substrate without interaction with the microchannel (grey path). (2) The light enters the side of the PDMS and hits the

side wall of the microchannel (green path). (3) The light enters via the side of the PDMS and is oriented to the top of the microchannel (red path).

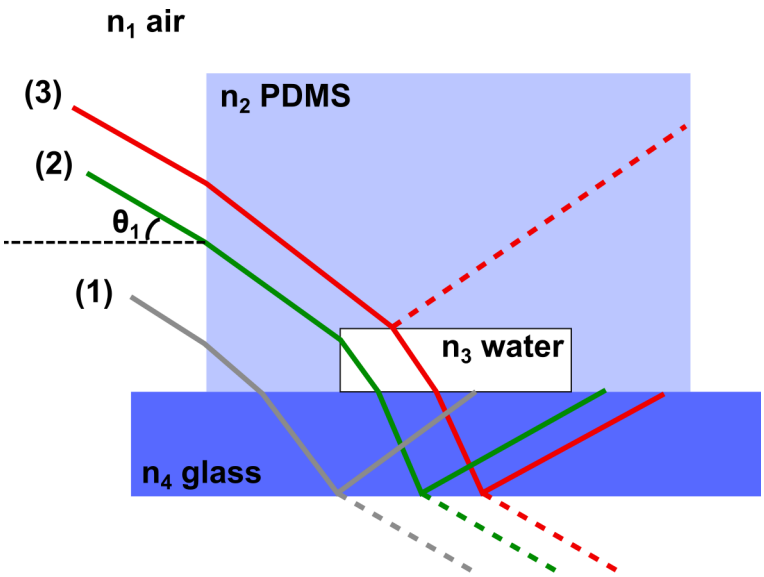

Figure. 4.19 Three different cases to summarise the light propagation in the microfluidic system.

Case (1) shows a total internal reflection of the light by the glass layer when the angle of incidence is between 0° and 79°. Beyond 79° the light is refracted and exits the glass substrate via the bottom, potentially adding to stray light in the microscope's detection part. In case (2), the suitable angle of total reflection between the glass layer and the air is between 0° and 62°, above this angle the light is refracted at the glass-air interface. In case (3), the light ray enters the microchannel wall, indicating that the better compromise is an incidence angle between 26° and 78° to have the maximum light intensity in the microchannel and to avoid light after exiting the substrate.

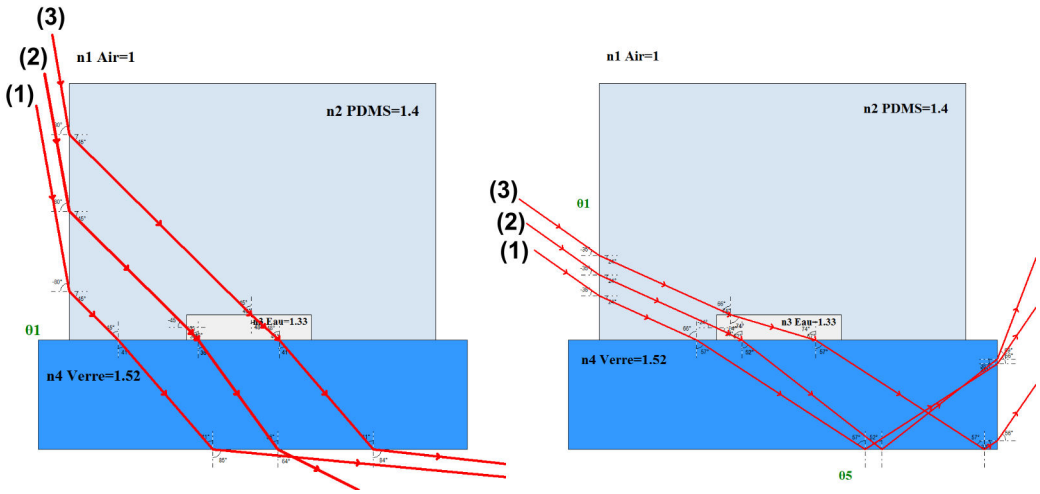

Figure. 4.20 (*left*) Examples of bad angles for light injection in the system used in this work leading to high background noise. (*right*) Best angles to avoid stray light from reflections in the microfluidic system.

Overall, angle of incidence between 26° and 62° (with respect to the normal o the side wall) is expected to lead to an ideal dark field illumination in the microchannel.

4.4.3 Experimental realisation

In previous experiments carried on in our group, side illuminated dark-field was achieved in a rudimentary way by simply sticking small-angle emitting low-power LEDs (3 mm housing) to the side of the PDMS.[156, 157] This method did not allow optimisation of the light focus onto a specific part of the microfluidic channel. In this thesis, the system was improved by focussing the output of a fibre-coupled high power LED onto the microfluidic channel via the side of the PDMS slab.

Experimental pictures in Figure 4.21 show the optical rays light injected into a PDMS device using the collimator placed at a distance of ten centimetres to the microfluidic channel side.

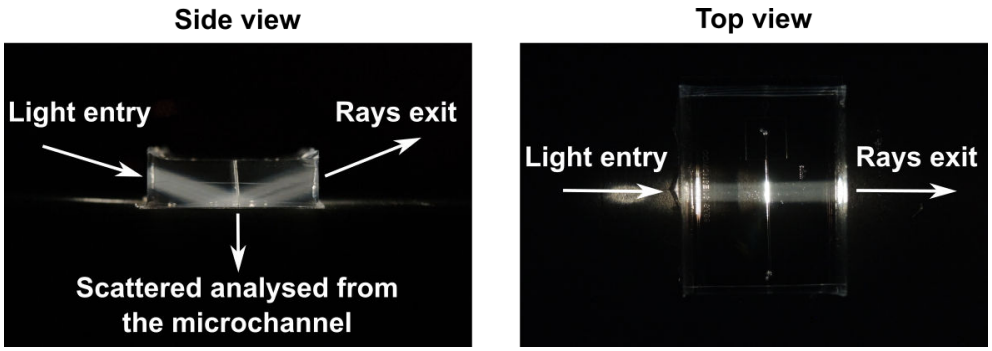

Figure. 4.21 Pictures coupling light into the PDMS from the side with a 25° incidence angle, using a fibre-coupled LED connected to a collimator and focused with an additional lens. (*left*) Side view (*right*) Top view.

Both the rudimentary LED illumination and the more sophosticated focused beam illumination were compared by imaging 100 nm gold nanoparticles deposited on the microfluidic channel substrate. For optimal comparison the same area was imaged. The digital microscopic images were analysed by plotting the histogram along a line with individual scattering particles. (see Figure 4.22)

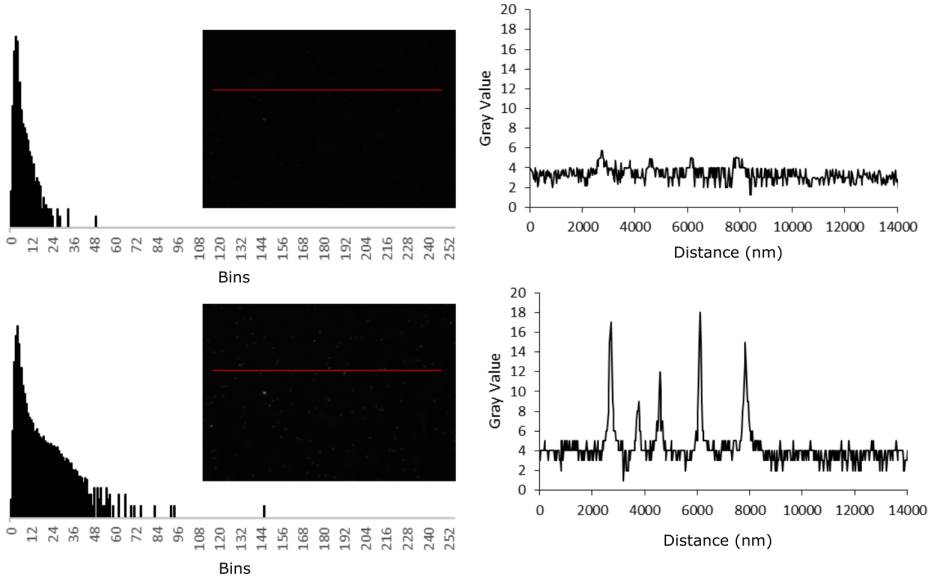

Figure. 4.22 Comparison of the (*bottom*) new high power white LED illumination to the (*top*) old method using a sample of 100 nm gold nanoparticles deposited on the bottom of a microchannel. (*left*) Histogram of the red line from the image (*right*) Grey value as a function of the distance along the red line on the image.

As shown Figure 4.22, the intensity signals of gold nanoparticles were increased by a factor of three for the same exposure time. While the background noise remained constant, leading to a significant increase in signal to noise of the dark-field detection of gold nanoparticles.

4.5 Real-time experiment control electronics

In order to obtain reproducible experiments, precise control of the timing of the electric field switching, video recording and light switching is needed. A simple electronics box based on an Arduino micro-controller was built.

4.5.1 Electronic synchronisation

LED illumination and electric field switching were controlled using home-built real-time trigger electronics based on an Arduino Uno board running custom microcode. The Arduino is a small computer built around an Atmel 320 microcontroller. The Arduino environment allows for directly programming the microcode running on the controller. In the following, the electronic circuit that interfaces the Arduino microcontroller to the outside world was described. This involves a hardware switch to start/stop the timing sequence (section 4.5.2), a control output for driving the function generator that drives the electric field (section 4.5.3) and a control output for the high power LED driver.

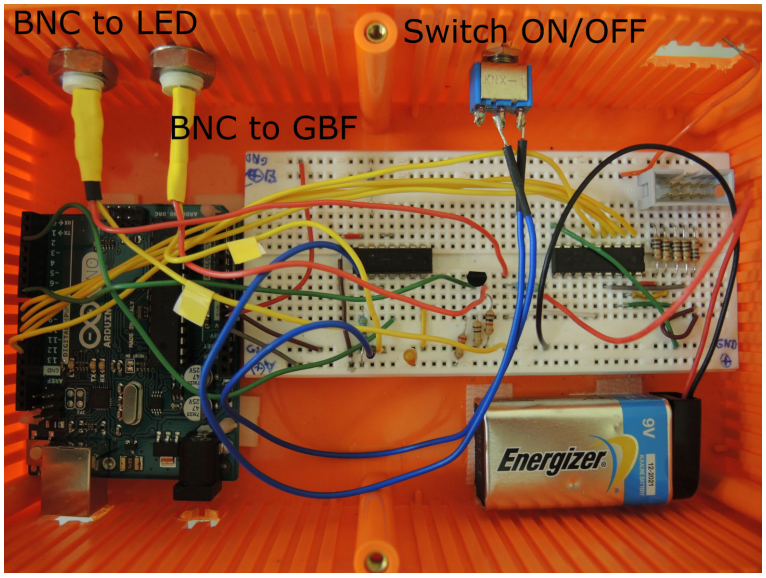

Figure. 4.23 Photo of the box containing electronic controller.

4.5.2 Hardware switch for program control

In order to change the state of the microcode running on the Arduino, between "running" and "stand by", a physical switch was interfaced to the Arduino TTL input (pin 2 on the board). The "stand-by" state is necessary to allow the operator to change samples to connect the device. In this state, the AC electric field is inactive (amplitude set to 0 V) but the illumination is switched on to allow observation.

When the switch is put into "run" mode, the experimental sequence is run repeated (*e.g.* blink illumination, switch "ON" electric field, wait, switch "OFF" electric field, blink, ... etc.). The blinking of the illumination is used as a synchronisation marker in the recorded video.

The circuit for interfacing the hardware switch is given in Figure 4.24. It uses a Schmitt-trigger inverter to "bounce back" the signal of the switch, and as a buffer to protect the Arduino from accidental electric damage. Here, two inverters were placed in series, which is not strictly necessary.

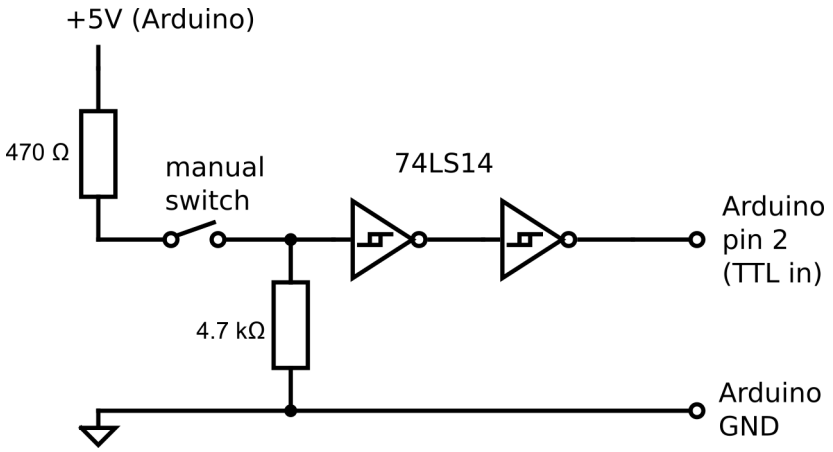

Figure. 4.24 Electric circuit for interfacing a physical switch to a digital TTL input of the Arduino board.

4.5.3 Control of the electronic function generator

The electric field in the microfluidic device is generated by applying an electric potential to the thin-film microelectrodes. This potential is provided by a function generator (ELC Centrad GF 266). The frequency and pre-set amplitude of the generated sinusoidal signal is set via the external RS 232 computer interface.

The amplitude of the signal generated by function generator can be modulated by applying a voltage (0...1.55 V) at the external modulation input. By applying a voltage of 1.55 V the amplitude is set to zero (electric field switched "OFF"). The amplitude is 100% of the pre-set value when the voltage is set to 0 V. Therefore, in order to switch "OFF" and "ON" the electric potential applied to the microelectrodes, an output controlled is needed by an Arduino TTL signal, that is able to drive the modulation input of the function generator to 0 V and to 1.55 V. The MOSFET-based circuit in Figure 4.25 was found to behave satisfactorily.

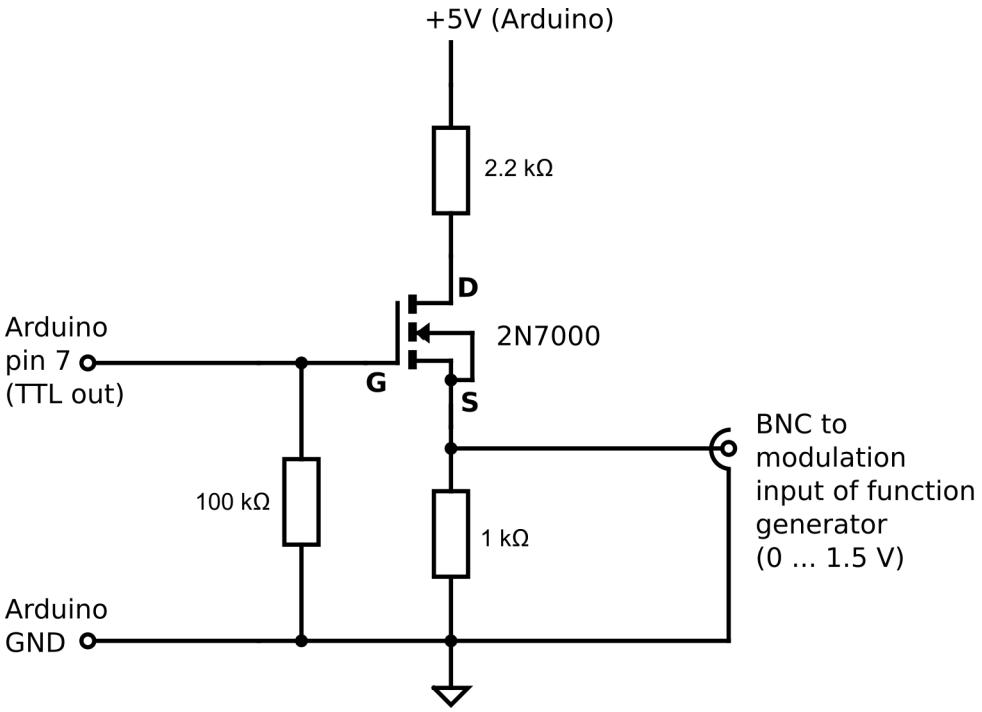

Figure. 4.25 Electric circuit used to switch the voltage applied to the function generator input

The "2N7000" MOSFET is a small low-power MOSFET with switching characteristics for interfacing with the Arduino TTL output (pin 7 of the board). The Arduino provides a very clean TTL voltage: it is really at +5 V when the output is logical 1, and really 0 V at logical 0. This feature does that the MOSFET can be used in the "switchable voltage divider" configuration shows, which pulls the BNC output down to 0 V with pin 7 at logical 0, and up to 1.55 V at logical 1.

4.5.4 LED controller

For videomicroscopy, it is essential to synchronise the recording to the switching of the electric potential of the function generator. This synchronisation was achieved by blinking the illumination, *i.e.* switching it off for 50 ms. The blinks are seen in the video as one or two dark frames. The analysis of the recorded videos was started at these frames. The high power LEDs were driven by a four-channel LED driver from

Thorlabs (DC4104 ,1 A ,5 V). This driver has an external control input. The LED drive current is controlled by applying a voltage between 0 and 10 V to the control input. Ten volts correspond to a LED current of 1000 mA (the maximal value). The electronic circuit used for switching the LEDs is shown in Figure 4.26.

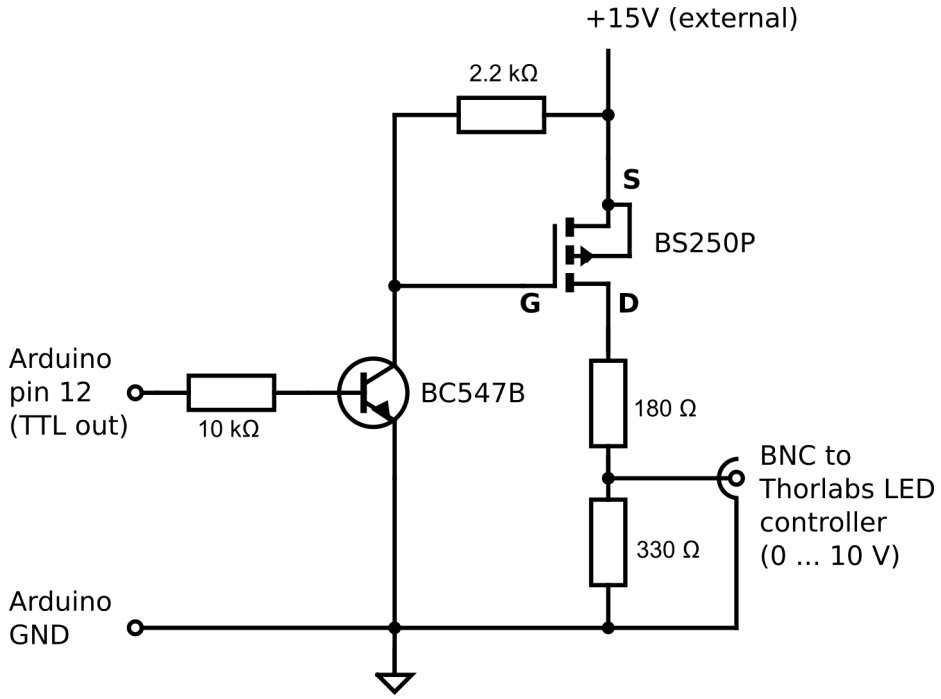

Figure. 4.26 Electric circuit used to control the voltage applied to the LED driver input.

The switching on the output was again achieved by a switchable voltage divider configuration. However, the switching between 0 and 10 V requires an external voltage source. Also, a different MOSFET configuration was used, requiring an additional bipolar drive transistor. The synchronisation of the function generator and the LED illumination enables the analysis of images knowing perfectly the start of each dielectrophoresis cycle. The aim was to analyse the dielectrophoresis of small particles in solution by analysing the video microscopic sequences recorded by a camera. This is further explained in Chapter 5.

4.5.5 Microfluidic flow control

In this thesis, only pressure driven flow was used to operate the microfluidic devices. Two types of controllers were used.

The first type was a plastic screw syringe (Jeulin, total volume 60 mL, Evreux, France). Using this purely mechanical syringe the pressure difference between entrance and exit on the microfluidic channel was controlled. Pressure was monitored using a digital pressure meter (Jeulin).

As second controller, the Fluigent MFCS-EZ microfluidic flow controller was used to drive the pressure at the entrance of the microfluidic channel above atmospheric pressure. The range of use is 0 to 69 mbar corresponding to a flow rate of 0 to 44 µL/min for a typical PDMS microchannel seen previously in section 4.2.4.

4.6 Conclusion

The electro-microfluidic system for studying dielectrophoresis of nanoparticles on the microscale was described in terms of microfabrication and characterisation of microelectrodes and microfluidic channels. Both parts were manufactured with good reproducibility.

More generally, each part of the overall system was described in order to not omit critical parameters for our experiments. The electrical connection, optical properties, microscope and image analysis were described in order to enable reproducible quantitative measurements for the understanding of the dielectrophoresis of small particles.

The microscopic work bench is very versatile. Three observation modes are available (1) transmitted light, (2) wide-field epifluorescence and (3) dark-field light scattering with side illumination of the microfluidic system.

The electro-microfluidic device is also adaptable. Different types of electro-micromanipulation can be done depending on the shape and placement of the electrodes by changing the mask for photolithography. Furthermore, electric field applied at the electrodes can be adjusted in terms of frequency, amplitude and "ON" and "OFF" times. Last but not least, it is possible to generate a controlled flow inside the microfluidic system that can be adapted for the characterisation of different samples. Finally, the detection chain may be modified to implement different spectroscopic analysis methods. For example a spectrophotometer, an avalanche photodiode (APD) or a camera can be positioned at the exit port of the microscope.

In this thesis, the set up was configured for on videomicroscopy and optical spectroscopy of gold nanoparticles in microfluidic channels in the presence of a dielectrophoretic field.

Chapter 5

Dielectrophoretic capture of sub-200 nm gold nanoparticles

This chapter describes dielectrophoresis measurements. This work is original due to measurement of the dielectrophoretic response of particles with a diameter smaller than 200 nm. These particles are not easily detectable using traditional techniques such as brightfield microscopy.

A better understanding of the dielectrophoresis of sub-200 nm Brownian nanoparticles in water will aid in the further development of DEP-based methods for nanoparticle characterisation,[158–160] separation[161] and assembly of superstructures.[162–164] Equation (5.1). It describes the parameters that change the dielectrophoretic response of particles in a fluid medium.

$$\langle \mathbf{F}_{DEP} \rangle = \frac{1}{4} V_p \mathrm{Re}[\tilde{\alpha}] \nabla |\mathbf{E}|^2 \tag{5.1}$$

In this expression, V_p is the volume of the particle, and $\tilde{\alpha}$ is the effective complex polarisability of the particle in the medium, of which the real part translates into the DEP force and the gradient of the norm of the electric field $\mathbf{E}$.

A summary of forces playing a role inside our set-up will be developed in the first part of this chapter to compare the magnitude of the DEP force to other forces (gravitational, electrostatic). Then one measurement of dielectrophoretic will be described in detailed as an example of the general method applied for each data points in this chapter. Finally, the general Equation 5.1 will be decomposed to validate the link between the varying of different parameters (frequency, Vpp) and the DEP response. This analysis will be done first on well known colloidal solutions (latex spheres) and thereafter on metallic particles smaller than 200 nm of diameter (gold particles).

5.1 Electrohydrodynamics and DEP in our set up

In order to determine the scaling of forces and their influence inside our system, an analysis of forces acting on gold nanoparticles were studied. These forces are composed of gravity, Brownian forces and DEP motion generated.[106] Only spherical particles will be described in the following part in order to keep the discussion simple. This means that the volume of one particle V_p is described as a function of the radius of the particle a, according to

$$V_p = \tfrac{4}{3}\pi a^3 \tag{5.2}$$

5.1.1 Gravitational influence

A particle completely immersed in a fluid displaces an equal volume of fluid. The magnitude of the resulting gravitational force F_g corresponds to the mass of the particle $\rho_p V_p$ minus the buoyancy, $\rho_m V_p$ both multiplied by the gravitational acceleration $|g|$.

$$F_g = \rho_p V_p |g| - \rho_m V_p |g| \tag{5.3}$$

For spherical particles, it is well known that the viscous friction force of a particle F_f can be described using Stokes' law as a function of the viscosity of the medium η and the particle velocity v as

$$F_f = 6\pi\eta a|v| \tag{5.4}$$

For a particle dispersed in a fluid, using the first Newton's law of motion $\sum \mathbf{F} = 0$ we are able to determine the velocity of the particle $|v|$ (also corresponding to the sedimentation coefficient multiplied by the gravitational acceleration) as

$$|v_g| = \frac{\Delta m|g|}{6\pi\eta a} = \frac{2}{9}\frac{a^2(\rho_p - \rho_m)|g|}{\eta} \tag{5.5}$$

5.1.2 DEP force

Referring to the equation 5.1, it is possible to express the dielectrophoretic force with the complex permittivity of the particle ε_p in a medium ε_m (assuming an infinitely thin frontier between particle and medium), as below

$$\langle \mathbf{F}_{DEP}(r) \rangle = 2\pi\varepsilon_m a^3 \mathrm{Re}\left[\frac{\tilde{\varepsilon}_\mathrm{p} - \tilde{\varepsilon_\mathrm{m}}}{\tilde{\varepsilon}_\mathrm{p} + 2\tilde{\varepsilon_\mathrm{m}}}\right] \nabla|\mathbf{E}(\mathrm{r})|^2 \tag{5.6}$$

Following the same approach as above for the gravitational influence, it is possible to calculate the magnitude of the velocity resulting from the dielectrophoresis as

$$|v_{DEP}| = \frac{a^2\varepsilon_m}{6\eta}\mathrm{Re}\left[\frac{\tilde{\varepsilon}_\mathrm{p} - \tilde{\varepsilon_\mathrm{m}}}{\tilde{\varepsilon}_\mathrm{p} + 2\tilde{\varepsilon_\mathrm{m}}}\right] \nabla|\mathbf{E}(\mathrm{r})|^2 \tag{5.7}$$

For gold nanospheres the Clausius-Mossotti factor will be chosen as equal to +1 and the permittivity of the medium as 80.

Using gradient electric field results from the section 5.5.1, it is possible to determine the electric field gradient along the electrode edge.

5.1.3 Brownian motion

The random displacement of the particle follows a Gaussian profile with a root-mean-square displacement, depending on the time that the particle is analysed, D is the diffusion coefficient of the particle. This gives rise to an "effective velocity".

$$|v_{brownian}| = \sqrt{4Dt} = \sqrt{\frac{k_B T}{3\pi a \eta}} \tag{5.8}$$

Where k_B Boltzman's constant, T is the absolute temperature and t is the period of observation.

5.1.4 Which force dominates?

The three forces (gravitational, DEP, Brownian) were calculated as described above. The magnitude of each velocity was compared to others as a function of the particle diameter. The objective was to compare the gravity, Brownian motion and DEP for different voltages applied.

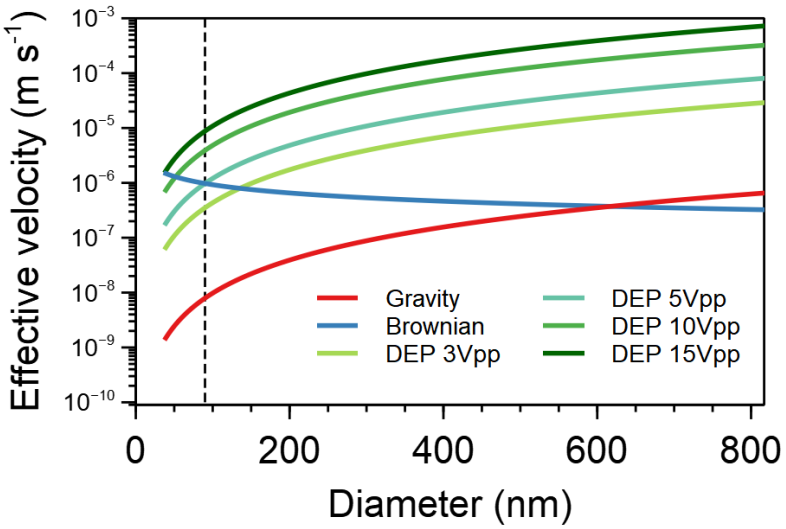

Figure. 5.1 Effective velocity (m s^{-1}) as a function of the particle diameter. The magnitude of the velocity due to DEP is plotted for voltage applied between 3 to 15 Vpp and compared to the magnitude of the velocity due to the gravity and Brownian motion.

By analysing these results we were able to determine the minimal sizes of particles which are sensitive to the dielectrophoretic force. For example, particles with a diameter of 80 nm are the lower limit for capture by pure dielectrophoresis using an electric field amplitude of 5 Vpp.

This first approach helps us to define parameters and limits of our device in terms of dielectrophoresis for the capture of spherical gold nanoparticles. A 3D representation was done in order to define an area of capture around an electrode tip.

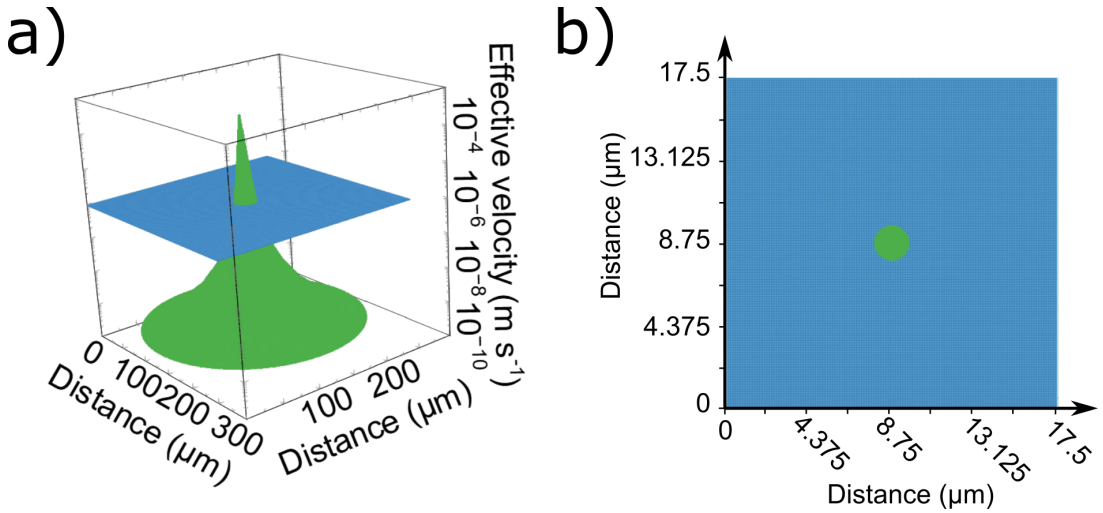

Figure. 5.2 a) 3D plot of the effective velocity due to DEP (m s^{-1}) for a gold nanoparticle of 100 nm diameter. Dielectrophoresis velocity was plotted for applied voltage 10 Vpp (green). It was compared to the effective velocity due to the DEP and Brownian motion (blue). b) 2D plot of the cross section between both effective velocity. The cross spot has a diameter of 1.9 μm.

It is also interesting to look in to the electric field gradient close to the electrode's tips using the COMSOL simulation to determine an area where particles are directly captured due to the dielectrophoresis force. The Figure 5.2 shows results from theoretical application comparing the magnitude of the velocity for a particle affected by the Brownian force and by the DEP force. This figure shows particles close to the tips of the electrodes at different amplitudes of electric field. Looking at Figure 5.2, a circle with a mean diameter of 1.9 μm can be assumed to be a typical size where the

DEP force becomes prominent over the Brownian force around the tips of electrodes. The DEP force topography against others forces can be easily represented using this analysis method.

Following, a general method applicable to our videomicroscopy measurements was described to analyse the dielectrophoretic response of the nano-objects samples. The videomicroscopic measurement of DEP for nanoparticles demonstrates the acquisition cycle and processing of the image's sequences. The videomicroscopic analysis is based on the light intensity measured in each pixel in each frame which is proportional to the amount of particles in the corresponding observation volume. The measurements can be described in 3 steps:

- The videomicroscopy recording;
- The image processing (electronic background subtraction, the background correction);
- The extraction of the intensity evolution as a function of the time

5.2 Methodology for video-microscopic analysis

To analyse the effect of dielectrophoresis on particles, the light intensity and the concentration of particles were correlated at each instant t. The area showing the higher gradient electric field of our system was selected. The area is defined as circle with a radius R_{cap}. For this analysis a method was developed of an original image processing method to avoid stray light in our measurements. In the following subsections the measurement method will be explained step-by-step and a set of measurements will be presented as an example of the analysis. The study will be concerned with the capture of nanoparticles by dielectrophoresis as a function of the applied electric field and time.

5.2.1 Image processing

The Ximea monochrome camera used for the measurements was composed of a 2048 x 2048 pixels CMOS image sensor (5.5 μm / pixel) with a maximum video recording frame rate equal to 90 frames per second (fps). A typical video recording was a stack of images recorded at 50 fps saved into a TIFF file directly from the Ximea software.

The problem with videomicroscopy, was the signal to noise ratio of the camera for these nano-objects with such high fps rates (short exposure times). In order to tackle this problem, the dielectrophoresis analysis was realised by averaging over several cycles of the same sequence, consisting of three seconds of particles capture when the electric field is "ON" followed by five seconds of particles release switching "OFF" the electric field (detailed in the section 5.3.1). Using averaging resulted in one cycle of eight seconds, this procedure was very similar to the averaging of traces in a digital oscilloscope which also enhances the analyte signal over the background noise.

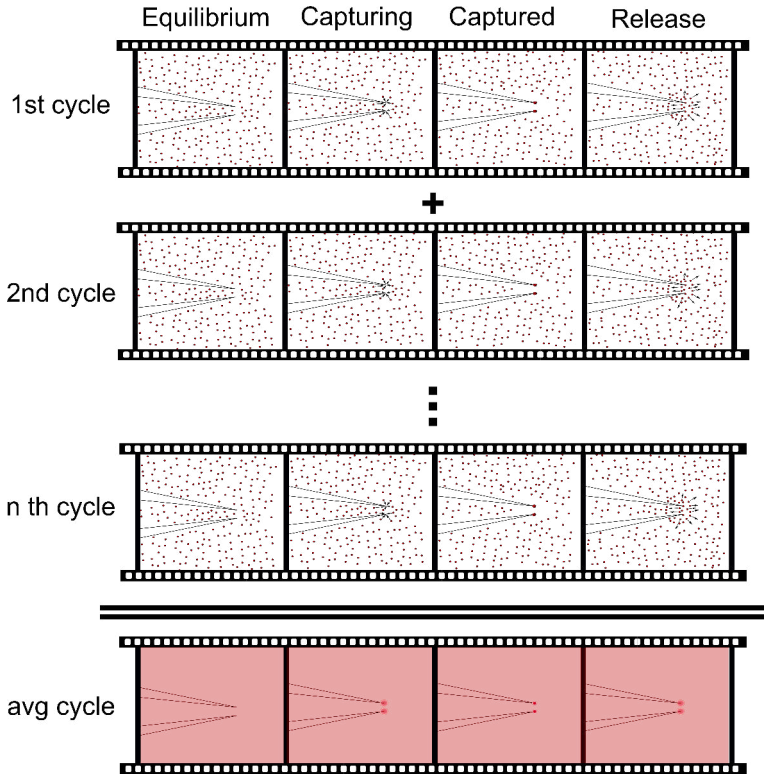

Figure. 5.3 Schematic representation of the sequence of the experiment. A DEP "capture-and-release" cycle is repeated "n" times, while filming the microscopic images near the electrode tips. After recording the full sequence, a "cycle-averaged" video is created by adding up all frames at the same phase of the cycle, giving a videomicroscopic sequence over one DEP cycle that contains the average signal over many cycles. This greatly increase the signal over the background noise, while averaging out the movements of individual particles.

Once the dielectrophoretic principle of the cycling capture has been defined, images corrections will be detailed in terms of intensity data. Images directly saved from the camera are called (I_{Raw}). Firstly, the electronic background ($I_{Electronic}$) corresponding to the record before each measurements series without light illumination was subtracted from the raw data. In this state of correction, it was not possible to directly study the contribution of particles captured in comparison to particles free in solution. In fact, particles stuck to the top of the microchannel contributed to the undesirable background intensity. To solve this sticking problem a last correction was done by subtracting a background image ($I_{Background}$).

$$I_{Studied} = I_{Raw} - I_{Electronic} - I_{Background} \tag{5.9}$$

Finally, the average images sequence shows the spatial distribution in two dimensions of particles around electrodes. This permits us to follow the particles comportment in an AC electric field for each frame and each of its positions.

Baseline verification

Raw images minus background images were realised to create the averaged video. The averaged video-microscopy image stacks were saved and the dielectrophoresis areas capture were used to follow the phenomena. This means that for each measurement (around 25 cycles of 8 seconds) an intensity profile was plotted. The baseline correction of the integrated intensity was done directly from the image processing as see in Figure 5.4.

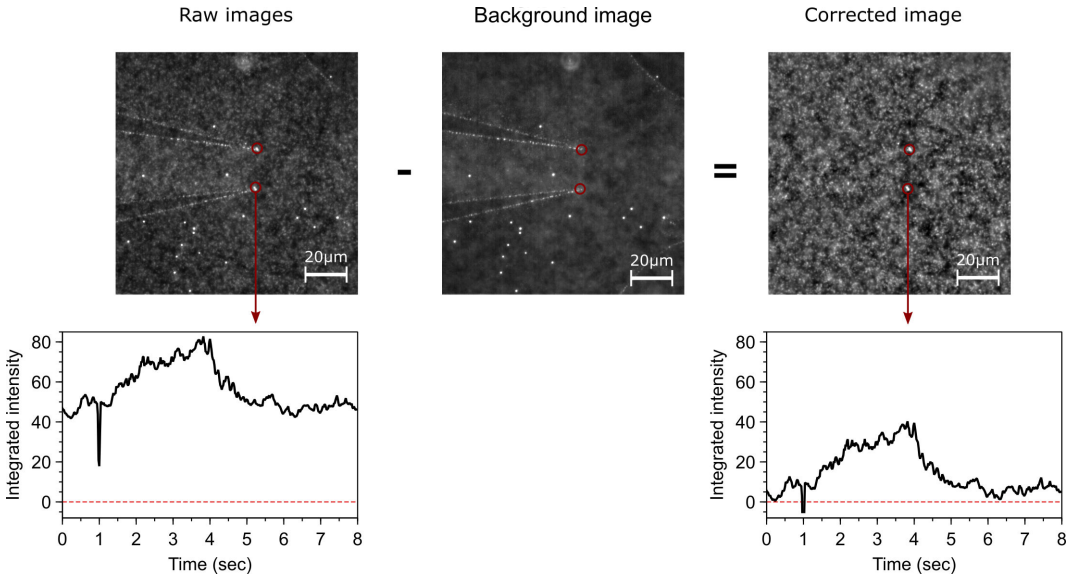

Figure. 5.4 Top: (*left*) Raw image of 100 nm gold nanoparticles in the microchannel dispersed around electrode tips. (*middle*) One of the background images subtracted from the raw images, removing stuck particles and the signal from PDMS and ITO electrodes scattered light. (*right*) Corrected image (*bottom*) Mean intensity profiles averaged from the red circles before correction and after correction.

Once again the image processing shows that only the baseline is modified and does not affect the shape of the signal.

5.3 Dielectrophoresis cycle

The image processing was developed and validated to be physically appropriate. This section shows how the method is used to extract the information from a videomicroscopic recording. An example will be detailed for a series of measurements to analyse the dependence of the DEP capture as a function of the time whilst applying the electric field.

5.3.1 Typical cycle and intensity trends

As shown in the Figure 5.5, a circle of 2 μm of radius ($R_{capture}$) was chosen as the reference for the signal intensity surface and an external radius ($R_{Depletion}$) of 3 μm was chosen for the depletion signal analysed in our images, both were placed at the electrodes tips.

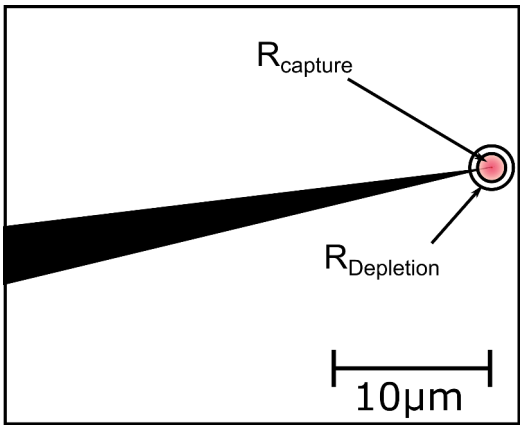

Figure. 5.5 Scheme of the electrode tip's geometry. To scale depletion and capture circle areas of analysis were placed on the schemes.

Below, the dielectophoresis cycle was described for the previously created average sequence using the light intensity evolution over time. Capture of nanoparticles due to DEP leads to an increase in light intensity close to the electrodes over time. When the DEP field is switched off, the previously captured nanoparticles diffuse freely, and the system returns to an equilibrium (I_0) state with an evenly distributed nanoparticles concentration. This simple cycle leads to trends as shown in the figure 5.6.

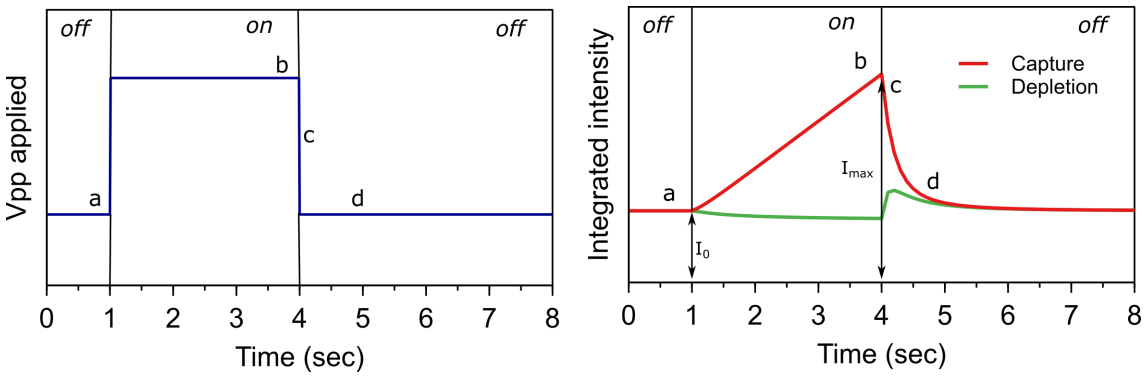

Figure. 5.6 Schematic representation of the sequence of the experiment. (*left*) electrical power supply at the electrodes as a function of time. (*right*) Integrated intensity in the circle determined by $R_{capture}$ placed at the electrodes tips. a) at equilibrium, with E-field switched off ($t = 0s$); at t=1s the LED blink; b) after $3s$ of electric field; c) just after $t = 4s$ when E-field was switched off; d) at $t = 5s$, when captured particles have partially diffused away.

The capture ratio ϕ_{cap} is defined as the ratio of the maximum of the integrated intensity just after release (I_{max}) to the integrated intensity at equilibrium (I_0). This is assimilated equal to the particles' concentration at the capture (C_{capt}) and at the equilibrium(C_0). Shorter, intensities integrated from images will be analysed and assimilated by division using an equilibrium reference (the variation of particles' concentration for a previously selected area).

$$\phi_{cap} = \frac{I_{max}}{I_0} = \frac{C_{capt}}{C_0} \tag{5.10}$$

5.3.2 Characterisation of ITO electrodes using atomic force microscopy

In addition to the characterisation done after the fabrication of electrodes (see Chapter 4). Atomic force microscopy (AFM) characterisation of ITO electrodes was performed after several dielectrophoresis cycles to follow the ageing of the electrodes. The measurements were performed on a Dimension 3100 AFM, where a silicon probe tip was mounted to analyse the samples by sweeping the electrodes by contact. AFM images in Figure 5.7 show the ageing of electrodes by the formation of roughness at electrode edges.

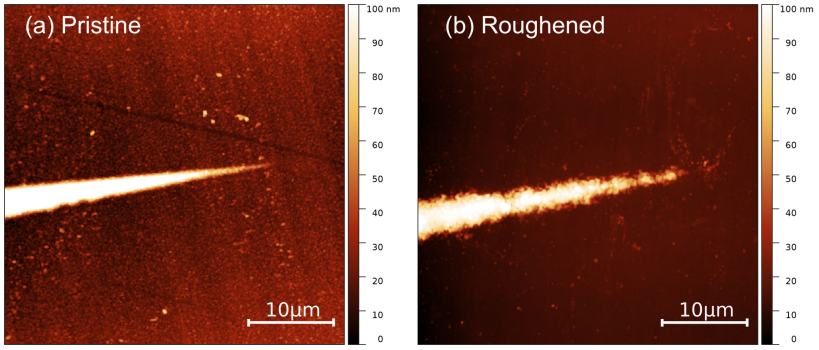

Figure. 5.7 AFM pictures (a) Fresh electrodes after microfabrication (b) Electrodes after more than 200 cycles of dielectrophoresis display important roughness.

It was hypothesised that electrochemical roughening of the electrode surface leads to the formation of a multitude of local zones of strong electric field gradient, effectively creating DEP "hot spots". Also, it was noticed that electrodes tips are non flat patterned coming from the wet etching microfabrication for this type of very small shapes. (see Figure 5.8)

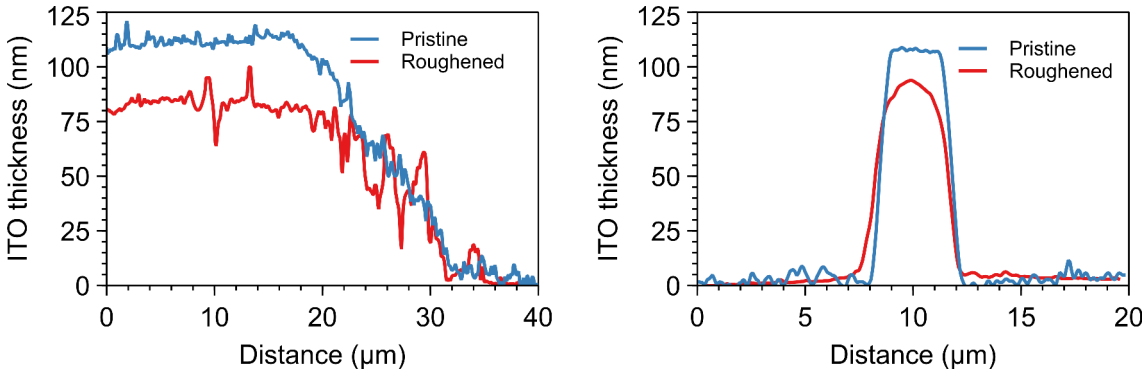

Figure. 5.8 Analysis of AFM pictures. (*left*) thickness of the ITO along the electrodes. (*right*) thickness of the ITO the electrodes using a cross-sectional profile (perpendicular to the electrode).

Depending on the frequency used and the voltage applied onto electrodes we defined the approximate amount of DEP cycles that can be done before the DEP zone starts extending all along the electrodes. (see Table 5.1)

Amplitude (Vpp)	f $\leq$ 0.8	f $\geq$ 1
3	100	$\gg$ 1000
6	10	1000
10	1	1000

Table 5.1 Development of electrode' roughness as a function of the field amplitude and frequency used. Numbers corresponds to the approximate number of DEP cycles which electrodes could support before damage begins to become apparent.

5.3.3 Example of a DEP measurement

In this part, an example of the analysis method was developed in order to describe each step of the method. Gold nanoparticles of 100 nm diameter were used. The dependence of the applied electric field time (DEP "ON") as a function of the capture ratio ($\phi_{cap} = I_{max}/I_0$) was studied in this example. The electric field was switched "ON" for 1, 3, 6, 8 and 10 seconds. For each of these five time frames, the capture ratio was measured in three files of twenty-five cycles (capture and release).

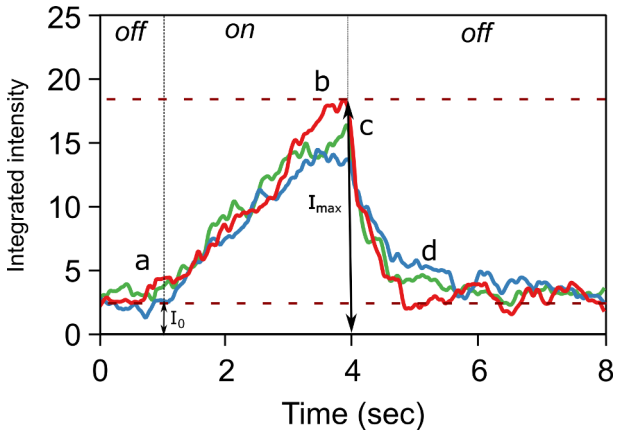

Figure. 5.9 Integrated intensity as a function of time in the monitored area of dielectrophoretic capture of 100 nm gold nanospheres whilst applying a voltage of 6 Vpp, measured using dark-field videomicroscopy (50 fps). The signal was averaged 25 "ON-OFF" cycles. Letters indicated different phases of the cycle: (a) at equilibrium, with E-field switched off (t = 0 s); at t = 1 s the LED blink; (b) after 3 s of electric field; (c) just after t = 4 s when E-field was switched off; (d) at t = 5 s, when captured particles have partially diffused away.

Capture ratios (ϕ_{cap}) were calculated for each recorded video. Three plots were analysed for each time DEP "ON". A confidence interval was also determined from these three measurements and plotted. The trend of the capture ratio can be estimated after analysis which is linear as a function of the time DEP "ON".

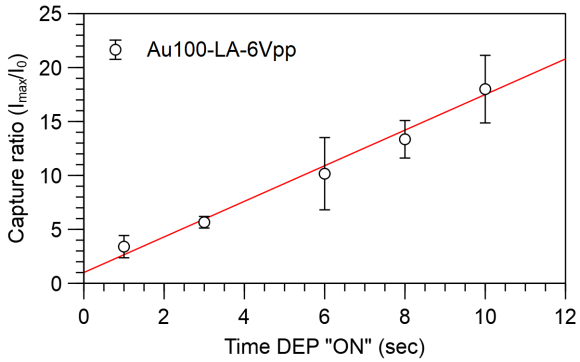

Figure. 5.10 Capture ratio as a function of the electric field time applied. For each cycle, a time of 5 seconds was fixed to let particles diffused freely. The red line corresponds to the fit of experimental dots.

This series of points was fitted and permitted to correlate to the time of electric field application and the capture ratio as seen in equation 5.11. Equation 5.11 is valid for Au100-LA (for our home-made suspension solution) for an AC electric field with an amplitude of 6 Vpp and a frequency of 1 MHz.

$$\phi_{cap} = 1.65\ t_{ON} + 1 \tag{5.11}$$

In this section, the general method has been described and shows how to determine the dielectrophoresis dependence as a function of the DEP "ON" time. In the following, all measurement points are averages of three different measurements and 95% of confidence interval are given.

5.4 Comparison with results from literature

To validate our dielectrophoresis system we were compared our system and method of measurement with that of published studies on latex particles. For this we were analysed the variability of the Clausius-Mossotti factor (CMF), which is an indicator of the dielectrophoresis response for nano-particles. By scanning the frequency and analysis of the response we have studied reliability of our measurements.

5.4.1 Cross-over frequency

For polystyrene latex particles, the behaviour of the CMF is well-known and has been confirmed in many different experiments. The CMF $\tilde{f}_{CM}$ can be calculated from the complex permittivities $\tilde{\varepsilon}_{m/p}$ according to equation 5.12 (subscripts m for medium, p for particles) :

$$\tilde{f}_{CM} = \frac{\tilde{\varepsilon}_p - \tilde{\varepsilon}_m}{\tilde{\varepsilon}_p + 2\tilde{\varepsilon}_m} \quad \text{with} \quad \tilde{\varepsilon}_{p/m} = \varepsilon_{p/m} - i\frac{\sigma_{p/m}}{\omega} \tag{5.12}$$

Where $\sigma_{p/m}$ are the conductivities of the particle and the medium, respectively, and ω is the angular frequency of the applied AC electric field. In the present case we have $\varepsilon_m = 78.5\varepsilon_0$, and $\varepsilon_p = 2.55\varepsilon_0$. The dependence of the σ_m is directly linked to the CMF.

For small particles, the conductivity σ_p is not only determined by the conductivity of the bulk material but also by its surface conductivity. The overall conductivity of the particles can be calculated from the bulk conductivity of the nanoparticle core material $\sigma_{(p,bulk)}$ (vanishingly small for polystyrene, $\sim 10^{-16}$ S m^{-1}), and from the radius (a) of the particle and its surface conductance K_s. For very small (< 1 μm) polystyrene latex particles, the conductivity is dominated by the surface conductivity. We found the overall surface conductivity to vary slightly between different particle diameters, likely due to differing surface densities of ionised groups. All conductivities are within the range typically found for latex particles.

$$\sigma_p = \sigma_{(p,bulk)} + \frac{2K_s}{a} \tag{5.13}$$

A first approach was realised to analyse the dependence of the CMF as a function of each configurable parameters. The diameter of the particle, the conductivity of the medium and the particle surface conductance, link to that of the previous particles which were studied to fit on our colloidal solution inject in the electro-microfluidic system; the microscope was used as fluorescence contrast (see Chapter 4).

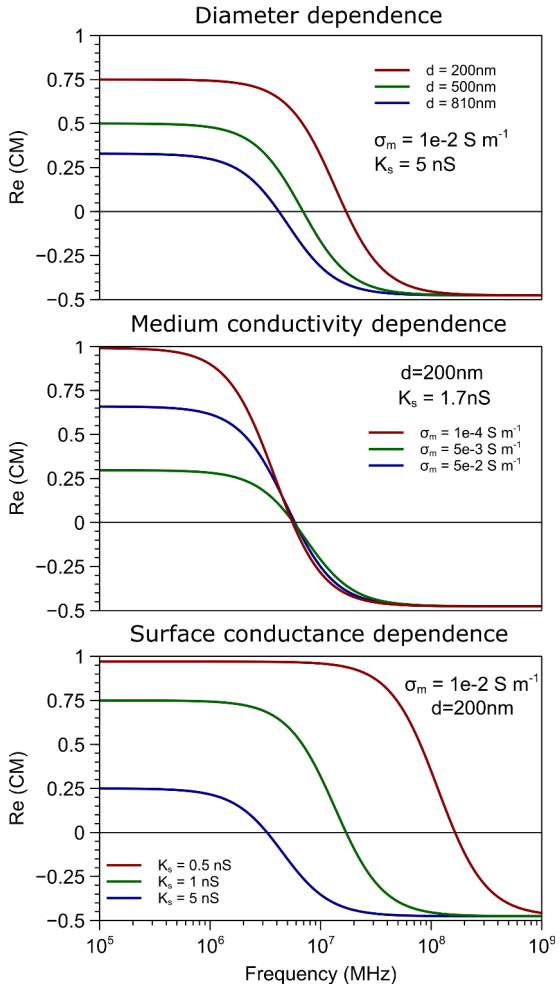

Figure. 5.11 (*top*) Theoretically calculated CMF as a function of the diameter of the particles (d), with $\sigma_m = 1.10^{-2}$ S m^{-1} and $K_s = 5$ nS. (*middle*) CMF as a function of the conductivity of the medium (σ_m), with $d = 200$ nm and $K_s = 1.7$ nS. (*bottom*) CMF as a function of the particle surface conductance (K_s), with $d = 200$ nm and $\sigma_m = 1.10^{-2}$ S m^{-1}.

As shown in Figure 5.11, an increase in diameter of the particle leads to a decrease of the crossover frequency and a decrease of the CMF values at the low-frequency plateau. By varying the medium conductivity we observe that the crossover frequency does not depend on medium conductivity. However, the CMF values change at the low-frequency plateau. Finally the particle surface conductance was varied for a 200 nm diameter particle. This resulted in a large change of the crossover frequency value and also to a change of the CMF plateau value.

5.4.2 Comparison with the literature

Using the methodology described in Chapter 4, we have investigated the dependence of the capture ratio on the frequency of the AC electric field at constant amplitude of the applied potential. For comparison with data obtained using other methods in published literature,[165–167] we first studied the dielectrophoresis of polystyrene particles (latex spheres).

Polystyrene latex particles were dispersed in the same medium as the gold nanoparticles (0.2 mM Na-lipoate, 1 mM NaOH in water). The measured conductivity of this medium is 2 x 10^{-2} S m^{-1}. The DEP of these particles is well known to be frequency-dependent. At constant field amplitude, the amount of captured particles decreases towards higher frequencies, since the dielectrophoretic force becomes weaker. At a certain frequency, the crossover frequency, the dielectrophoretic force changes sign, turning from positive DEP to negative DEP, meaning that DEP pushes particles away from the capture zone. The weakening of the DEP force on latex particles with increasing frequency is indeed observed as a decrease in the capture ratio in our measurement. (Figure 5.12)

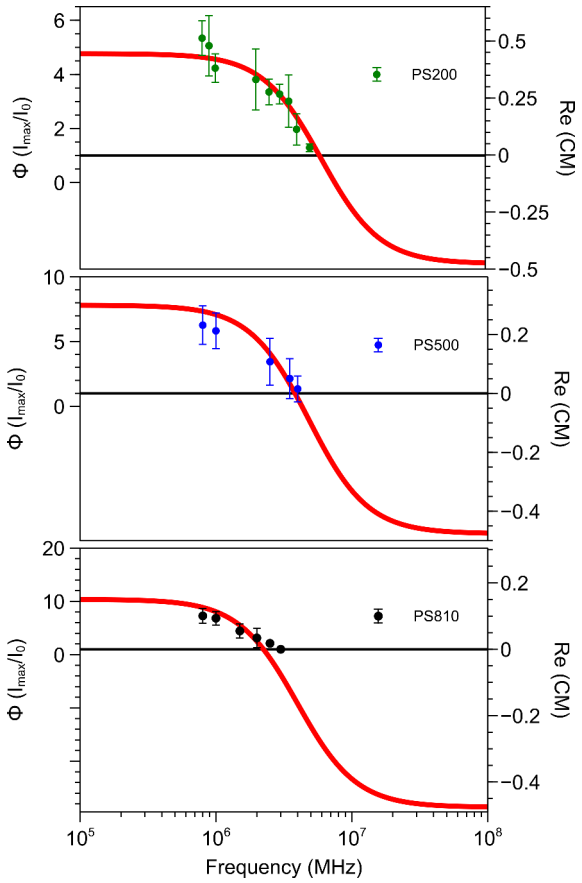

Figure. 5.12 Experimental capture ratios for polystyrene particles (200, 500, 810 nm) as a function of the frequency at 7 Vpp to determine the crossover frequency. Red lines correspond to model calculations of the Clausius-Mossotti factor, using $\varepsilon_m = 78.5\varepsilon_0$, $\sigma_m = 1\text{x}10^{-2}$ S m^{-1}, and $K_s = 1.7$ nS (PS200), $K_s = 2.8$ nS (PS500), $K_s = 3.1$ nS (PS810).

Figure 5.12 shows the dependence of the capture ratio for latex particles on the field frequency, at constant amplitude of the applied voltage. From this dependence we can estimate the crossover frequency for each diameter of latex sphere particles.

Comparatively, it was not possible to directly observe negative DEP for all particles. In fact the signal ratio of the noise is too important to be really significant. An example was detailed in Figure 5.13.

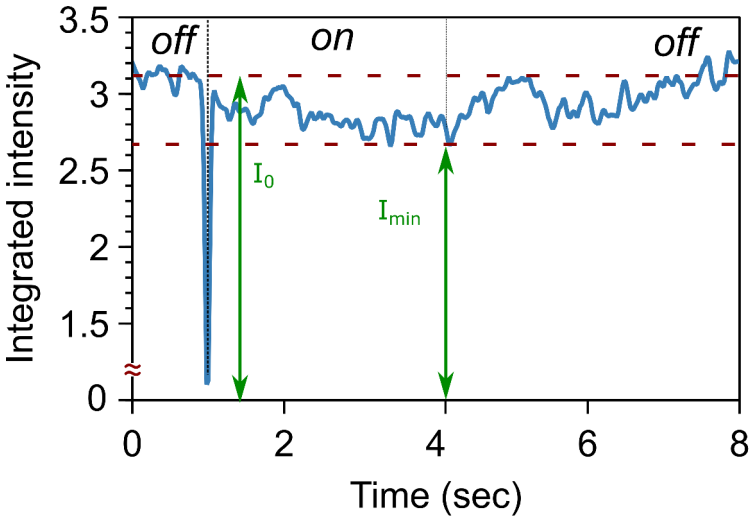

Figure. 5.13 Integrated intensity as a function of time in the monitored area of dielectrophoretic capture of 200 nm latex nanospheres applying an electric field amplitude of 7 Vpp and a frequency of 6 MHz using fluorescence videomicroscopy (50 fps). The signal was averaged 25 "ON-OFF" cycles.

The crossover frequency could be reliably extrapolated from the decreasing capture ratio with increasing frequency.

The crossover frequencies, 5 MHz for 200 nm 4 MHz for 500 nm, 2 MHz for 810 nm latex spheres, were well in line with observations in the literature. Moreover, we found that the decrease of the capture ratio for the latex particles as a function of rising frequency followed the CMF predicted by the theoretical model. For low capture ratios, the capture amplitude (= capture ratio minus one) is proportional to the dielectrophoretic force. The behaviour of the capture ratio as a function of electric frequency should therefore follow directly the evolution of the real part of the CMF.

This proves that our methodology yields results that are consistent with existing literature.[165–167]

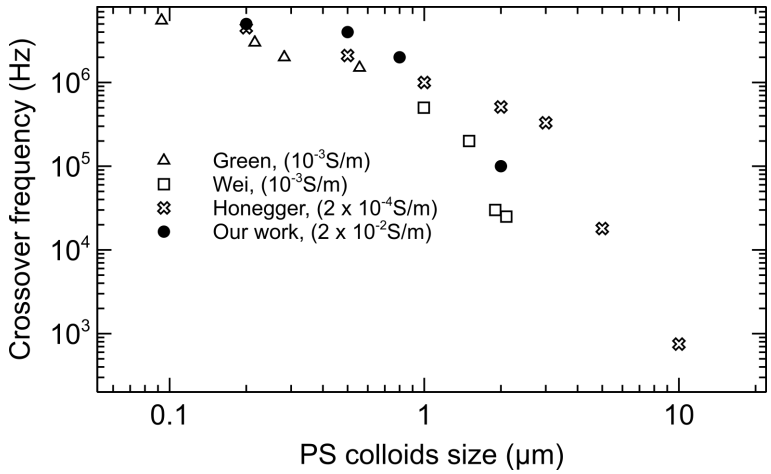

Figure. 5.14 DEP crossover frequency for polystyrene latex particles: comparison of determination using the capture ratio in microfluidic system carried out in the study, and values from the literature. Capture ratios were measured for all polystyrene latex particles, except particles of 2 μm diameter which were analysed only by direct visual inspection of DEP-induced particle motion.

5.5 Dielectrophoresis of gold nanospheres

After confirming the agreement between our measurement of polystyrene spheres with measurements published in the literature, we now focus on the study of the dielectrophoresis of particles smaller than 200 nm of diameter.

5.5.1 COMSOL simulation of our system

In this section the electro-microfluidic chip will be modulated using the finite element method, in order to estimate the magnitude of the dielectrophoretic force and the topography of the DEP force field. COMSOL multiphysics software (version 5.2a). Following Equation 5.1, the effective time-averaged dielectrophoretic force at position $\mathbf{r} = (r_x, r_y, r_z)$ is calculated from the effective polarisability of the particle $\tilde{a}$ its volume V_p and the gradient of the norm of the electric field E.

$$\langle \mathbf{F}_{DEP}(\mathbf{r}) \rangle = \frac{1}{4} V_p \mathrm{Re}[\tilde{a}] \nabla |\mathbf{E}(\mathbf{r})|^2 \tag{5.14}$$

The electric field for our device geometry was calculated from the electrostatic potential obtained by solving the Laplace equation in three dimensions. The substrate was modelled as silica glass ($\varepsilon_{glass} = 2.09$). The experimental planar electrode geometry was reproduced; the electrode tips were rounded with a radius of 0.25 μm. The thin-film electrodes were approximated as infinitely thin equipotential. An applied potential difference of 10 V between the electrodes was used. The medium was water ($\varepsilon_{water} = 78.5; \sigma_m = 1.10^{-2}$ S m^{-1}), enclosed in a chamber of PDMS ($\varepsilon_{PDMS} = 2.75$) dimensions $[l, w, h] = [650, 400, 100]$ μm.[115]

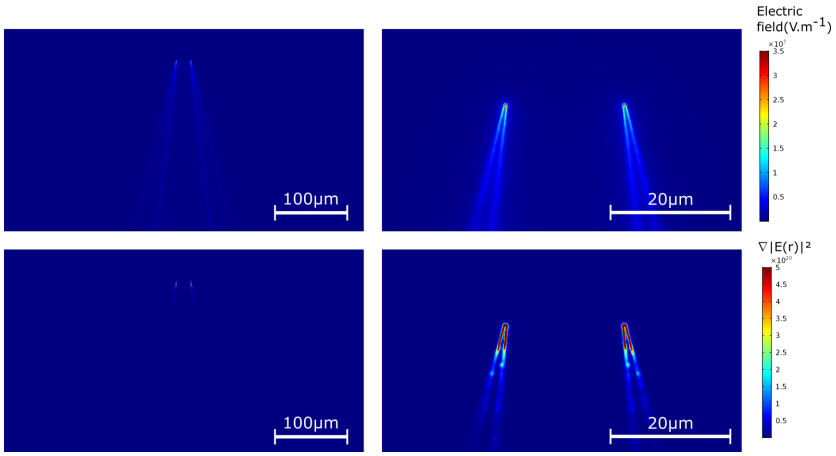

Figure. 5.15 (*top*) Top view of calculated electrical field strength on electrodes in the microchannel in the electrode plane. (*bottom*) Top view of gradient of the squared norm of the electric field.

Using these results we are able to extract the electric field gradient profile around electrodes tips. This one was used in the section 5.1.4.

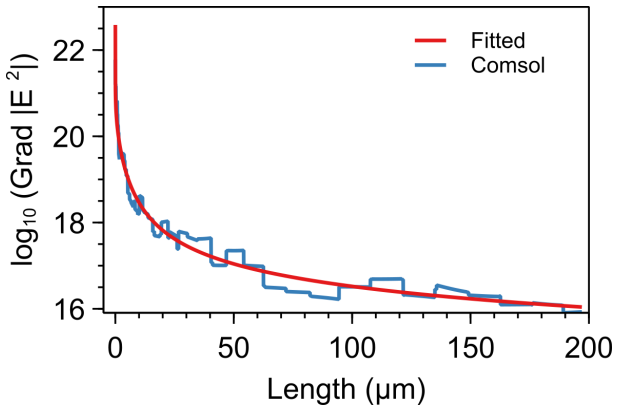

Figure. 5.16 Electric gradient square along the electrode extract from the COMSOL simulation of our system

Using the CMF and the radius of the gold nanoparticles (a = 50 nm), we can calculate the dielectrophoretic force field (which is proportional to the gradient of the squared norm of the electric field and has identical topology). A CMF of +1 is taken in line with literature observations, as described in section 5.5.3. The side view of the magnitude of the force is shown in Figure 5.17. This demonstrates that the force-field is concentrated at the electrode tips. By choosing a lower threshold value of $\sim 2.10^{-11}$ N we can define a "DEP capture zone" that has a radius of 2 μm.

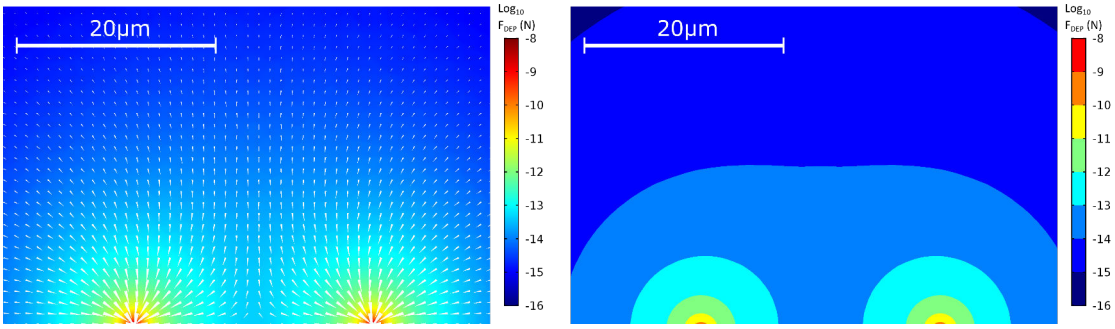

Figure. 5.17 (*left*) False colour image (side view) of decadic logarithm of the magnitude of the dielectrophoresis force near the electrode tips. The direction of the force is represented with arrows. (*right*) Threshold false colour image with decadic logarithm of DEP forces clarifying the radical dependence of the force around the electrode tips.

From this simulation and from results in section 5.1.4, we have fixed a circular area with a diameter of 2 μm around each electrode tip to obtain the maximum signal

from the video-microscopy. This permitted us to analyse the dielectrophoresis of gold nanoparticles with a high definition.

5.5.2 Reproducibility of DEP measurements

In order to estimate the uncertainty due to device-to-device variations, we measured the same sample (100 nm gold nanospheres in 0.2 mM Na-lipoate, 1 mM NaOH in water) in four separate devices. For each device, at least three independent measurements were carried out over several days. As shown in Figure 5.18, the measurement of the capture ratio of the same sample in different devices is reproducible to within 20%.

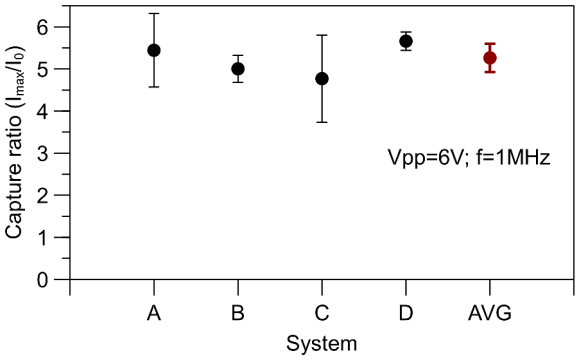

Figure. 5.18 Capture ratio at t = 4 s of particles release as a function of the device at 6 Vpp and frequency 1 MHz. Data points indicate individual measurements in different devices. Red data point represents the meaning of all points with the standard deviation (95% confidence interval) coming from the experiment measurement.

5.5.3 Frequency dependence of the DEP factor for gold nanospheres

To analyse the frequency-dependence of the capture ratio of gold nanoparticles, the frequency was varied from 800 kHz to 6 MHz and measurements of the capture ratio were made. Figure 5.19 is a typical result, for 100 nm gold nanospheres.

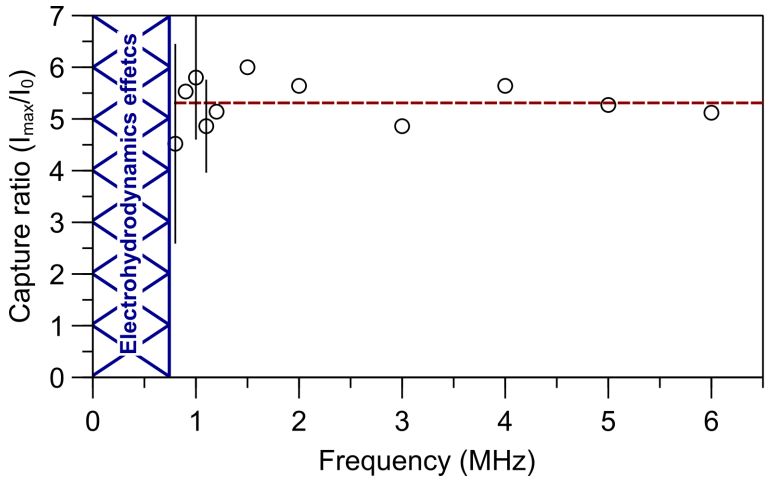

Figure. 5.19 Capture ratio at t = 4 s of Au100-LA as a function of electric field frequency applying an AC electric potential with amplitude 6 Vpp. The data points indicate the average of individual measurements with the standard deviation (95% confidence interval). The dotted line is the mean value of all measured capture ratios. Frequencies smaller than 800 kHz were not studied due to the appearance of electrohydrodynamic effects that perturb characterization.

The capture ratio does not depend on frequency. This suggests that the real part of the Clausius Mossotti is independent of frequency in this range. This is in line with observations using a different technique for slightly larger gold nanoparticles, and also with predictions by Gierhart et al. The bulk conductivity of the gold nanoparticle core is so high (4.1×10^7 S m^{-1}), completely dominating the dielectric response, leading to $\mathrm{Re}(\tilde{f}_{CM}) = 1$ for all frequencies studied. The CMF for gold nanoparticles is expected to be unity for frequencies well beyond 1 GHz, as a result of their conductive core. On the basis of this finding, we decided to keep the working frequency fixed at 1 MHz.

5.5.4 Gold nanoparticles response

We now discuss the results of the quantitative measurement of the DEP capture ratios for 80 nm, 100 nm and 150 nm diameter gold nanospheres as a function of the amplitude of the AC electric potential applied to the electrodes. These measurements were carried out using a fixed frequency of 1 MHz. Experimental settings were kept constant for

all particle diameters and amplitudes: temperature (298 K), solution conductivity (10^{-2} S m^{-1}), electric field switching sequence (3 s "ON", 5 s "OFF"), camera frame rate (50 fps) and device geometry (electrode separation 20 μm, channel height 20 μm). As described above, videomicroscopic sequences were recorded for each data point, processed, and the corresponding capture ratio was determined.

The resulting set of experimental capture ratios as a function of the nanoparticle diameter and electric field amplitude is shown in Figure 5.20. The capture ratios rise quadratically with the amplitude of the applied AC potential. We choose to stay at sufficiently low amplitudes to ensure this quadratic behaviour, as well as avoiding unnecessary deterioration of the ITO electrodes and undesired electrohydrodynamic effects such as electro-thermal motions or electro-osmosis.

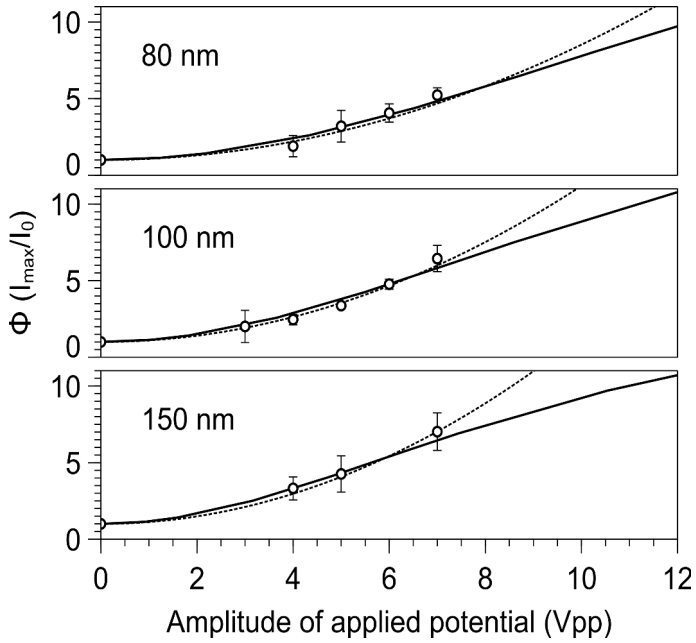

Figure. 5.20 Experimental DEP capture ratios (black circles) for gold nanoparticles in aqueous solution as a function of the amplitude of the AC potential applied to the electrodes, quadratic models fits to the experimental data (dotted lines) and capture ratios from numerical modelling realised in sections 5.5.5 (solid lines) and 5.5.6. Each experimental point corresponds to at least three measurements in different devices (f = 1 MHz).

The main experimental observations on the dielectrophoresis of sub-200 nm gold nanoparticles in our microfluidic architecture can be summarized in three points. First, the dielectrophoretic capture is concentrated in a small area at the tip of the electrodes. Second, the dielectrophoresis is independent of frequency over the frequency range studied. Third, at low field amplitudes the capture ratio depends quadratically on the electric field amplitude.

5.5.5 Simple physical model of DEP capture dynamics

We developed a simple physical model of the dielectrophoretic capture of Brownian, sub-200 nm gold nanoparticles which reproduces the experimental observations. The time-averaged DEP force experienced by a polarisable particle of arbitrary size, shape and composition in a medium of different polarisability in a divergent AC electric field is well known as in equation 5.1.

In the context of our measurement we control the frequency (radial frequency ω) and amplitude (U_0) of the electric potential applied to the electrodes.[1] Furthermore, we measure the effect of dielectrophoresis on different particle systems, while keeping the same geometry of the device. The electric field can be written $\mathbf{E} = U\mathbf{G}$, such that $\mathbf{G}$ contains the information on the topology of the field, and U is the experimentally applied amplitude. We further introduce $K_{pol} = V_p \mathrm{Re}[(\tilde{\alpha})]$. This product of the particle volume V_p and its effective polarisability could be loosely referred to as the "dielectrophoretic susceptibility of the particle. Thus, equation can be written as follows.

$$\langle \mathbf{F}_{DEP} \rangle = \frac{1}{4} K_{pol} U^2 \nabla |\mathbf{G}|^2 \tag{5.15}$$

The sub-200 nm particles that are studied in this work undergo significant Brownian motion. The steady, directional DEP force is thus perturbed by the random Brownian

force on the individual particles. At the microscopic scale, the overall behaviour of Brownian particles in a DEP field has usually been described with the Fokker-Planck (or Smoluchowski) equation.[168, 169] The Smoluchowski equation can be rewritten into a diffusion-advection equation.[170] Such a diffusion-advection description has been applied in simulations of DEP in combination pressure-driven and electro-hydrodynamic flows.[171, 172] We apply one further approximation (tentatively called the "chemist's approximation"): we replace the DEP-force related advective term by a spatially dependent capture rate. This approximation can be made since the DEP force is strongly localised very near the tip of the electrode and always pointing towards the tip of the electrode see section 5.5.1.

Far away from the electrode, the force is negligible and pure diffusion dominates. The diffusion of the nanoparticle concentration distribution is characterized by the Fickian diffusion coefficient D ($m^2\ s^{-1}$), given by Stokes-Einstein-Sutherland relation.[173–175] In the absence of a DEP force field, all particles diffuse freely and the concentration distribution of these 'free' particles $c = c(x, y, z, t)$ thus follow the simple diffusion equation.

$$\frac{\partial c}{\partial t} = D\nabla^2 c \tag{5.16}$$

A particle that comes under the influence of the DEP force and does not escape as a result of Brownian motion will end up on the tip of the electrode (as seen in the section 5.1.4). The probability that the capture eventually happens is proportional to the magnitude of the DEP force. On the ensemble level (the average of the contributions of individual particles) this probability can be represented with a capture rate, which we call k_{cap}. Within the DEP "capture zone", the evolution of free particles is described by a diffusion-reaction equation

$$\frac{\partial c}{\partial t} = D\nabla^2 c - k_{cap} c \tag{5.17}$$

The spatially-dependent capture rate is assumed to be proportional to the (effective) magnitude of the dielectrophoretic force, which enables us to write:

$$k_{cap} = \kappa K_{pol} U^2 \tag{5.18}$$

K_{pol} is the term describing the polarisability of the particle in its medium. κ is a proportionality factor that links k_{cap} to the topology of the DEP force field. It translates the probability of a particle at a certain position in the DEP force field ending up captured when continuing its motion under the influence of the DEP force and the random Brownian force. This factor, κ, is constant throughout this work, since we always use devices with the same electrode configuration. This enables relative measurements of K_{pol}. For a spherical particle of radius a having a complex permittivity ($\tilde{\varepsilon}_p$) in a medium $\tilde{\varepsilon}_m$ (assuming an infinitely thin frontier between particle and medium), the following equation has been derived.

$$K_{pol} = 4\pi\varepsilon_m a^3 \mathrm{Re}\left[\tilde{\mathrm{f}_{\mathrm{CM}}}\right] \quad \text{with} \quad \tilde{\mathrm{f}}_{\mathrm{CM}} = \frac{\tilde{\varepsilon}_{\mathrm{p}} - \tilde{\varepsilon}_{\mathrm{m}}}{\tilde{\varepsilon}_{\mathrm{p}} + 2\tilde{\varepsilon}_{\mathrm{m}}} \tag{5.19}$$

This equation features the Clausius-Mossotti factor $\tilde{f}_{CM}$ that was mentioned earlier, and whose behaviour for polystyrene and gold nanoparticles was discussed in more detail in section 5.4.2 . κ is a proportionality factor that links k_{cap} to the itinerary of the particle in the DEP force field. It only depends on the topology of the electric field, and is therefore constant throughout this work, since we use always devices with the same electrode configuration. The topology of the field gradient is furthermore represented in an approximate manner by the spatial distribution of k_{cap}. In our model, this probability is taken to be zero outside of the zone where the DEP force is significant

and has a constant value inside. This means that when a particle enters this "DEP zone" there is a certain probability that it is captured (but it also has a probability to escape the zone thanks to Brownian motion). The “DEP zone” is modelled to be a constant value within a hemisphere of radius R_{cap} centred around the electrode tip. (Figure 5.21). When the DEP field is switched off, k_{cap} is set to zero everywhere, and all capture particles are assumed to be concentrated in a thin disk. Finite-element calculations of the electric field in our device architecture (section 5.5.1) showed that the DEP force only has significant magnitude very close to the electrodes. The DEP force is always directed towards the tip of the electrode. This is in agreement with the observation that DEP capture only takes place in a small circular area near the tips of the electrodes.

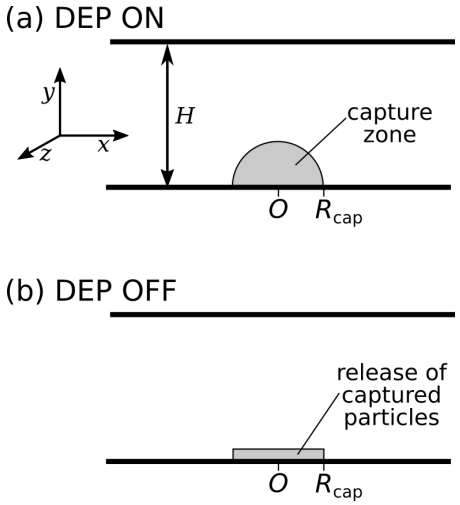

Figure. 5.21 Schematic of the geometry of the system used in numerical modelling (cross-section in the xy plane at z = 0). (a) Hemisphere where the particles have a non-zero probability of being capture during the “DEP ON” phase. (b) Initial condition for the free diffusion upon entering the “DEP OFF” phase.

5.5.6 Numerical modeling

Our reaction-diffusion model of dielectrophoresis of Brownian particles was solved numerically for the geometry and boundary conditions corresponding to our electro-

microfluidic device. The solution describes the ensemble behaviour in terms of the spatial and temporal distribution of the particle concentration (number density), *i.e.* the collective average result of the motions of individual particles. In Figure 5.22 the evolution of the radial nanoparticle concentration profile around the tip of the electrode is shown for a 2 μm thin layer above the substrate, for a given k_{cap} and D. During the "DEP capture" phase, particle density builds up in the area at the tip of the electrode. Simultaneously, there is some depletion of nanoparticles just outside this capture area, due to mass transfer limitation, i.e. diffusion of particles is too slow to replenish the particles that have been dielectrophoretically captured at the electrode tips.

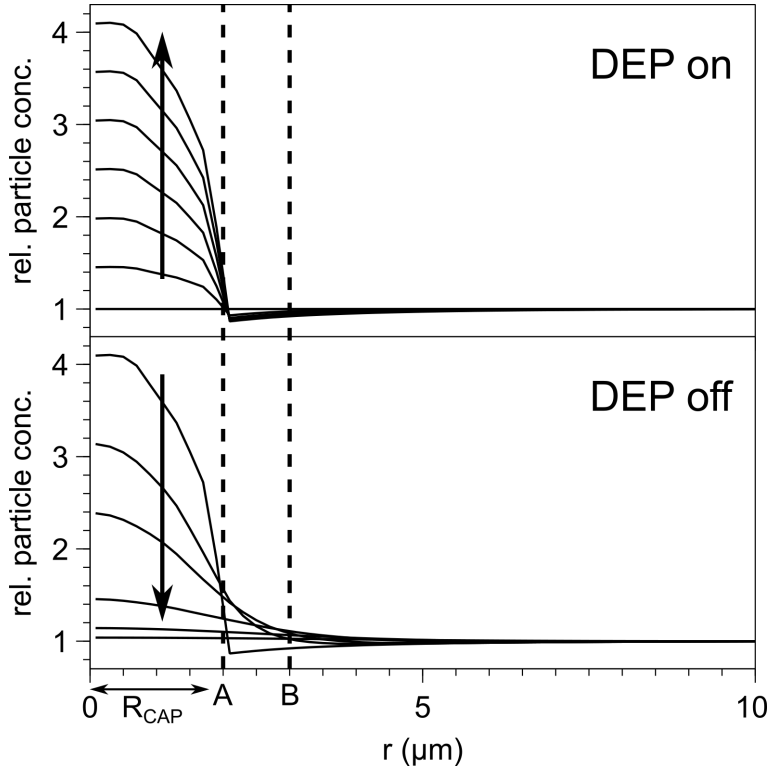

Figure. 5.22 Example of a numerical result of the time-evolution of the relative nanoparticle concentration near the tip of the electrode: radial concentration profiles relative to the centre of the capture zone. The labels "A" and "B" indicate the limits of the inner capture zone and the outer "depletion disk", respectively (corresponding to $R_{capture}$ and $R_{depletion}$ in Figure 5.5). (*top*) capture of particles by positive dielectrophoresis. (*bottom*) free diffusion of particles after release of the DEP field. Model parameters: 100 nm nanoparticles, water at 298 K, capture radius 2 μm, capture rate 0.8 s^{-1}. Right: Scale representation of the system with “A” and “B” circles.

When integrating the particle concentration in the inner capture area, and the particle concentration in the ring just around this area, we obtain the evolution of the integrated intensity of these two areas over time, which can be directly compared with experimental capture curves. As can be seen in Figure 5.23, there is close agreement between experimentally obtained DEP capture curves and model curves. Also, the depletion next to the capture zone is reproduced.

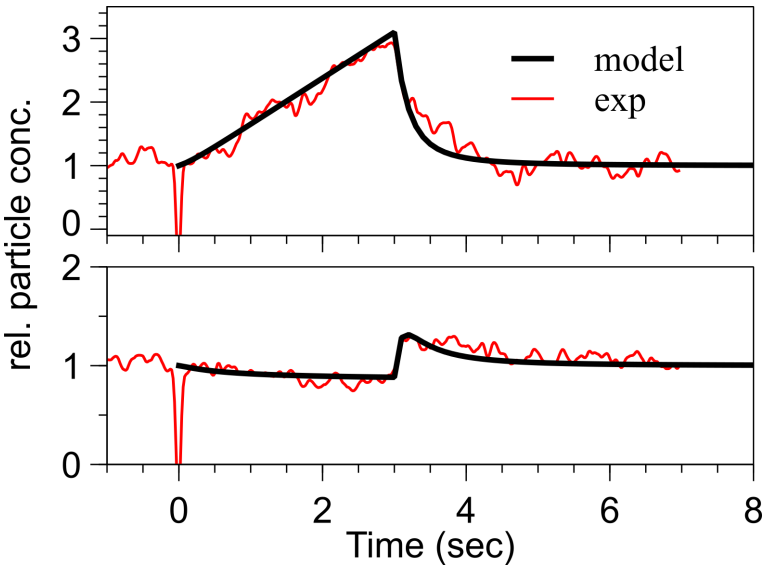

Figure. 5.23 Time evolution of the particle concentration. Comparison of model (black) and experimental capture curves (red). Capture of 100 nm gold nanoparticles in water at 298 K on the tip of electrode (*top*) and depletion in a ring just outside the capture zone (*bottom*). Experiment: amplitude 5 Vpp, theory: capture rate 0.8 s^{-1}.

A series of numerical simulations was carried out using our model, varying k_{cap} for each nanoparticle diameter. As simulation parameters, we used the 3 s "DEP ON"/5 s "DEP OFF" cycle from the experiment. For each of the three particle diameters, the corresponding diffusion coefficient was set, and then the capture ratios were evaluated for different values of k_{cap} . This yielded the evolution of the capture ratio as a function of k_{cap}, for each nanoparticle diameter studied.

For direct comparison with experiments, k_{cap} was converted to an applied electric potential amplitude using Equation 5.18, so that we can plot the capture ratio as a

function of applied potential amplitude. The conversion is done by choosing a value for the factor κK_{pol} that gives the best fit between experiment and model for a given nanoparticle diameter (Figure 5.20). For each nanoparticle diameter studied, a different value for κK_{pol} was obtained. There is agreement between the experimentally measured capture ratios and those obtained from our model (Figure 5.23). The numerically modelled capture ratios have a quadratic behaviour as a function of electric potential amplitude at low amplitudes. These level off at higher amplitudes as a result of nanoparticle depletion near the electrodes due to mass transport limitation. This depletion effect is more pronounced for larger particles. The experimental observations were done at sufficiently low amplitudes to still be in the non-depleted quadratic regime, where the Brownian motion is sufficiently potent to supply new particles to be captured. This enabled the accumulation of measurable amounts of particles. In order to fit the numerically modelled capture ratios to the experimental data, the k_{cap} of the model is related to the amplitude of the applied potential U. This determines κK_{pol}. The coefficient κ only depends on the electric field topology and is independent of the nanoparticles. We may thus determine relative values of K_{pol} for nanoparticles, by dividing the κK_{pol} by a reference value. Here, we take the 100 nm particles as the reference value. Figure 5.24 displays the evolution of K_{pol}, a measure of the susceptibility of the nanoparticles to dielectrophoresis as a function of gold nanoparticle diameter.

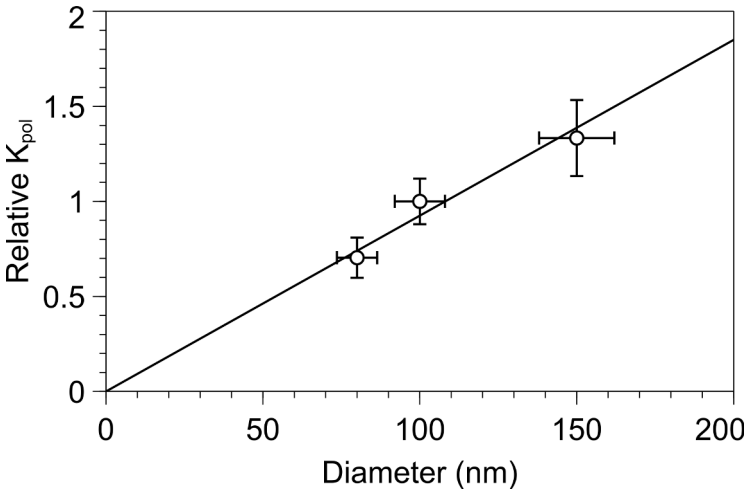

Figure. 5.24 Relative dielectrophoretic susceptibility K_{pol} as a function of gold nanoparticle diameter (circles). The K_{pol} values are relative to the value of 100 nm particles. The solid line suggests a linear relation between K_{pol} and nanoparticle diameter.

For sufficiently large spheres K_{pol} is expected to depend on the volume (see Equation 5.19), *i.e.*K_{pol} will vary as diameter cubed. This is clearly not the case here; the dependence seems to be linear. We speculate that in the size range 200 nm to 1 μm the dependence of K_{pol} on diameter evolves gradually from linear to cubic. The break-down of the cubic dependence for sub-200 nm particles may be explained by the derivation of Equation 5.19 for spherical particles. This states that the electric double layer around the particles is approximated as a surface conductivity at the infinitely thin particle-medium interface. This is justified for sufficiently large particles (> 1 μm), where the electric double layer ion cloud is thin compared to the particle diameter, but is expected to break down for smaller particles. The linear dependence of K_{pol} on diameter means that K_{pol} falls off less radically for submicron nanoparticles than expected on the basis of the usual model of the dielectrophoretic force for spheres. There are therefore two reasons why very small objects (nanoparticles, proteins, polymers) can still be captured in dielectrophoretic processes: (1) Brownian motion bringing the

objects close to the zone of effective capture and (2) breakdown of the cubic dependence of the dielectrophoretic force for small particles.

More precisely, we designate $u = u(x, y, z, t)$, the local concentration of free nanoparticles and $v = v(x, y, z, t)$, the local concentration of particles that have been captured by DEP. The free nanoparticles diffuse with a constant isotropic Fickian diffusion coefficient D. The process of nanoparticles being trapped onto the small area at the tip of the electrodes is represented as a reaction transforming free particles into captured ones, characterized by rate constant= $k(x, y, z, t)$.

$$\begin{cases} \frac{\partial u}{\partial t} = D\nabla^2 u - ku \\ \frac{\partial v}{\partial t} = +ku \end{cases} \tag{5.20}$$

The system is considered to be infinite in the x and z directions, and of limited height h in the y direction. In the numerical method this is approximated by choosing a domain of width l sufficiently large for x and z and Dirichlet boundary conditions (*i.e.*, the values at these boundaries are kept constant at a particular value, providing a constant-concentration reservoir in the x and z directions). Numerical tests demonstrated L = 12 μm to be a reliable choice for our system

$$\begin{aligned} &x, z \in [-L/2, L/2] \\ &u = c_{eq}, \quad \text{at} \quad x = -L/2, x = L/2, z = -L/2, z = L/2 \end{aligned} \tag{5.21}$$

In the y direction the particle flux is set to zero at the bottom and top of the microchannel (Neumann "zero-flux" boundary condition). In our case, we have h = 20 μm

$$\begin{aligned} &y \in [0, h] \\ &\tfrac{\delta u}{\delta y} = 0, \quad \text{at} \quad y = 0, y = h \end{aligned} \tag{5.22}$$

In our model, we start with an initial condition at $t = 0$ where the system is at equilibrium, i.e. the concentration of free particles is the same throughout the sample, and no particles have been captured. The value of C_{eq} is arbitrary, since our experiment gives the relative concentration, and a convenient choice is $C_{eq} = 1$.

$$\begin{aligned} u(x, y, z, t = 0) &= C_{eq} \\ v(x, y, z, t = 0 &= 0 \end{aligned} \tag{5.23}$$

The variable v keeps track of how many particles have been captured during the phase where the DEP field is active. The process of a particle coming under the influence of the DEP force and ultimately being captured at the electrode (in spite of its Brownian motion) is modelled using the approximation that k has a constant value within a radius R_{cap} and is zero everywhere else. This reflects the notion that the DEP force is only significant very close to the electrode tip and does not influence the motion of the particles farther away. Switching the DEP field on and off is reflected by the temporal dependence of k. The DEP field is on between $t = 0$ and $t = t_{off}$, and is subsequently switched off.

$$\begin{cases} k = 0, & t > t_{off} \\ k = 0, & t \in [0, t_{off}] \wedge x^2 + y^2 + z^2 > R_{cap}^2 \\ k = k_{cap}, & t \in [0, t_{off}] \wedge x^2 + y^2 + z^2 \leq R_{cap}^2 \end{cases} \tag{5.24}$$

Simultaneously, at $t = t_{off}$ all captured particles are released as a thin flat disk with radius R_{cap} and a minimal height h, which we chose to be the height of a single elemental volume in our solver. We numerically achieved this transfer from "captured" to "free" particles by summing all xz planes of v over all y and adding this sum plane to the bottom plane of u. Subsequently all elements of v are set to 0. In essence, we sequentially solve two partial differential equation systems, the first representing the DEP capture phase in a diffusion-reaction system, the second a pure diffusion

equation (PDE) of the released particles, using the results of the first PDE as the initial condition.

This system of partial differential equations was solved numerically by M. Werts in a regular cubic mesh in Cartesian coordinates using the finite-volume method implemented by the FiPy module[176] (version 3.1.3.dev531+gd4b7593, Anaconda 4.4.10, Python 2.7.15-condaforge, 64-bit Linux). The choice of the Cartesian coordinates and the regular mesh was guided by (i) limitations in the code concerning the use of cylindrical coordinates, and (ii) facilitation of post-processing of the solution on a regular mesh, in spite of the higher computational cost. The computational cost was somewhat alleviated by using symmetry and calculating only one quadrant of the solution.

5.6 Conclusion

The capture area of the dielectrophoresis delimited by a radius of 2 μm was determined to be representative of the area directly linked to the dielectrophoresis force using theory, simulation and experimental observations.

A method for the measurement of DEP of gold nanoparticles was developed and found to be in agreement with results in the literature. This offers the possibility to work with a variety of nanoparticles samples in our microfluidic work bench.

Through *in situ*, real-time observations on well-defined gold colloids using dark-field videomicroscopy in combination with physicochemical modelling, we explained why small gold nanospheres (here limited to 80 nm diameter) can still be effectively captured and assembled by dielectrophoresis in microfluidic systems. If one was to extrapolate the often-cited cubic dependence of the dielectrophoretic force on sphere radius from micrometre to sub-200 nm nanoparticles, the DEP force would be predicted to be exceedingly weak.

However, near the tips of microelectrodes, very high electric field gradients exist and Brownian motion is efficient in transporting smaller particles towards these zones where the particles are captured by DEP. The capture zones are limited to the regions very near (< 5 μm) the electrodes; the DEP force is negligible outside these zones. The DEP force on the gold nanoparticles was found not to depend on the frequency of the electric field in the 800 kHz – 5 MHz band studied. We also found that the DEP force for these sub-200 nm particles does not display a cubic dependence on particle diameter, but a linear dependence. This is likely a manifestation of the increasing influence of the electric double-layer ion cloud around the particles as the particle diameter decreases. The resulting higher electric polarizability is further enhanced by the high conductivity of the gold core.

There are few in situ studies concerning the strength of the DEP force for sub-200 nm nanoparticles. Much prior experimental work has focused on the frequency dependence, which has been very fruitful for the characterization of polystyrene latex dispersions. The present work focuses on gold nanoparticles, and the dependence of the DEP strength on applied electric potential and nanoparticle diameter, since the DEP force was found not to depend on frequency in the 800 kHz – 5 MHz band studied. The lower limit on the gold nanoparticle diameter in our experiments was 80 nm; smaller particles generated insufficient contrast in the dark-field microscope.

Chapter 6

Dielectrophoresis and spectroscopy

This chapter describes an original bright-field transmitted light method for optical extinction spectroscopy measurements on nanoparticles directly inside a microchannel cell under the application of a dielectrophoretic field. In comparison to the dark-field videomicroscopy used in the previous chapter which relies on the light scattering by gold nanoparticles, the range of particle sizes that are accessible is extended to particles smaller than 80 nm. In effect, we use the high optical extinction properties of gold nanoparticles in the UV-vis range. The technique presented offers the advantages of working with transmitted light microscopy and generates spectra whose variation can be recorded as a function of time. The design of system and its calibration are explained first. Then extinction spectra are recorded for different nanoparticle solutions while modulating the electric field. The modulation of the optical density as a result of the dielectrophoretic capture/release of gold nanoparticles is analysed in terms of the dielectrophoretic susceptibility of the nanoparticles, which allowed us to extend the measurements of Chapter 5 towards smaller particle sizes. Furthermore, we describe the enhancement of the DEP capture of nanoparticles in presence of pressure-driven flow of the suspension over the array of microelectrodes, and apply the DEP-modulated

optical extinction microscpectroscopy to the analysis of mixtures of gold nanoparticles of different diameters.

6.1 Optical detection in the microfluidic cell

The microfluidic volume in the device was observed in bright-field transmitted light contrast through the Olympus IX71 inverted microscope using a moderate magnification objective (20x, N.A. = 0.4) (Figure 6.1). The illumination was provided by the illumination optics of the microscope (halogen light source, Osram HLX 100 W). The beam-splitter in the microscope's observation path was used to send 20% of the light onto the Ximea digital camera attached to the front port and 80% to the side port, where it is focussed onto the end of an optical fibre. The optical fibre has a core diameter of 50 μm. The other end of the optical fibre was connected to a diode-array UV-visible-NIR spectrograph (OceanOptics USB4000-VIS-NIR). Spectra were recorded using 250 milliseconds exposure time. The useful spectral range of the present set-up was 430 . . . 700 nm, limited at short wavelengths by the weak blue-UV emission of the halogen lamp, and at long wavelengths by the infrared filter firmly integrated into the microscope illumination optics.

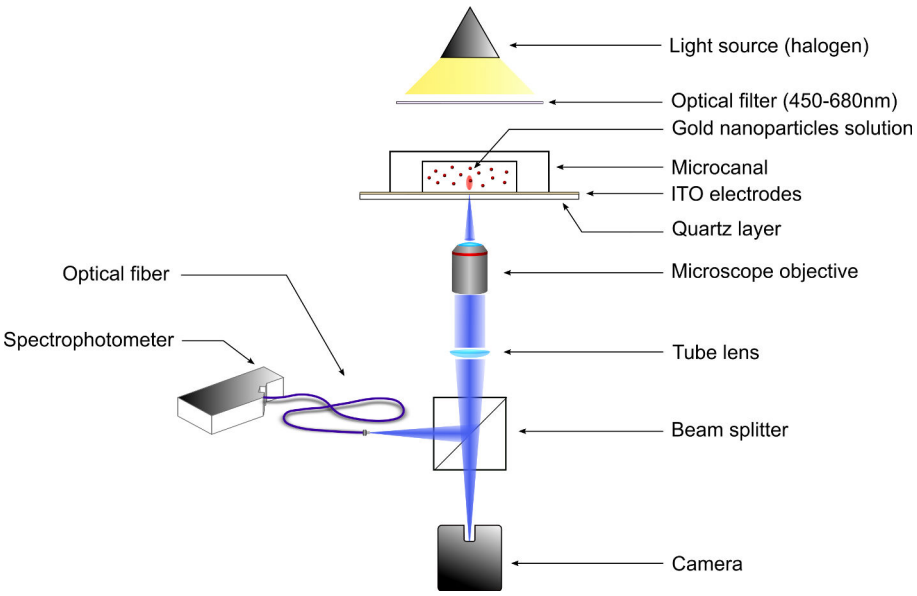

Figure. 6.1 Schematic of the dielectrophoresis system composed of ITO electrodes, PDMS microchannel and halogen light source, and split detection channel consisting of digital camera and fibre-coupled spectrometer.

The entry of the fibre was adjusted to be in focus and at the center of the image plane. To do this, a high power LED was coupled to the fibre instead of the spectrophotometer. This allows us to position the fibre by optimising the image on the camera sensor of the LED light back-scattered from the sample.

6.1.1 Experimental characterization of the effective observation area

The optical path has been kept as simple as possible in these experiments, essentially placing a fibre-coupled spectrometer at the side-port of the microscope. The transmitted-light illumination was not optimised. It is therefore expected that the part of the microscope image that is sampled by the spectrometer is relatively large. We decided to determine the sampled area experimentally by scanning the entire microsystem and recording the evolution of the detected light intensity. The microsystem provides sharp,

small features: the microfluidic channel walls, and also the transparent microelectrodes that have sufficient contrast.

A scan along the width of the microchannel was realised using the motorized sample stage. The evolution of the detected optical spectrum was recorded as a function of the position (see Figure 6.2 a)). The walls of the microchannel were used as markers providing a spatial 'delta' pulse. From the microscope camera image a line profile (one pixel wide) was plotted to identify the position of the walls in the image.

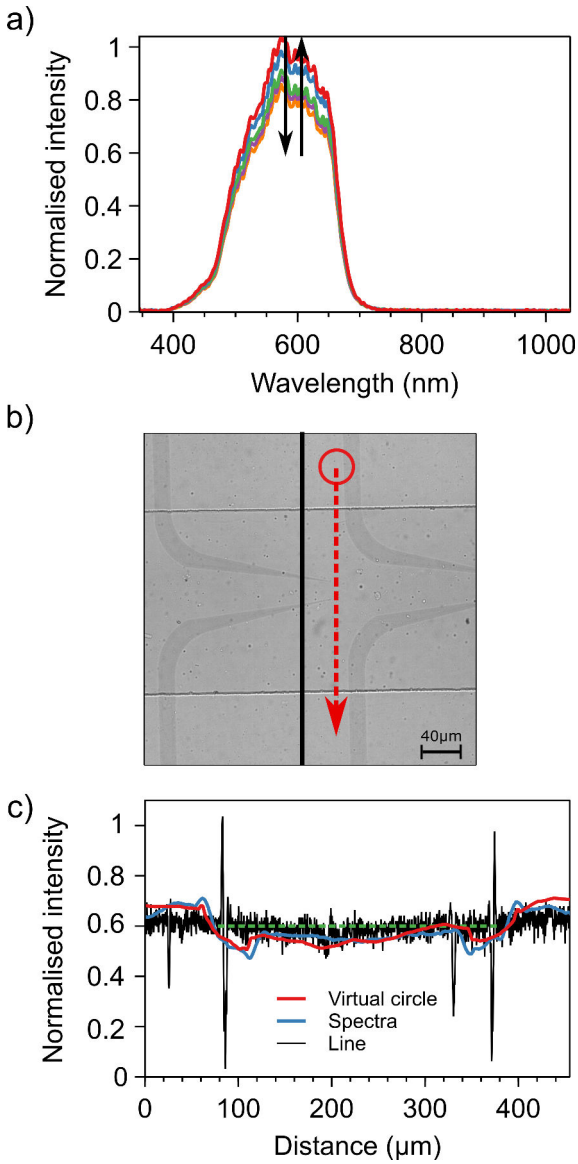

Figure. 6.2 a) Spectra evolution sweeping the microchannel as a function of the position. b) Bright field image of the microchannel, black line corresponds to the line where the black profile was extracted, red circle shows the area swept along the dotted red line. c) Normalised intensity as a function of the distance from real experimental observation (blue), virtual sweeping with a circle diameter of 51 μm (red) and from a pixels line (black). A distance of 300 μm was added corresponding to the walls distance of the microchannel.

Two intensity-*vs*-position profiles were generated. One profile is the real profile of the detected spectral intensity. The second is a virtual profile generated by numerically scanning a circular region-of-interest over the microscope camera image and tracing

the integrated intensity in this ROI as a function of position. The diameter of this circular ROI is tuned such that the virtual profile (red profile) has the same shape as the experimental profile (blue profile) (see Figure 6.2)

From the comparison of the two profiles, the size of the area sampled by the spectrophotometer was determined. A diameter of 51 μm was found. The recorded spectra are thus averages over the microfluidic volume covered by this area. No further optimization of the spatial resolution of optical system for extinction measurement[177] was done at this stage, since the main interest was in observing and characterizing the dielectrophoretic modulation, which requires an average over a relatively large area of the microfluidic channel.

6.1.2 Extinction microspectroscopy

Colloidal gold nanospheres 40, 80 and 100 were stabilised with lipoic acid as described before, and will be referred to as Au40-LA, Au80-LA and Au100-LA, respectively. This time, ten millilitres of each solution were centrifuged in order to concentrate the particles twenty-five times. The particles were finally dispersed in a total volume of 500 μL aqueous solution (0.2 mM NaLA, 1 mM NaOH). The samples were characterized using optical extinction (UV-visible) spectroscopy, confirming their integrity and providing reference spectra for the extinction spectroscopy in the microfluidic system. On basis of the extinction spectra, the concentrations of nanoparticles in the stock solutions were determined[2] to be 1.93 x 10^{12} particles mL^{-1} for Au40, 2.32 x 10^{11} particles mL^{-1} for Au80 and 8.95 x 10^{10} particles mL^{-1} for Au100.

Optical extinction spectroscopy was done by first recording the dark spectrum I_{dark}, *i.e.* the spectrum recorded by the spectrometer without any light. Subsequently, a baseline spectrum I_0 was recorded by filling the microfluidic channel with water. With these spectra in place, the extinction spectrum OD was obtained from the

light transmitted through a solution containing nanoparticles. Optical spectroscopy measurements were carried out at ambient temperature on aqueous gold nanoparticle dispersions contained directly into the microfluidic channel.

$$\mathrm{OD} =^{10} \log\left(\frac{I - I_{\mathrm{dark}}}{I_0 - I_{\mathrm{dark}}}\right) \tag{6.1}$$

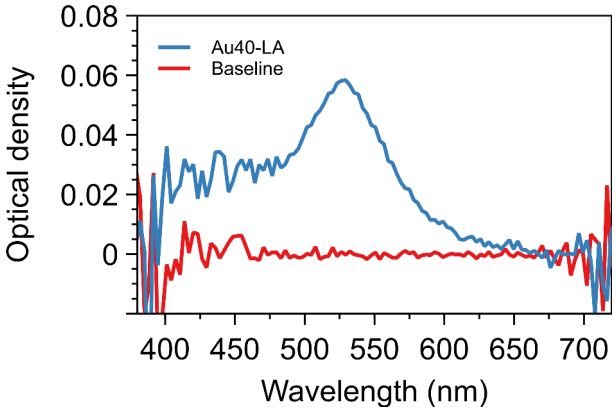

Figure. 6.3 (*top*) Baseline spectrum obtained using water injected in the microchannel (*bottom*) Extinction particles spectrum recorded of Au40-LA solution injected into the microchannel.

Extinction spectra of the solvent baseline and of the aqueous solution containing Au40-LA are shown in Figure 6.3. The baseline fluctuations were sufficiently small over several minutes in order to reliably measure spectra of the solution in the microfluidic volume. The spectrum of the nanoparticle dispersion shows the typical plasmon resonance for gold nanoparticles. The optical density corresponds well to the density expected for the 20 μm path length ($\mathrm{OD}_{1\mathrm{cm}} = 25$, expected for 20 μm: 0.05, found: $\mathrm{OD}_{20\mu\mathrm{m}} = 0.058$)

6.2 DEP-modulated extinction microspectroscopy

The optical microspectroscopy was then combined with the application of dielectrophoresis. This is illustrated in Figure 6.4. The microfluidic device used was the same as the one of the Chapter 5. The microfluidic channel was filled with aqueous solutions containing colloidal nanoparticles. Experiments were done either with or without microfluidic flow. A periodic dielectrophoretic perturbation was applied, switching ON and OFF the dielectrophoretic field while continuously recording optical extinction spectra of the microscopic volume using the spectrometer. In a typical experiment, one cycle period was composed of 15 seconds of dielectrophoretic capture ("DEP ON") to let enough time for a sufficient number of particles to be captured. This was followed by 10 seconds of release ("DEP OFF") during which the nanoparticles diffuse freely.

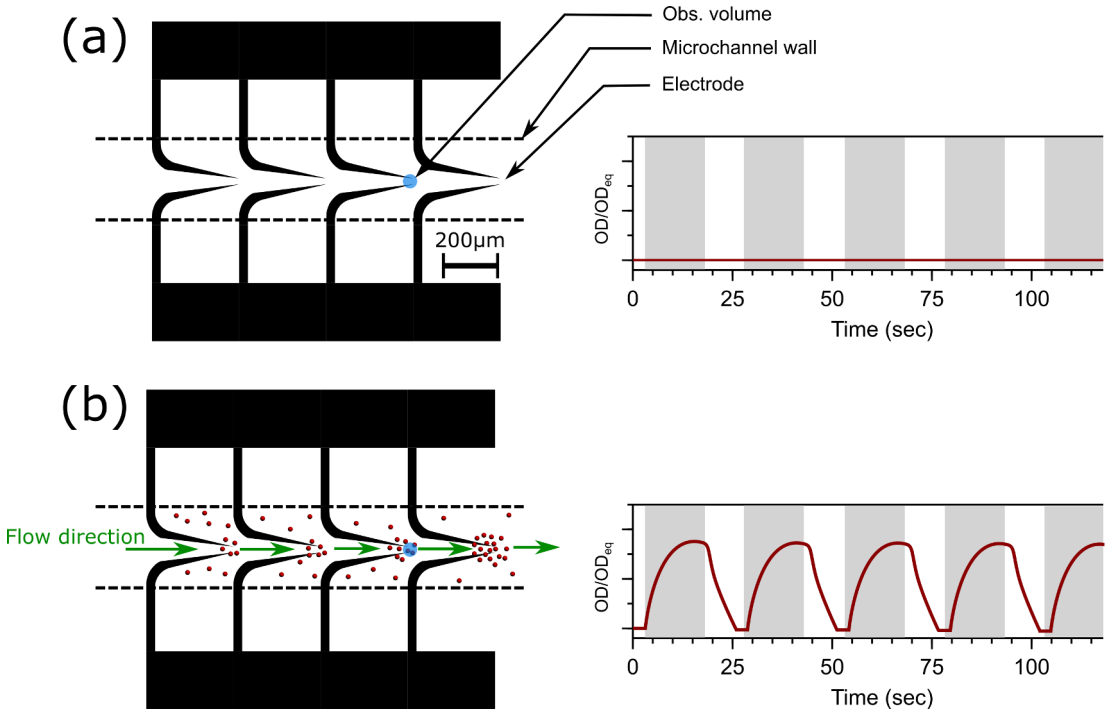

Figure. 6.4 (a): Schematic top-view of the microfluidic channel showing the relative sizes of electrodes and the capture area (actual diameter = 50 μm) analysed by the spectrophotometer. (b): Shows the gradually capture of particles along the microchannel. Dashed lines corresponds to microchannel walls.

6.2.1 DEP-modulation in the absence of flow

First, the "pure" dielectrophoresis (*i.e.*, without pressure-driven flow and undesirable electrohydrodynamic effects) for particles Au40-LA, Au80-LA and Au100-LA was studied. Electrohydrodynamic phenomena were avoided by using a suitable AC electric field at a frequency of 1 MHz, as discussed in Chapter 5.[100] The amplitude of the applied electric potential was 20 Vpp. After injection of the solution containing the nanoparticles and stopping the microfluidic flow using the pressure controller (Fluigent), the dielectrophoretic modulation was started. Once a steady modulation of the optical spectra was reached, extinction spectra were recorded for around 8 minutes. Figure 6.5 shows a typical result for Au40-LA nanoparticles.

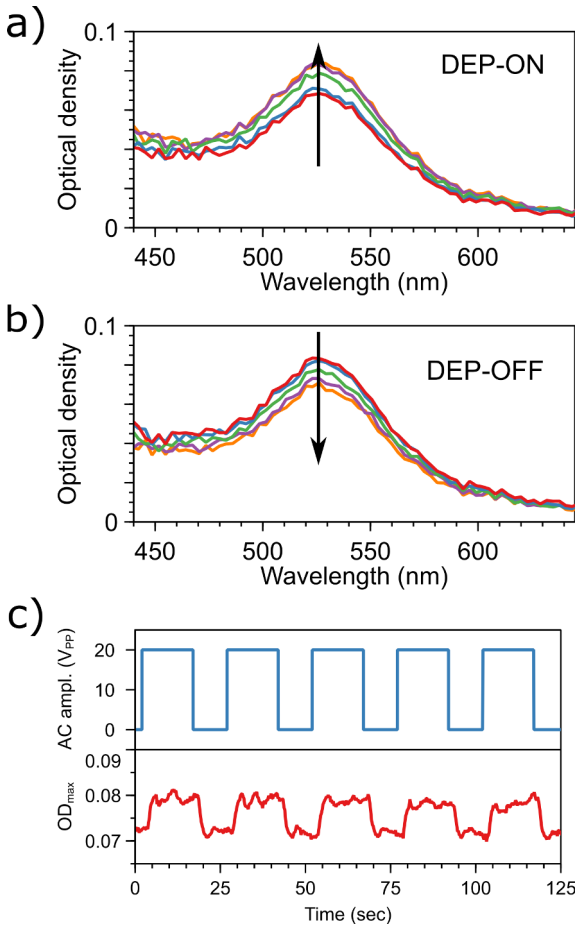

Figure. 6.5 DEP-modulated optical extinction spectroscopy of Au40-LA in aqueous solution. (a) Evolution of the extinction spectrum in the observation volume during the "DEP ON" phase. (b) Evolution of the extinction spectrum in the observation volume during the "DEP OFF" phase. (c) Amplitude of the applied AC potential (*top*) and evolution of the measured optical density at $\lambda_{max} = 526$ nm as a function of time.

The intensity of the extinction band corresponding to the Au40-LA plasmon resonance was modulated as the DEP field was switched on and off. The optical density increased as the field was switched on, indicating an increase of the number of particles in the observation volume. When the DEP field was switched off the extinction dropped rapidly to its equilibrium value. This drop corresponds to the rapid free diffusion after release of the nanoparticles from the electrode tips.

Measurement of DEP-modulated extinction spectra was performed for 40, 80 and 100 nm gold nanoparticles (Au40-LA, Au80-LA, Au100-LA) using identical experimental

settings. The periodically DEP-modulated spectra were recorded for a prolonged period (8 min). Multiple recordings were realised (more than three). Figure 6.6 contains the variations of the optical density at the wavelength of maximum extinction for the gold nanoparticles by the absence of microfluidic flow. In order to directly compare the results for the different nanoparticle dispersions, the optical densities were scaled with respect to the equilibrium optical density OD_{eq}.

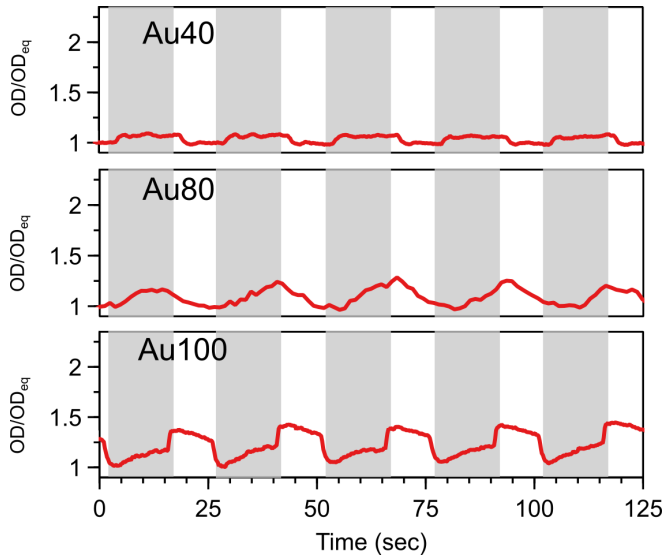

Figure. 6.6 Selected DEP modulation cycles of Au40-LA, Au80-LA and Au100-LA, in the absence of flow, monitored as the optical density at the wavelengths of the plasmon maximum, $\lambda_{max} = 526$ nm , $\lambda_{max} = 549$ nm, $\lambda_{max} = 572$ nm. The grey areas in the background indicate when the DEP field was active.

The modulated optical densities are analysed in terms of the factor by which the optical density increases as a result of dielectrophoretic concentration of nanoparticles. We call this factor the *capture factor* ψ_{cap}. It is closely related to the capture ratio ϕ_{cap} used in Chapter 5. Indeed, $\psi_{cap} = \phi_{cap} - 1$. The capture factor ψ_{cap} is 0 if no capture takes place, and becomes greater the more particles are captured during the "DEP on" phase.

The capture factor is obtained in this case from the peak-to-valley amplitude of the modulation of the optical density ($OD_{max} - OD_{min}$) and its equilibrium value (OD_{eq}).

$$\psi_{\text{cap}} = \frac{\text{OD}_{\text{max}} - \text{OD}_{\text{min}}}{\text{OD}_{\text{eq}}} \tag{6.2}$$

The optical densities were taken at the wavelengths where the nanoparticles' plasmonic extinction bands have their maximum (λ_{max}). For a single measurement, capture factors ψ_{cap} were averaged over several DEP cycles (typically 20 cycles per measurement). The results are collected in Table 6.1. The capture factor increases as the nanoparticle diameter increases, indicating that larger particles are more susceptible to dielectrophoresis.

	λ_{max}(nm)	ψ_{cap}
Au40-LA	526	0.20($\pm$0.11)
Au80-LA	549	0.35($\pm$0.13)
Au100-LA	572	0.44($\pm$0.15)

Table 6.1 Wavelength of the extinction maximum and DEP capture factor ψ_{cap} (95% confidence interval) obtained for gold nanoparticles of different diameters in aqueous solution using DEP-modulated optical extinction spectroscopy. Applied AC electric field had an amplitude of 20 V_{pp} and a frequency of 1 MHz.

For nanoparticles measured using identical parameters of the applied electric field (amplitude, frequency, topology), the capture factors ψ_{cap} are proportional to the dielectrophoretic susceptibility K_{pol} of the particles. The dielectrophoretic susceptibility gives the time-averaged dielectrophoretic force $\langle \mathbf{F}_{\text{DEP}} \rangle$ for a type and diameter of particle at a given amplitude of the applied AC potential U and topology of the electric field $\mathbf{G}$ (the electric field is defined by $\mathbf{E} = U\mathbf{G}$).

$$\langle \mathbf{F}_{\text{DEP}} \rangle = \frac{1}{4} K_{\text{pol}} U^2 \nabla |\mathbf{G}|^2 \tag{6.3}$$

By taking the ratio of ψ_{cap} for two different diameters of particles, the ratio of K_{pol} for these particles is obtained. From the present set of measurement this yields a series of relative DEP susceptibilities.

In Chapter 5, the relative DEP susceptibilities for 80, 100 and 150 nm gold nanoparticles were determined using dark-field video-microscopy.[100] Smaller particles did not generate sufficient contrast in that technique. Here we obtain results for 40, 80, 100 nm gold nanoparticles with DEP-modulated extinction spectroscopy. The overlap between the two types of measurement enables us to compare, combine and extend the results (Figure 6.7).

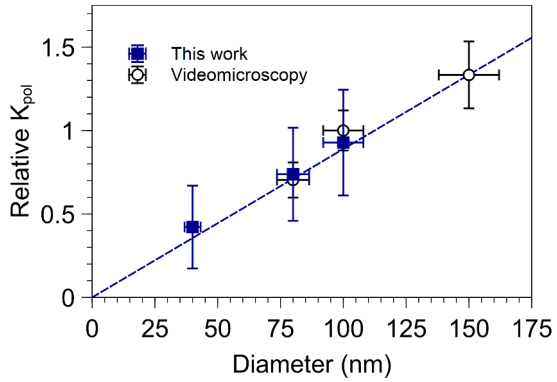

Figure. 6.7 Combined results for the relative dielectrophoretic susceptibilities K_{pol} as a function of diameter for spherical gold nanoparticles in aqueous solution (0.2mM NaLA, 1mM NaOH). Unfilled circle markers indicate the results from dark-field video-microscopy.[100] Filled squares were the result obtained using the present DEP-modulated spectroscopy. The dotted line suggests a linear dependence of dielectrophoretic susceptibility on gold nanosphere diameter. Data were plotted with their 95% confidence interval.

The new results further extend previous observations[100] that the relative dielectrophoretic susceptibility (and the DEP force for a given amplitude and frequency for the applied field) have a linear dependence on nanoparticle diameter for sub-200 nm gold particles, instead of the cubic dependence found for spheres with diameters larger than 1 μm.[165–167]

6.2.2 Enhancement of DEP modulation using microfluidic flow

It was hypothesized that the DEP capture of nanoparticles may be enhanced by having a microfluidic flow over the array of electrode pairs while periodically switching the DEP field. Particles are concentrated at the first electrode pair when DEP is switched on. When DEP is switched off, the particles are released into a 'blob' that is further transported by the flow towards the next electrode pair, where it arrives at the moment the DEP is again switched on. The advected particle 'blobs' are increasingly concentrated at each electrode pair.

To test this hypothesis, we studied this mode of DEP modulation by having a controlled slow microfluidic flow. A full experimental and theoretical study might be complex because of the combined effects of the (parabolic) flow profile and the particle diffusion. The present study only studies the flow-enhancement of DEP capture experimentally with the objective to demonstrate the relevance of the effect.

Setting the optimal flow rate

The flow rate was calculated so as to let enough time for particles to be captured at each pair of electrode tips during DEP, while ensuring that they were transported just from one electrode pair to the next during the phase that the DEP is not active. Electrode pairs are placed at distance intervals of 300 μm. In each dielectrophoresis cycle, the electric field was switched off for 10 seconds. This means that particles must be transported by the fluid at an average speed of 30 μm s^{-1}. The velocity in a microchannel is not equal along its width, the Figure 6.8 shows the velocity distribution in a microchannel. The profile of displacement can be described as a parabolic profile.[178]

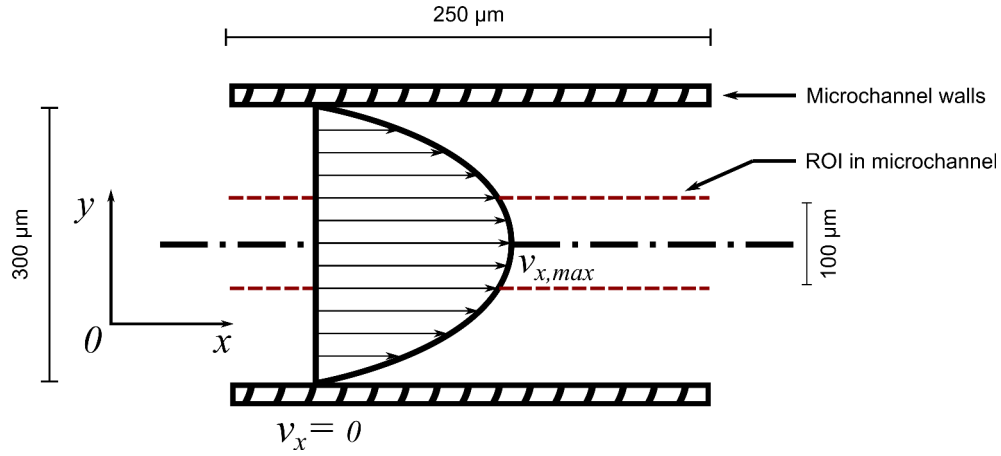

Figure. 6.8 Representation of the fluid velocity distribution in the microchannel used in this work. Red dotted lines show the region of interest (ROI) selected to analyse the average gold nanoparticles velocity in the microchannel using particles tracking analysis presented in the next part of this section.

In this case we supposed the velocity, in the ROI, equal along the width. Meaning that the velocity in the ROI is equal to $v_{x,max}$. This velocity is equal to:

$$v_{x,max} = 2 \ < v_x > \tag{6.4}$$

$< v_x >$ is the mean velocity in the microchannel. The fluidic pressure differential, required to maintain the mean velocity, was calculated to be $\Delta P = 1.15$ mbar and therefore $\Delta P = 0.58$ mbar for the equivalent velocity in the ROI for our microchannel geometry.[179]

The flow velocity was checked using dark-field single particle tracking measurements. To do this, Au150-LA (high light scattering cross section enabling single particle tracking) were injected into the microchannel. A pressure differential between channel entrance and exit was applied using a Fluigent system (0 to 69 mbar). Videomicroscopy was used because the targeted flow rate was very low and videomicroscopy offers the possibility to use particle tracking. Videomicroscopy was recorded with an exposure time of 50 ms for more than 2 minutes after stabilization of the flow. The trajectories

of particles were determined and analysed using the Trackpy package (Python). An example is shown in Figure 6.9

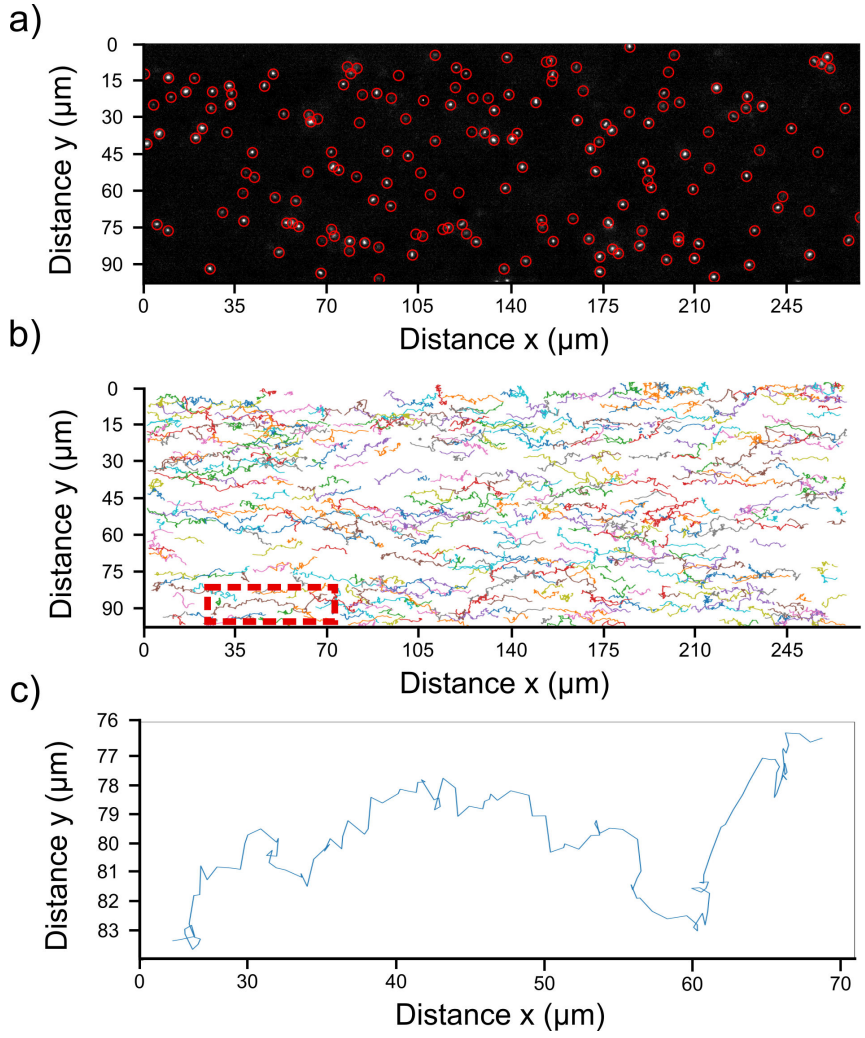

Figure. 6.9 a) Image at t=0 s of Au150-LA particles in dark-field contrast. Red circles highlight particles detected using the Trackpy. b) Trajectories of all particles detected during 2 min 30 seconds having a sufficient long trajectories in the focal plane. A fluidic pressure differential $\Delta P = 2.35$ mbar was applied. Red dotted box was the trajectory shown in the last part of the figure. c) Trajectory of the red dotted box into b) showing the perturbation of the flow on the particle Brownian motion.

Finally, by analysis of the x velocity of the nanoparticles, it was found that in the experimental set up, a differential pressure $\Delta P = 2.35$ mbar should be applied to have a mean flow velocity $v_{x,max}$ of 30.2 ± 1.54 μm s^{-1} (95% confidence interval). The

higher differential pressure necessary could be explained by possible leakages from the connections of the microfluidic system. Or also from the precision of the Fluigent at very low differential pressure.

DEP capture with flow rate

Figure 6.10 shows that microfluidic flow indeed enhances the overall yield of dielectrophoretic capture. Compared to DEP without flow, microfluidic flow was found to enhance the capture ratio by factors 1.1, 2.3 and 2.6, for 40, 80 and 100 nm diameter gold nanoparticles, respectively.

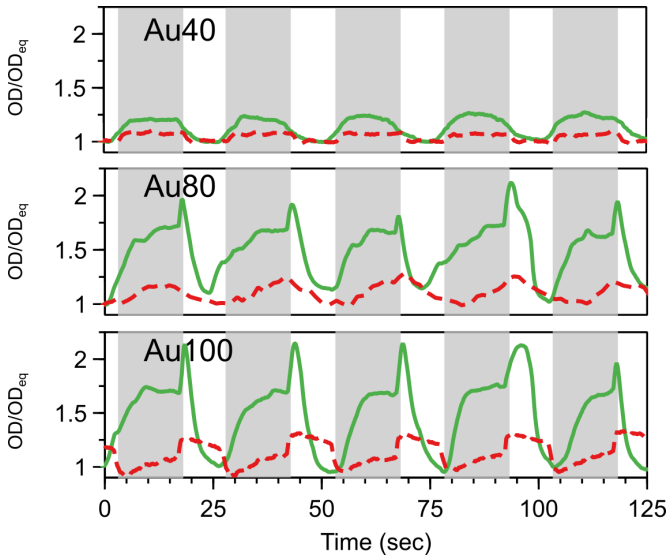

Figure. 6.10 Selected DEP modulation cycles of Au40-LA, Au80-LA and Au100-LA with flow (average speed 30 μm s^{-1}). The optical density was recorded at the wavelength of the maximum of the plasmon band: λ_{max} = 526 nm , λ_{max} = 549 nm, λ_{max} = 572 nm, respectively. The grey areas in the background indicate when the DEP field was switched on. Red dotted lines corresponds to measurements done without flow.

The higher enhancement observed for larger particle diameter can be attributed to the slower diffusion of the particles during the "DEP OFF" cycle, leading to less spreading out of the concentrated particle flocks as they are transported towards the next electrode pair. The enhancement factor is expected to depend simultaneously on

electrode pair separation, flow velocity profile (which depended in turn on flow rate and channel geometry), and nanoparticle diffusion coefficient. Furthermore, the exact position of the observation volume relative to the capture zone will also be of influence.

6.3 Multi-component analysis of a nanoparticle mixture

In this last part of the Chapter, the feasibility of analysing a two-component mixture was demonstrated using DEP-modulated extinction microspectroscopy. An aqueous solution containing a mixture of Au40-LA and Au80-LA particles was used for this. The concentration of each component was chosen such that both components contribute equally to the total optical density (Figure 6.11).

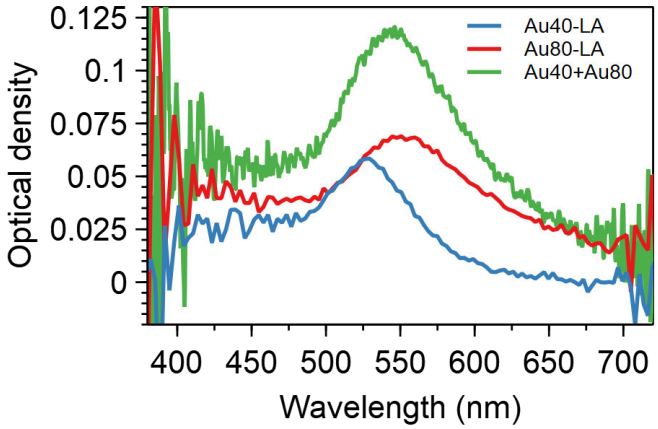

Figure. 6.11 Spectra of stock solutions Au40-LA, Au80-LA and Au40-Au80 recorded inside the microchannel for an exposure time of 250 ms.

As before, an AC electric field of 1 MHz, 20 Vpp was applied to the electrodes, with the field being active for 15 seconds ('ON') and inactive for 10 seconds ('OFF'). Microfluidic flow was induced inside the microchannel using the pressure controller in

order to enhance the capture of particles at each subsequent pair of electrodes applying a flow speed of 30μm s^{-1}. (see Section 6.2.2)

Spectra were recorded with the spectrophotometer using an exposure time of 250 milliseconds. The position of the observation volume was slightly shifted compared to the other measurements in an effort to enhance the contrast between the DEP-modulated spectra of the 40 nm and the 80 nm nanoparticles. The modulated spectra as a function of time are stored in a spectrotemporal matrix. A typical spectrotemporal matrix is shown at the top of Figure 6.12.

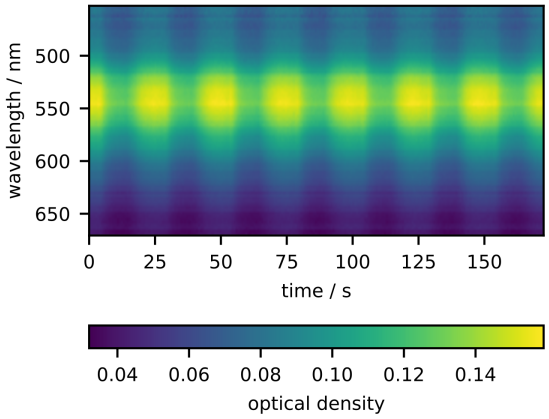

Figure. 6.12 DEP-modulated extinction spectra of an aqueous dispersion of a mixture Au40-LA and Au80-LA (spectrotemporal recording).

Looking at the individual spectra in the spectrotemporal matrix, it is not easy to disentangle the two components, due to their spectral similarity (Figure 6.11). It was decided to submit the spectrotemporal matrix to principal component analysis using singular value decomposition.[180]

Singular value decomposition (SVD) factorizes the spectrotemporal matrix $\mathbf{M}$ into the product of three matrices, $\mathbf{M} = \mathbf{U}\mathbf{\Sigma}\mathbf{V}^*$. The middle matrix $\mathbf{\Sigma}$ is a diagonal matrix whose diagonal elements are called the singular values. The column vectors of $\mathbf{U}$ and $\mathbf{V}$ contain the spectral and temporal data necessary to completely reproduce the initial

matrix. Interestingly, in the case of data containing contributions of a limited number of species, it is possible to truncate **U** and **V** to include only those vectors that contribute significantly to the spectrotemporal data. Figure 6.13 shows the decomposition of the spectrotemporal matrix of Figure 6.12, in particular the first ten singular values and the first three spectrotemporal components.

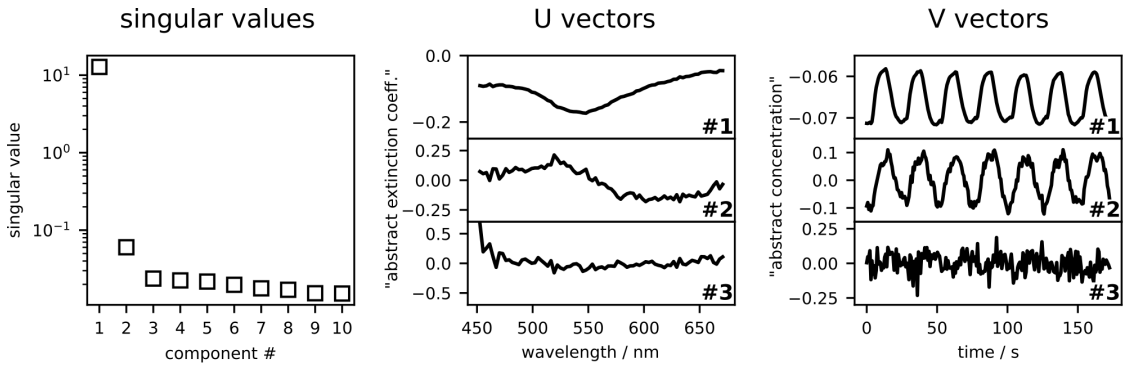

Figure. 6.13 Singular value decomposition of the spectrotemporal matrix from the DEP-modulated spectroscopic measurement on a mixture of 40 nm and 80 nm gold nanoparticles. The graphs show the singular values of the first 10 components (*left*, indicating two principal components), and the U and V vectors of the first three components. These are abstract responses and loadings, respectively. These abstract vectors are transformed into vectors with physical quantities by taking linear combinations.

The singular values of only the first two components contribute significantly. Starting from the third component we find mainly noise. What is special about this, is that SVD has identified these two components without any prior knowledge, only based on the information in the spectrotemporal matrix.

Further scrutiny of the two first column vectors of **U** and **V** shows that they contain 'warped' versions of the spectra and concentration profiles. In fact, these vectors are orthogonal, and may be converted into realistic spectra and concentration profiles by taking linear combinations. In this exploratory case, we simply optimised the linear combinations by hand to reproduce concentrations and spectral profiles (Figure 6.14).

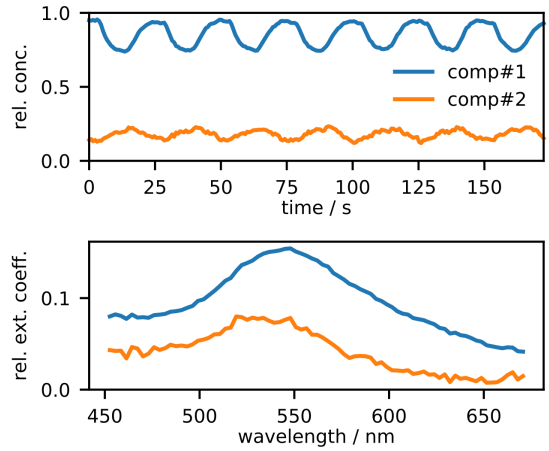

Figure. 6.14 (*Top*) relative concentration traces for the two principal components reconstructed by target transformation from the singular value decomposition of the spectrotemporal matrix. (*Bottom*) The corresponding extinction spectra. The reconstructed concentration traces and extinction spectra reproduce the recorded spectrotemporal matrix.

This result demonstrates that it is feasible to use DEP-modulated spectroscopy to disentangle multicomponent mixtures in situ. It is important to emphasize that this analysis is done on a microfluidic volume of sample and that the sample is only minimally perturbed. It is even possible to recover the sample from the system after analysis.

6.4 Conclusion

In this chapter, it was demonstrated that by coupling the electromicrofluidic system developed in this thesis, it can also be coupled to a spectrophotometer. The resulting system was used to measure particles smaller than 200 nm and to expand the range of dielectrophoresis measurements to particles smaller than 80 nm diameter.

The dielectrophoretic susceptibililties of 40 nm, 80 nm and 100 nm gold nanoparticles were measured by operating the system without microfluidic flow. These measurements

confirm the linear trend observed for the dependence of dielectrophoretic susceptibility on nanoparticle' diameter first described in Chapter 5.

Dielectrophoretic concentration of nanoparticles was enhanced by applying a fluidic flow, which transports the particles along the array of microelectrodes. Finally, it was demonstrated that multicomponent analysis of a mixture of nanoparticles could be realised *in situ* by applying a modulation to the sample using dielectrophoresis.

This initial study shows the potential of the technique, but it equally shows where the challenges lie. The waveforms obtained from the DEP-modulated spectra have different shapes, and currently we only extract the maximum and minimum values of each cycle. We anticipate that with suitable capture-diffusion-advection models we may be able to explain and analyse the waveforms in more detail. Also, the multicomponent analysis should be further extended to more complex samples, ultimately samples of unknown composition.

Chapter 7

Conclusion and prospect

Microfluidics has opened the possibility of handling liquids at small scales with a small amount of analytes. We built an electro-microfluidic system with the goal to investigate dielectrophoresis for the handling of nanoparticles. Gold nanoparticles show interesting optical properties as a result of an electromagnetic resonance known as the localised surface plasmon resonance.[2, 15, 16] Thus this has made these particles a good candidate to follow mechanisms of the assembly of particles.
Based on the prior experience of the laboratory with gold nanoparticles, it was a logical choice to use these objects as analytes.[2, 15, 24, 115, 181]

Dielectrophoresis is analogous to the related phenomenon of electrophoresis but only takes place in a non-uniform electric field. It is useful to manipulate small objects. Dielectrophoresis has previously been used with latex spheres,[17] biological cells,[182], proteins[183–187] but rarely on metallic nanoparticles.[167]

In this thesis, we first studied the interaction of bio-molecules between streptavidin and biotins using gold nanospheres with optical spectroscopy, then an electromicrofluidic was built and used to analyse the dielectrophoretic response of gold nanospheres by

videomicroscopy. This led ultimately to an experiment in which a solution composed of two sizes of particles was analysed using spectroscopy in microchannel in order to separate particles as a function of their dielectrophoretic affinities.

For each chapter the main findings have been summarised in section 7.1. An outlook for future work has been developed in section 7.2.

7.1 Summary of results

The results obtained in this thesis give further information about the behaviour of sub-200 nm gold nanoparticles subject to dielectrophoresis.

In Chapter 3, spectroscopy methods were detailed, with a focus on light scattering spectroscopy. First, the stability of particles in solution was analysed as a function of the composition of the buffer solution. Secondly, bio-molecular recognition was determined for biotin- coated gold nanoparticle and terbium labelled streptavidin. Using photolminescence spectroscopy it was demonstrated that the interaction between biotin and streptavidin is operational in this system, but does not lead to the formation of multi-particle aggregates. (see Figure 7.1)

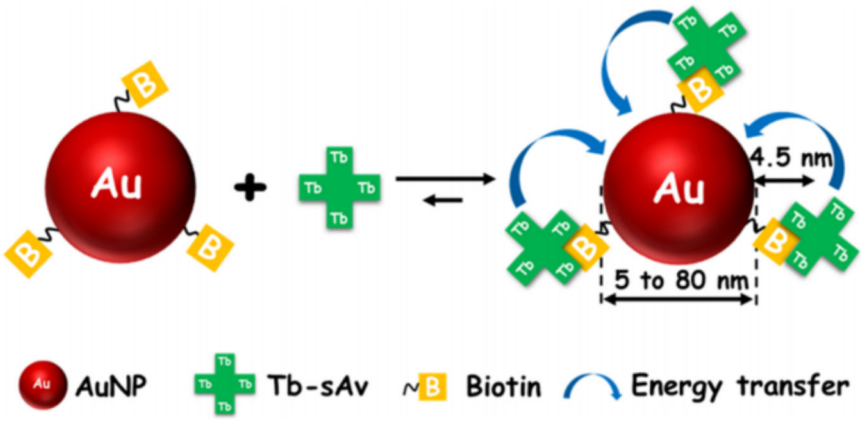

Figure. 7.1 Schematic representation (not to scale) of the assemblies of Tb-labeled sAv (Tb-sAv) and biotinylated AuNPs (biot-AuNPs), wherein excitation energy transfer occurs. A distance of 4.5 nm was estimated using a radius of 3 nm for sAv plus 1.5 nm for the biotin and linker attached to the AuNP.

In Chapter 4, the microfabrication of an electromicrofluidic system and its installation on an inverted microscope were explained. This was with the objective to manipulate gold nanoparticles in solution and to study their dielectrophoretic response in non-uniform electric field. We demonstrated good reproducibility in the microfabrication of ITO electrodes. Also, the system can be adapted to different types of microscopic contrast (fluorescence, dark field, transmitted light).

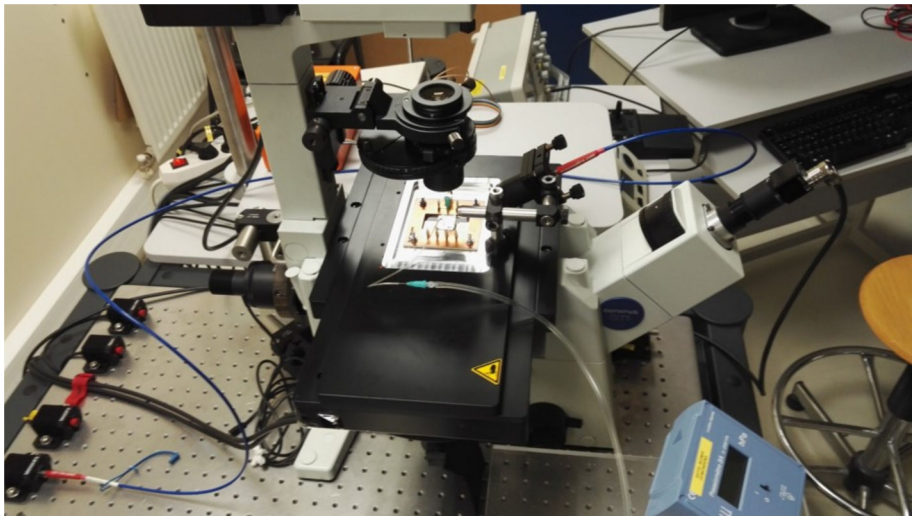

Figure. 7.2 Photo of the dielectrophoretic system mounted on the microscope system coupled to the image detection

In Chapter 5, we described the relation between Brownian motion and dielectrophoresis capture of small gold nanospheres ($\geq$ 80 nm diameter) in a microfluidic system using dark field videomicroscopy. The dielectrophoretic susceptibility was measured to depend linearly on particle diameter. This contrast with existing theoretical (and experimental) results on larger particles, where the dielectrophoretic susceptibility is expected to vary as the cube of the diameter. The dark-field microscopic method used in Chapter 5 was limited to gold particles with diameters of 80 nm and larger, due to the weak light scattering by smaller particles.

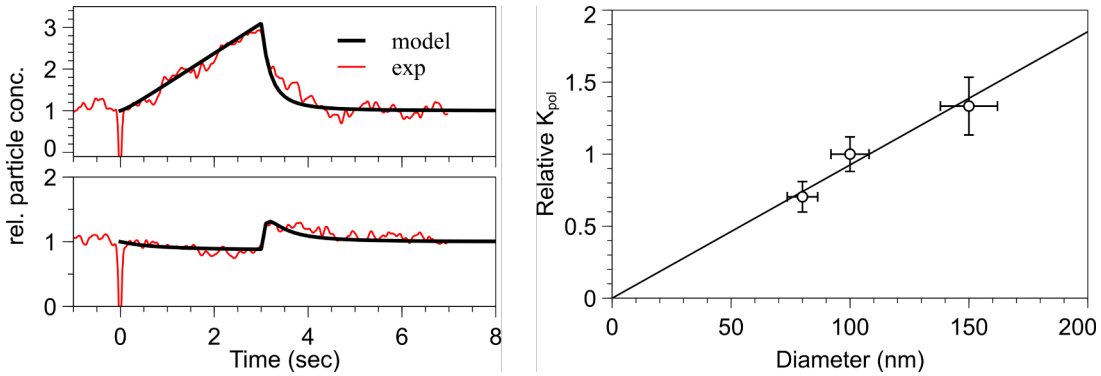

Figure. 7.3 (*left*) Time evolution of the particle concentration. Comparison of model (black) and experiment (red). Capture of 100 nm gold nanoparticles in water on the tip of electrode (*top*) and depletion in a ring just outside the capture zone (*bottom*). Experiment: amplitude 5 Vpp, theory: capture rate 0.8 s^{-1}. (*right*) Relative dielectrophoretic susceptibility K_{pol} as a function of gold nanoparticle diameter (circles). The K_{pol} values are relative to the value of 100 nm particles.

In Chapter 6, we used transmitted light and extinction micro spectroscopy to replace the dark field technique used in Chapter 5. This extends the range of size possibilities for gold nanoparticles (to below 80 m). The dielectrophoretic susceptibility was analysed and compared to the measurements of Chapter 5. Also, colloidal mixture was studied (mix of Au40 and Au80). This was the first demonstration of the possibility to discriminate two types of gold nanoparticle in a single solution using dielectrophoresis.

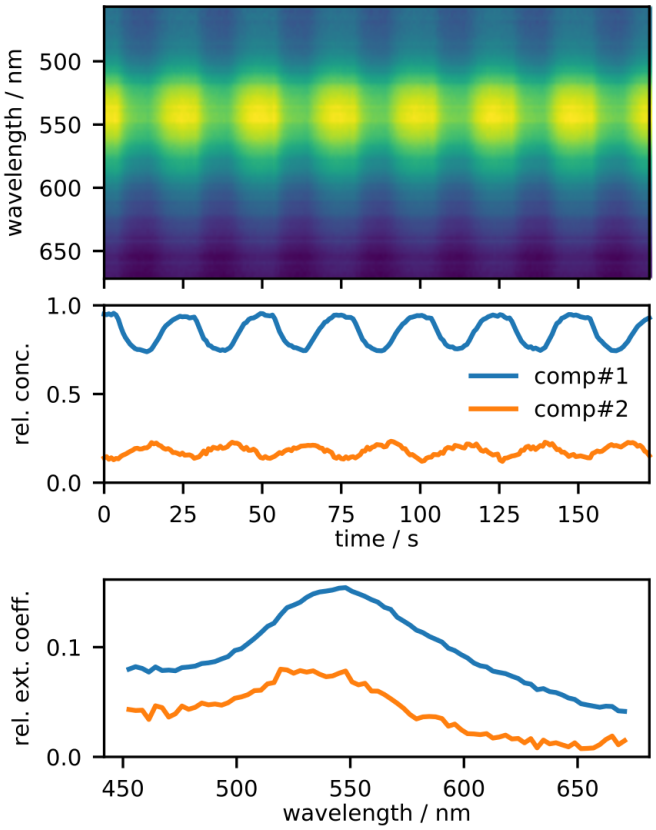

Figure. 7.4 (*top*) DEP-modulated extinction spectra of an aqueous dispersion of a mixture Au40-LA and Au80-LA (spectrotemporal recording). (*middle*) relative concentration traces for the two principal components reconstructed by target transformation from the singular value decomposition of the spectrotemporal matrix. (*bottom*) The corresponding extinction spectra. The reconstructed concentration traces and extinction spectra reproduce the recorded data.

7.2 Outlook: Future work

Despite the progress made in this thesis, there are still some unresolved questions. This section contains the main ideas for further investigations.

In Chapter 3, we showed an example for a potential bioanalytical detection scheme. This scheme may be used in a microfluidic system and improved by the application of selective dielectrophoresis.

The dielectrophoresis micro-system built in Chapter 4 can be improved by increasing the optical power of the light source and focusing it more tightly inside the microchannel. Here, a super-continuum laser would be an excellent tool. Also, the design of the electrodes can be changed to interdigitated electrodes. This will increase the area where dielectrophoretic capture will take place.

The results of Chapter 5 may be extended through measurements of gold nanoparticles in aqueous media of varying ionic strength and composition to make the connection to newly developed theoretical models.[188, 189] The contribution of surface conductance to the overall dielectrophoretic susceptibility may be expected to be negligible for conducting particles, further highlighting the expected importance of the diffuse part of the electric double layer in the DEP of nanoparticles. An interesting question is the interplay between the polarization of the highly conductive gold core and the polarization of the electric double layer. Also, the effect of different types of surface functionalisation of the gold nanoparticles needs investigation, as these will impact surface conductance and the structure of the electric double layer.

Finally in Chapter 6 we demonstrated the first results for the dielectrophoresis separation of a mixture of gold nanoparticles. It may now be possible to inject particles functionalised with biotin and mix it with a solution containing streptavidin in order to follow the formation of new assemblies and to distinguish all entities formed in solution.

It is possible to imagine a compact system for *in-vitro* diagnostics based on this dielectrophoresis separation. Gold nanoparticles with their sensitive optical responses are useful for such types of portable system.

There is potential for a system based on a mix of gold nanospheres and gold nanorods for example. This system is depicted in Figure 7.5.

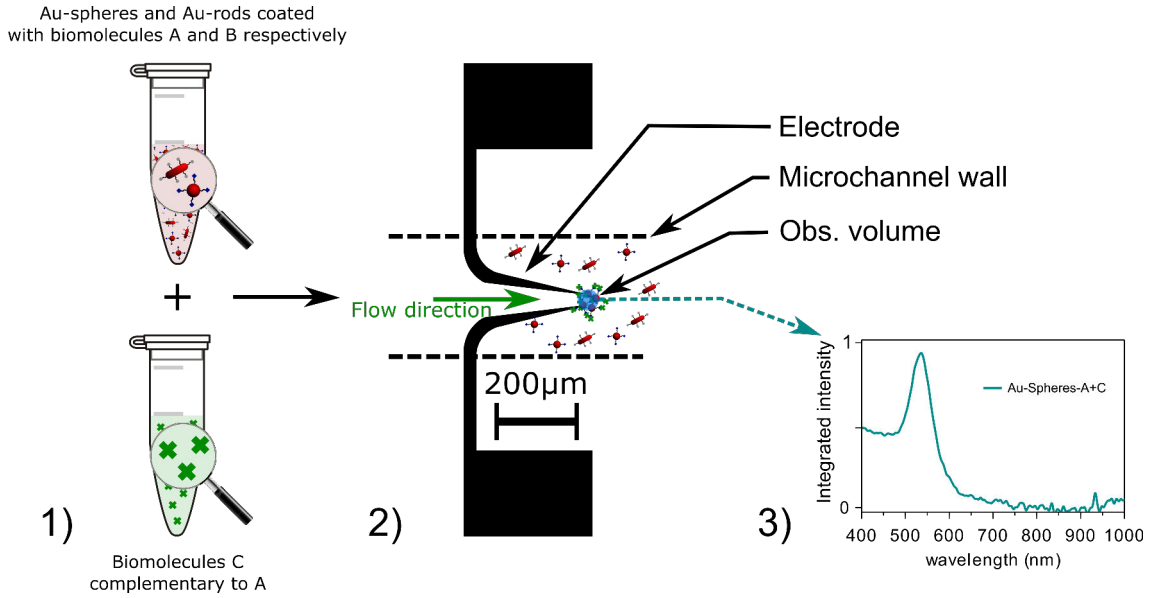

Figure. 7.5 (1) Schematic representation (not to scale) of the assemblies of AuNPs functionalised with biomolecules A and biomolecules B complementary to A. (2) Schematic top-view of the microfluidic channel and the capture area analysed by the spectrophotometer. Shows the selectivity of the capture as a function of the electric field parameters and affinities of particles coated with biomolecules (3) Extinction spectra of Au-Spheres-A+C capture using dielectrophoresis.

This thesis has described a first work on the dielectrophoretic susceptibility of sub 200 nm gold nanoparticles using videomicroscopy and spectroscopy detection in microfluidic channel and let a lot of capabilities and possibilities to use the electro-microfluidic system built.

References

[1] Herbert A. Pohl. The motion and precipitation of suspensoids in divergent electric fields. *Journal of Applied Physics*, 22:869–871, **1951**.

[2] Julien R G Navarro and Martinus H V Werts. Resonant light scattering spectroscopy of gold, silver and gold–silver alloy nanoparticles and optical detection in microfluidic channels. *Analyst*, 138:583–592, **2013**.

[3] Masatake Haruta. When Gold Is Not Noble: Catalysis by Nanoparticles. *The Chemical Record*, 3:75–87, **2003**.

[4] Yiwen Wang, Xueyi Xie, Xueding Wang, Geng Ku, Kelly L. Gill, D. Patrick O'Neal, George Stoica, and Lihong V. Wang. Photoacoustic Tomography of a Nanoshell Contrast Agent in the in Vivo Rat Brain. *Nano Letters*, 4:1689–1692, **2004**.

[5] Markus Zahn. Magnetic Fluid and Nanoparticle Applications to Nanotechnology. *Journal of Nanoparticle Research*, 3:73–78, **2001**.

[6] Selin Pıravadılı Mucur, Tülay Aslı Tumay, Sait Eren San, and Emine Tekin. Enhancing effects of nanoparticles on polymer-OLED performances. *Journal of Nanoparticle Research*, 14:1214, **2012**.

[7] Hana Šípová, Lei Shao, Nils Odebo Länk, Daniel Andrén, and Mikael Käll. Photothermal DNA Release from Laser-Tweezed Individual Gold Nanomotors Driven by Photon Angular Momentum. *ACS Photonics*, 5:2168–2175, **2018**.

[8] Stoyan K. Smoukov, Sumit Gangwal, Manuel Marquez, and Orlin D. Velev. Reconfigurable responsive structures assembled from magnetic Janus particles. *Soft Matter*, 5:1285, **2009**.

[9] E Palleau, N M Sangeetha, and L Ressier. Quantification of the electrostatic forces involved in the directed assembly of colloidal nanoparticles by AFM nanoxerography. *Nanotechnology*, 22:325603, **2011**.

[10] Cosmin Farcau, Neralagatta M. Sangeetha, Helena Moreira, Benoît Viallet, Jérémie Grisolia, Diana Ciuculescu-Pradines, and Laurence Ressier. High-Sensitivity Strain Gauge Based on a Single Wire of Gold Nanoparticles Fabricated by Stop-and-Go Convective Self-Assembly. *ACS Nano*, 5:7137–7143, **2011**.

[11] Pierre Moutet, Pierre Deram, Neralagatta M. Sangeetha, and Laurence Ressier. Dynamics of Dielectrophoretic-Force-Directed Assembly of $NaYF_4$ Colloidal Nanocrystals into Tunable Multilayered Micropatterns. *The Journal of Physical Chemistry Letters*, 5:2988–2993, **2014**.

[12] Claudia Irene Trainito, Olivier Français, and Bruno Le Pioufle. Monitoring the permeabilization of a single cell in a microfluidic device, through the estimation of its dielectric properties based on combined dielectrophoresis and electrorotation in situ experiments: Microfluidics and Miniaturization. *Electrophoresis*, 36:1115–1122, **2015**.

[13] Robert Schreiber, Jaekwon Do, Eva-Maria Roller, Tao Zhang, Verena J. Schüller, Philipp C. Nickels, Jochen Feldmann, and Tim Liedl. Hierarchical assembly of

metal nanoparticles, quantum dots and organic dyes using DNA origami scaffolds. *Nature Nanotechnology*, 9:74–78, **2014**.

[14] Asaf Salant, Ella Amitay-Sadovsky, and Uri Banin. Directed Self-Assembly of Gold-Tipped CdSe Nanorods. *Journal of the American Chemical Society*, 128:10006–10007, **2006**.

[15] Matthieu Loumaigne, Clyde Midelet, Tristan Doussineau, Philippe Dugourd, Rodolphe Antoine, Meriem Stamboul, Anne Débarre, and Martinus H. V. Werts. Optical extinction and scattering cross sections of plasmonic nanoparticle dimers in aqueous suspension. *Nanoscale*, 8:6555–6570, **2016**.

[16] J Yguerabide and E E Yguerabide. Light-scattering submicroscopic particles as highly fluorescent analogs and their use as tracer labels in clinical and biological applications. I. Theory. *Analytical biochemistry*, 262:157–176, **1998**.

[17] A Ramos, H Morgan, N G Green, and A Castellanos. Ac electrokinetics: a review of forces in microelectrode structures. *Journal of Physics D: Applied Physics*, 31:2338–2353, **1998**.

[18] Chuan Zhang, Robert J. Macfarlane, Kaylie L. Young, Chung Hang J. Choi, Liangliang Hao, Evelyn Auyeung, Guoliang Liu, Xiaozhu Zhou, and Chad A. Mirkin. A general approach to DNA-programmable atom equivalents. *Nature Materials*, 12:741–746, **2013**.

[19] L. Motte, F. Billoudet, E. Lacaze, J. Douin, and M. P. Pileni. Self-Organization into 2d and 3d Superlattices of Nanosized Particles Differing by Their Size. *The Journal of Physical Chemistry B*, 101:138–144, **1997**.

[20] Frank Caruso, editor. *Colloids and colloid assemblies: synthesis, modification, organization, and utilization of colloid particles*. Wiley-VCH, Weinheim, **2004**.

[21] Ying Guan and Yongjun Zhang. PNIPAM microgels for biomedical applications: from dispersed particles to 3d assemblies. *Soft Matter*, 7:6375, **2011**.

[22] Michael P. Hughes and Hywel Morgan. Dielectrophoretic trapping of single sub-micrometre scale bioparticles. *Journal of Physics D: Applied Physics*, **1998**.

[23] Adam F Chrimes, Aminuddin Kayani, Khashayar Khoshmanesh, Paul R Stoddart, Paul Mulvaney, Arnan Mitchell, and Kourosh Kalantar-Zadeh. Dielectrophoresis-Raman spectroscopy system for analysing suspended nanoparticles. *Lab on a chip*, 11:921–8, **2011**.

[24] Matthieu Loumaigne, Raïssa Praho, Daniele Nutarelli, Martinus H V Werts, and Anne Débarre. Fluorescence correlation spectroscopy reveals strong fluorescence quenching of FITC adducts on PEGylated gold nanoparticles in water and the presence of fluorescent aggregates of desorbed thiolate ligands. *Physical Chemistry Chemical Physics*, 12:11004, **2010**.

[25] Chia-Hung Chen, Adam R. Abate, Daeyeon Lee, Eugene M. Terentjev, and David A. Weitz. Microfluidic Assembly of Magnetic Hydrogel Particles with Uniformly Anisotropic Structure. *Advanced Materials*, 21:3201–3204, **2009**.

[26] K. Lance Kelly, Eduardo Coronado, Lin Lin Zhao, and George C. Schatz. The Optical Properties of Metal Nanoparticles: The Influence of Size, Shape, and Dielectric Environment. *The Journal of Physical Chemistry B*, 107:668–677, **2003**.

[27] G. Schmid and U. Simon. Gold nanoparticles: assembly and electrical properties in 1–3 dimensions. *Chem. Commun.*, 697–710, **2005**.

[28] Susie Eustis and Mostafa A. El-Sayed. Why gold nanoparticles are more precious than pretty gold: Noble metal surface plasmon resonance and its enhancement

of the radiative and nonradiative properties of nanocrystals of different shapes. *Chem. Soc. Rev.*, 35:209–217, **2006**.

[29] Simon Mostafa, Farzad Behafarid, Jason R. Croy, Luis K. Ono, Long Li, Judith C. Yang, Anatoly I. Frenkel, and Beatriz Roldan Cuenya. Shape-Dependent Catalytic Properties of Pt Nanoparticles. *Journal of the American Chemical Society*, 132:15714–15719, **2010**.

[30] Dayan Chlala, Madona Labaki, Jean-Marc Giraudon, Olivier Gardoll, Audrey Denicourt-Nowicki, Alain Roucoux, and Jean-François Lamonier. Toluene total oxidation over Pd and Au nanoparticles supported on hydroxyapatite. *Comptes Rendus Chimie*, 19:525–537, **2016**.

[31] Julien Gigault, Boris Pedrono, Benoît Maxit, and Alexandra Ter Halle. Marine plastic litter: the unanalyzed nano-fraction. *Environmental Science: Nano*, 3:346–350, **2016**.

[32] Y. Sun. Shape-Controlled Synthesis of Gold and Silver Nanoparticles. *Science*, 298:2176–2179, **2002**.

[33] Daniel L Feldheim and Colby A Foss. *Metal nanoparticles: synthesis, characterization, and applications.* **2002**.

[34] Catherine J. Murphy, Tapan K. Sau, Anand M. Gole, Christopher J. Orendorff, Jinxin Gao, Linfeng Gou, Simona E. Hunyadi, and Tan Li. Anisotropic Metal Nanoparticles: Synthesis, Assembly, and Optical Applications. *The Journal of Physical Chemistry B*, 109:13857–13870, **2005**.

[35] Calin Hrelescu, Tapan K. Sau, Andrey L. Rogach, Frank Jäckel, Guillaume Laurent, Ludovic Douillard, and Fabrice Charra. Selective Excitation of Individual

Plasmonic Hotspots at the Tips of Single Gold Nanostars. *Nano Letters*, 11:402–407, **2011**.

[36] Médéric Lequeux, Johan Grand, and Guillaume Laurent. Importance of Gold Nanorods' Aggregation in Surface Plasmon Coupling with a Photochromic Film in Hybrid Structures. *Plasmonics*, 10:1863–1868, **2015**.

[37] X. Hu, P. H. Bessette, J. Qian, C. D. Meinhart, P. S. Daugherty, and H. T. Soh. Marker-specific sorting of rare cells using dielectrophoresis. *Proceedings of the National Academy of Sciences*, 102:15757–15761, **2005**.

[38] Grant T.D. Shouldice, Gerald A. Vandezande, and Alfred Rudin. Practical aspects of the emulsifier-free emulsion polymerization of styrene. *European Polymer Journal*, 30:179–183, **1994**.

[39] Kar P. Lok and Christopher K. Ober. Particle size control in dispersion polymerization of polystyrene. *Canadian Journal of Chemistry*, 63:209–216, **1985**.

[40] Nida Qutub, Bilal Masood Pirzada, Khalid Umar, and Suhail Sabir. Synthesis of CdS nanoparticles using different sulfide ion precursors: Formation mechanism and photocatalytic degradation of Acid Blue-29. *Journal of Environmental Chemical Engineering*, 4:808–817, **2016**.

[41] Mathias Brust, Merryl Walker, Donald Bethell, David J. Schiffrin, and Robin Whyman. Synthesis of thiol-derivatised gold nanoparticles in a two-phase Liquid–Liquid system. *J. Chem. Soc., Chem. Commun.*, 0:801–802, **1994**.

[42] Haibing Xia, Shuo Bai, Jürgen Hartmann, and Dayang Wang. Synthesis of Monodisperse Quasi-Spherical Gold Nanoparticles in Water via Silver(I)-Assisted Citrate Reduction. *Langmuir*, 26:3585–3589, **2010**.

[43] Christoph Ziegler and Alexander Eychmüller. Seeded Growth Synthesis of Uniform Gold Nanoparticles with Diameters of 15-300 nm. *The Journal of Physical Chemistry C*, 115:4502–4506, **2011**.

[44] Robert J. Macfarlane, Matthew N. O'Brien, Sarah Hurst Petrosko, and Chad A. Mirkin. Nucleic Acid-Modified Nanostructures as Programmable Atom Equivalents: Forging a New "Table of Elements". *Angewandte Chemie International Edition*, 52:5688–5698, **2013**.

[45] Rajib Ghosh Chaudhuri and Santanu Paria. Core/Shell Nanoparticles: Classes, Properties, Synthesis Mechanisms, Characterization, and Applications. *Chemical Reviews*, 112:2373–2433, **2012**.

[46] Xiaoyong Lai, Jun Li, Brian A. Korgel, Zhenghong Dong, Zhenmin Li, Fabing Su, Jiang Du, and Dan Wang. General Synthesis and Gas-Sensing Properties of Multiple-Shell Metal Oxide Hollow Microspheres. *Angewandte Chemie International Edition*, 50:2738–2741, **2011**.

[47] Hye Hun Park, Kyoungja Woo, and Jae-Pyoung Ahn. Core–Shell Bimetallic Nanoparticles Robustly Fixed on the Outermost Surface of Magnetic Silica Microspheres. *Scientific Reports*, 3:1497, **2013**.

[48] Rijun Gui, Ajun Wan, and Hui Jin. Facile synthesis of quantum dots/mesoporous silica/quantum dots core/shell/shell hybrid microspheres for ratiometric fluorescence detection of 5-fluorouracil in human serum. *The Analyst*, 138:5956, **2013**.

[49] Numpon Insin, Joseph B. Tracy, Hakho Lee, John P. Zimmer, Robert M. Westervelt, and Moungi G. Bawendi. Incorporation of Iron Oxide Nanoparticles and Quantum Dots into Silica Microspheres. *ACS Nano*, 2:197–202, **2008**.

[50] Richard Hayes, Adham Ahmed, Tony Edge, and Haifei Zhang. Core–shell particles: Preparation, fundamentals and applications in high performance liquid chromatography. *Journal of Chromatography A*, 1357:36–52, **2014**.

[51] Feng Wang, Renren Deng, Juan Wang, Qingxiao Wang, Yu Han, Haomiao Zhu, Xueyuan Chen, and Xiaogang Liu. Tuning upconversion through energy migration in core–shell nanoparticles. *Nature Materials*, 10:968–973, **2011**.

[52] Domenico Cassano, Diego Rota Martir, Giovanni Signore, Vincenzo Piazza, and Valerio Voliani. Biodegradable hollow silica nanospheres containing gold nanoparticle arrays. *Chemical Communications*, 51:9939–9941, **2015**.

[53] M. A Hayat. *Colloidal gold: principles, methods, and applications. Volume 3*. Academic Press, San Diego, **1989**.

[54] Colin D. Bain, E. Barry Troughton, Yu Tai Tao, Joseph Evall, George M. Whitesides, and Ralph G. Nuzzo. Formation of monolayer films by the spontaneous assembly of organic thiols from solution onto gold. *Journal of the American Chemical Society*, 111:321–335, **1989**.

[55] Fajun Zhang, Maximilian W. A. Skoda, Robert M. J. Jacobs, Stefan Zorn, Richard A. Martin, Christopher M. Martin, Graham F. Clark, Günter Goerigk, and Frank Schreiber. Gold Nanoparticles Decorated with Oligo(ethylene glycol) Thiols: Protein Resistance and Colloidal Stability. *The Journal of Physical Chemistry A*, 111:12229–12237, **2007**.

[56] Jie Gao, Xiangyi Huang, Heng Liu, Feng Zan, and Jicun Ren. Colloidal Stability of Gold Nanoparticles Modified with Thiol Compounds: Bioconjugation and Application in Cancer Cell Imaging. *Langmuir*, 28:4464–4471, **2012**.

[57] B. T. Holland. Synthesis of Macroporous Minerals with Highly Ordered Three-Dimensional Arrays of Spheroidal Voids. *Science*, 281:538–540, **1998**.

[58] Chunlei Wang, Juntao Yan, Xuejun Cui, Dengli Cong, and Hongyan Wang. Preparation and characterization of magnetic hollow PMMA nanospheres via in situ emulsion polymerization. *Colloids and Surfaces A: Physicochemical and Engineering Aspects*, 363:71–77, **2010**.

[59] Kathryn M. L. Taylor, Jason S. Kim, William J. Rieter, Hongyu An, Weili Lin, and Wenbin Lin. Mesoporous Silica Nanospheres as Highly Efficient MRI Contrast Agents. *Journal of the American Chemical Society*, 130:2154–2155, **2008**.

[60] N. Wartenberg, O. Raccurt, D. Imbert, M. Mazzanti, and E. Bourgeat-Lami. Luminescent latex particles loaded with anionic lanthanide complexes: a versatile platform for multicolour optical coding. *Journal of Materials Chemistry C*, 1:2061, **2013.**

[61] Gilles Bosma, Chellapah Pathmamanoharan, Els H.A. de Hoog, Willem K. Kegel, Alfons van Blaaderen, and Henk N.W. Lekkerkerker. Preparation of Monodisperse, Fluorescent PMMA–Latex Colloids by Dispersion Polymerization. *Journal of Colloid and Interface Science*, 245:292–300, **2002**.

[62] Frédéric Grillot, Kiril Veselinov, Mariangela Gioannini, Ivo Montrosset, Jacky Even, Rozenn Piron, Estelle Homeyer, and Slimane Loualiche. Spectral Analysis of 1.55-µm InAs–InP(113)B Quantum-Dot Lasers Based on a Multipopulation Rate Equations Model. *IEEE Journal of Quantum Electronics*, 45:872–878, **2009**.

[63] Erol Kucur, Jürgen Riegler, Gerald A. Urban, and Thomas Nann. Determination of quantum confinement in CdSe nanocrystals by cyclic voltammetry. *The Journal of Chemical Physics*, 119:2333–2337, **2003**.

[64] Nurul I. Supiandi, G. Charron, M. Tharaud, L. Cordier, J.-M. Guigner, M. F. Benedetti, and Y. Sivry. Isotopically Labeled Nanoparticles at Relevant Concentrations: How Low Can We Go? The Case of CdSe/ZnS QDs in Surface Waters. *Environmental Science and Technology*, 53:2586–2594, **2019**.

[65] Surat Hotchandani and Prashant V. Kamat. Charge-transfer processes in coupled semiconductor systems. Photochemistry and photoelectrochemistry of the colloidal cadmium sulfide-zinc oxide system. *The Journal of Physical Chemistry*, 96:6834–6839, **1992**.

[66] Horst Weller. Quantized Semiconductor Particles: A novel state of matter for materials science. *Advanced Materials*, 5:88–95, **1993**.

[67] Tito Trindade, Paul O'Brien, and Nigel L. Pickett. Nanocrystalline Semiconductors: Synthesis, Properties, and Perspectives. *Chemistry of Materials*, 13:3843–3858, **2001**.

[68] W. Brown. *Dynamic Light Scattering: The method and some applications*. Clarendon Press, Oxford, **1993**.

[69] Bruce J. Berne and Robert Pecora. *Dynamic light scattering: with applications to chemistry, biology, and physics*. Dover Publications, Mineola, N.Y, dover ed edition, **2000**.

[70] R. Pasternack and P. Collings. Resonance light scattering: a new technique for studying chromophore aggregation. *Science*, 269:935–939, **1995**.

[71] Hind Al-Johani, Edy Abou-Hamad, Abdesslem Jedidi, Cory M. Widdifield, Jasmine Viger-Gravel, Shiv Shankar Sangaru, David Gajan, Dalaver H. Anjum, Samy Ould-Chikh, Mohamed Nejib Hedhili, Andrei Gurinov, Michael J. Kelly, Mohamad El Eter, Luigi Cavallo, Lyndon Emsley, and Jean-Marie Basset. The structure and binding mode of citrate in the stabilization of gold nanoparticles. *Nature Chemistry*, 9:890–895, **2017**.

[72] Herr Otto Stern. Zur theorie der elektrolytischen doppelschitcht. *Electrochem.*, 30, **1924**.

[73] Christian Pfeiffer, Christoph Rehbock, Dominik Hühn, Carolina Carrillo-Carrion, Dorleta Jimenez de Aberasturi, Vivian Merk, Stephan Barcikowski, and Wolfgang J. Parak. Interaction of colloidal nanoparticles with their local environment: the (ionic) nanoenvironment around nanoparticles is different from bulk and determines the physico-chemical properties of the nanoparticles. *Journal of The Royal Society Interface*, 11:20130931, **2014**.

[74] S. S. Dukhin, V. N. Shilov, and J. J. Bikerman. Dielectric Phenomena and Double Layer in Disperse Systems and Polyelectrolytes. *Journal of The Electrochemical Society*, 121:154C, **1974**.

[75] J. O'M Bockris and Amulya K. N. Reddy. *Modern electrochemistry: an introduction to an interdisciplinary area. Vol. 2: ...* Plenum Press, New York, 3. printing edition, **1977**.

[76] Robert J. Hunter. *Foundations of colloid science*. Oxford University Press, Oxford ; New York, 2nd ed edition, **2001**.

[77] E. J. W. Verwey. Theory of the Stability of Lyophobic Colloids. *The Journal of Physical and Colloid Chemistry*, 51:631–636, **1947**.

[78] B Derjaguin and L Landau. Theory of the stability of strongly charged lyophobic sols and of the adhesion of strongly charged particles in solutions of electrolytes. *Progress in Surface Science*, 43:30–59, **1993**.

[79] J. Wu, D. Bratko, and J. M. Prausnitz. Interaction between like-charged colloidal spheres in electrolyte solutions. *Proceedings of the National Academy of Sciences*, 95:15169–15172, **1998**.

[80] Jiashu Sun, Yunlei Xianyu, and Xingyu Jiang. Point-of-care biochemical assays using gold nanoparticle-implemented microfluidics. *Chem. Soc. Rev.*, 43:6239–6253, **2014**.

[81] Jean Perrin. Mouvement brownien et molécules. *Journal de Physique Théorique et Appliquée*, 9:5–39, **1910**.

[82] A. Hirlekar Schmid, S.E. Stanca, M.S. Thakur, K. Ravindranathan Thampi, and C. Raman Suri. Site-directed antibody immobilization on gold substrate for surface plasmon resonance sensors. *Sensors and Actuators B: Chemical*, 113:297–303, **2006**.

[83] Tobias Kraus, Laurent Malaquin, Heinz Schmid, Walter Riess, Nicholas D. Spencer, and Heiko Wolf. Nanoparticle printing with single-particle resolution. *Nature Nanotechnology*, 2:570–576, **2007**.

[84] Martinus H. V. Werts, Mathieu Lambert, Jean-Philippe Bourgoin, and Mathias Brust. Nanometer Scale Patterning of Langmuir-Blodgett Films of Gold Nanoparticles by Electron Beam Lithography. *Nano Letters*, 2:43–47, **2002**.

[85] Frank N. Crespilho, M. Emilia Ghica, Monica Florescu, Francisco C. Nart, Osvaldo N. Oliveira, and Christopher M.A. Brett. A strategy for enzyme immobilization on layer-by-layer dendrimer–gold nanoparticle electrocatalytic membrane

incorporating redox mediator. *Electrochemistry Communications*, 8:1665–1670, **2006**.

[86] Philip H. Jones, Onofrio M. Maragò, and Giovanni Volpe. *Optical tweezers: principles and applications*. Cambridge University Press, Cambridge, **2015**.

[87] Yeonee Seol, Amanda E. Carpenter, and Thomas T. Perkins. Gold nanoparticles: enhanced optical trapping and sensitivity coupled with significant heating. *Optics Letters*, 31:2429, **2006**.

[88] Karel Svoboda and Steven M. Block. Optical trapping of metallic Rayleigh particles. *Optics Letters*, 19:930, **1994**.

[89] Poul Martin Hansen, Vikram Kjøller Bhatia, Niels Harrit, and Lene Oddershede. Expanding the Optical Trapping Range of Gold Nanoparticles. *Nano Letters*, 5:1937–1942, **2005**.

[90] P. H. O'Farrell. High resolution two-dimensional electrophoresis of proteins. *The Journal of Biological Chemistry*, 250:4007–4021, **1975**.

[91] Xiaoyou Xu, K. Kenneth Caswell, Elizabeth Tucker, Saswat Kabisatpathy, K. Lisa Brodhacker, and Walter A. Scrivens. Size and shape separation of gold nanoparticles with preparative gel electrophoresis. *Journal of Chromatography A*, 1167:35–41, **2007**.

[92] Matthias Hanauer, Sebastien Pierrat, Inga Zins, Alexander Lotz, and Carsten Sönnichsen. Separation of Nanoparticles by Gel Electrophoresis According to Size and Shape. *Nano Letters*, 7:2881–2885, **2007**.

[93] T. Pellegrino, R. A. Sperling, A. P. Alivisatos, and W. J. Parak. Gel Electrophoresis of Gold-DNA Nanoconjugates. *Journal of Biomedicine and Biotechnology*, 2007:1–9, **2007**.

[94] Robert Kretschmer and Wolfgang Fritzsche. Pearl Chain Formation of Nanoparticles in Microelectrode Gaps by Dielectrophoresis. *Langmuir*, 20:11797–11801, **2004**.

[95] Dongqing Li. *Electrokinetics in microfluidics*. Number 2 in Interface science and technology. Elsevier/Academic Press, Amsterdam, 1. ed edition, **2004**.

[96] Martin Z. Bazant and Todd M. Squires. Induced-Charge Electrokinetic Phenomena: Theory and Microfluidic Applications. *Physical Review Letters*, 92:066101, **2004**.

[97] Todd M. Squires and Martin Z. Bazant. Induced-charge electro-osmosis. *Journal of Fluid Mechanics*, 509:217–252, **2004**.

[98] Hope C. Feldman, Marin Sigurdson, and Carl D. Meinhart. AC electrothermal enhancement of heterogeneous assays in microfluidics. *Lab on a Chip*, 7:1553, **2007**.

[99] Martin Pumera, Joseph Wang, Eli Grushka, and Ronen Polsky. Gold Nanoparticle-Enhanced Microchip Capillary Electrophoresis. *Analytical Chemistry*, 73:5625–5628, **2001**.

[100] Clyde Midelet, Bruno Le Pioufle, and Martinus H. V. Werts. Brownian motion and large electric polarizabilities facilitate dielectrophoretic capture of sub-200 nm gold nanoparticles in water. *ChemPhysChem*, **2019**.

[101] RH Muller and GE Hildebrand. Zetapotential und Partikelladung in der Laborpraxis(Einführung in die Theorie praktische Messdurchführung Dateninterpretation). *Paperback APV*, **1996**.

[102] M. Trau, D. A. Saville, and I. A. Aksay. Assembly of Colloidal Crystals at Electrode Interfaces. *Langmuir*, 13:6375–6381, **1997**.

[103] N G Green, A Ramos, and H Morgan. Ac electrokinetics: a survey of sub-micrometre particle dynamics. *Journal of Physics D: Applied Physics*, 33:632–641, **2000**.

[104] N. G. Green, A. Ramos, A. González, H. Morgan, and A. Castellanos. Fluid flow induced by nonuniform ac electric fields in electrolytes on microelectrodes. I. Experimental measurements. *Physical Review E*, 61:4011–4018, **2000**.

[105] Hywel Morgan and Nicolas G Green. *AC electrokinetics: colloids and nanoparticles*. Number 2 in Microtechnologies and microsystems series. Research Studies Press, Baldock, **2003**.

[106] A Castellanos and A Ramos. Electrohydrodynamics and dielectrophoresis in microsystems: scaling laws. *Journal of Physics D: Applied Physics*, 2584, **2003**.

[107] J. B. Hasted, D. M. Ritson, and C. H. Collie. Dielectric Properties of Aqueous Ionic Solutions. Parts I and II. *The Journal of Chemical Physics*, 16:1–21, **1948**.

[108] J. H. Ambrus, C. T. Moynihan, and P. B. Macedo. Conductivity relaxation in a concentrated aqueous electrolyte solution. *The Journal of Physical Chemistry*, 76:3287–3295, **1972**.

[109] Johannes Hunger, Alexander Stoppa, Simon Schrödle, Glenn Hefter, and Richard Buchner. Temperature Dependence of the Dielectric Properties and Dynamics of Ionic Liquids. *ChemPhysChem*, 10:723–733, **2009**.

[110] N. G. Green, A. Ramos, A. González, H. Morgan, and A. Castellanos. Fluid flow induced by nonuniform ac electric fields in electrolytes on microelectrodes. III. Observation of streamlines and numerical simulation. *Physical Review E*, 66:026305, **2002**.

[111] S Loire, P Kauffmann, I Mezić, and C D Meinhart. A theoretical and experimental study of ac electrothermal flows. *Journal of Physics D: Applied Physics*, 45:185301, **2012**.

[112] Antonio Ramos, Hywel Morgan, Nicolas G Green, and Antonio Castellanos. AC Electric-Field-Induced Fluid Flow in Microelectrodes. *Journal of Colloid and Interface Science*, 217:420–422, **1999**.

[113] Nicolas G. Green, Antonio Ramos, Antonio González, Antonio Castellanos, and Hywel Morgan. Electrothermally induced fluid flow on microelectrodes. *Journal of Electrostatics*, 53:71–87, **2001**.

[114] Jonghyun Oh, Robert Hart, Jorge Capurro, and Hongseok (Moses) Noh. Comprehensive analysis of particle motion under non-uniform AC electric fields in a microchannel. *Lab Chip*, 9:62–78, **2009**.

[115] M. H. V. Werts, Florent Allix, Olivier Français, Céline Frochot, Laurent Griscom, Bruno Le Pioufle, Matthieu Loumaigne, and Johanna Midelet. Manipulation and Optical Detection of Colloidal Functional Plasmonic Nanostructures in Microfluidic Systems. *IEEE Journal of Selected Topics in Quantum Electronics*, 20:102–114, **2014**.

[116] B. G. Dick and A. W. Overhauser. Theory of the Dielectric Constants of Alkali Halide Crystals. *Physical Review*, 112:90–103, **1958**.

[117] Gustav Mie. Beiträge zur Optik trüber Medien, speziell kolloidaler Metallösungen. *Annalen der Physik*, 330:377–445, **1908**.

[118] John M. Steinke and A. P. Shepherd. Comparison of Mie theory and the light scattering of red blood cells. *Applied Optics*, 27:4027, **1988**.

[119] Prashant K. Jain, Kyeong Seok Lee, Ivan H. El-Sayed, and Mostafa A. El-Sayed. Calculated Absorption and Scattering Properties of Gold Nanoparticles of Different Size, Shape, and Composition: Applications in Biological Imaging and Biomedicine. *The Journal of Physical Chemistry B*, 110:7238–7248, **2006**.

[120] Johanna Midelet, Afaf H. El-Sagheer, Tom Brown, Antonios G. Kanaras, Anne Débarre, and Martinus H. V. Werts. Spectroscopic and Hydrodynamic Characterisation of DNA-Linked Gold Nanoparticle Dimers in Solution using Two-Photon Photoluminescence. *ChemPhysChem*, 19:827–836, **2018**.

[121] Gj Deželić and J. P. Kratohvil. Determination of size of small particles by light scattering. experiments on ludox colloidal silica. *Kolloid-Zeitschrift*, 173:38–48, **1960**.

[122] Kadir Aslan, Claudia C. Luhrs, and Víctor H. Pérez-Luna. Controlled and Reversible Aggregation of Biotinylated Gold Nanoparticles with Streptavidin. *The Journal of Physical Chemistry B*, 108:15631–15639, **2004**.

[123] B. Devika Chithrani and Warren C. W. Chan. Elucidating the Mechanism of Cellular Uptake and Removal of Protein-Coated Gold Nanoparticles of Different Sizes and Shapes. *Nano Letters*, 7:1542–1550, **2007**.

[124] Anup K. Pramanik, Siddikuzzaman, Duraippandi Palanimuthu, Kumaravel Somasundaram, and Ashoka G. Samuelson. Biotin Decorated Gold Nanoparticles for Targeted Delivery of a Smart-Linked Anticancer Active Copper Complex: In Vitro and In Vivo Studies. *Bioconjugate Chemistry*, 27:2874–2885, **2016**.

[125] Kae Sato, Kazuo Hosokawa, and Mizuo Maeda. Characterizing the non-crosslinked aggregation of DNA-modified gold nanoparticles: effects of DNA length and terminal base pair. *The Analyst*, 144:5580–5588, **2019**.

[126] K. Ouhenia-Ouadahi, R. Yasukuni, P. Yu, G. Laurent, C. Pavageau, J. Grand, J. Guérin, A. Léaustic, N. Félidj, J. Aubard, K. Nakatani, and R. Métivier. Photochromic–fluorescent–plasmonic nanomaterials: towards integrated three-component photoactive hybrid nanosystems. *Chem. Commun.*, 50:7299–7302, **2014**.

[127] Yu, Ser-Sing Chang, Chien-Liang Lee, and C. R. Chris Wang. Gold Nanorods: Electrochemical Synthesis and Optical Properties. *The Journal of Physical Chemistry B*, 101:6661–6664, **1997**.

[128] Babak Nikoobakht and Mostafa A. El-Sayed. Preparation and Growth Mechanism of Gold Nanorods (NRs) Using Seed-Mediated Growth Method. *Chemistry of Materials*, 15:1957–1962, **2003**.

[129] Wafa Abidi, P. R. Selvakannan, Yanick Guillet, Isabelle Lampre, Patricia Beaunier, Brigitte Pansu, Bruno Palpant, and Hynd Remita. One-Pot Radiolytic Synthesis of Gold Nanorods and Their Optical Properties. *The Journal of Physical Chemistry C*, 114:14794–14803, **2010**.

[130] Matthias Thiele, Joanne Zi En Soh, Andrea Knauer, Daniell Malsch, Ondrej Stranik, Robert Müller, Andrea Csáki, Thomas Henkel, J. Michael Köhler, and Wolfgang Fritzsche. Gold nanocubes – Direct comparison of synthesis approaches reveals the need for a microfluidic synthesis setup for a high reproducibility. *Chemical Engineering Journal*, 288:432–440, **2016**.

[131] P. Weber, D. Ohlendorf, J. Wendoloski, and F. Salemme. Structural origins of high-affinity biotin binding to streptavidin. *Science*, 243:85–88, **1989**.

[132] H. Grubm ller, B. Heymann, and P. Tavan. Ligand Binding: Molecular Mechanics Calculation of the Streptavidin-Biotin Rupture Force. *Science*, 271:997–999, **1996**.

[133] Oya Tagit and Niko Hildebrandt. Fluorescence Sensing of Circulating Diagnostic Biomarkers Using Molecular Probes and Nanoparticles. *ACS Sensors*, 2:31–45, **2017**.

[134] D. Duret, Z. Haftek-Terreau, M. Carretier, T. Berki, C. Ladavière, K. Monier, P. Bouvet, J. Marvel, Y. Leverrier, M.-T. Charreyre, and A. Favier. Labeling of native proteins with fluorescent RAFT polymer probes: application to the detection of a cell surface protein using flow cytometry. *Polymer Chemistry*, 9:1857–1868, **2018**.

[135] Julien R G Navarro, Marcel Plugge, Matthieu Loumaigne, Angel Sanchez-Gonzalez, Benedetta Mennucci, Anne Débarre, Albert M Brouwer, and Martinus H V Werts. Probing the interactions between disulfide-based ligands and gold nanoparticles using a functionalised fluorescent perylene-monoimide dye. *Photochemical and Photobiological Sciences*, 9:1042, **2010**.

[136] N. Nerambourg, R. Praho, M.H.V. Werts, D. Thomas, and M. Blanchard Desce. Hydrophilic monolayer-protected gold nanoparticles and their functionalisation with fluorescent chromophores. *International Journal of Nanotechnology*, 5:722, **2008**.

[137] Tao Huang and Royce W. Murray. Quenching of $[Ru(bpy)_3]^{2+}$ Fluorescence by Binding to Au Nanoparticles. *Langmuir*, 18:7077–7081, **2002**.

[138] P R Selvin and J E Hearst. Luminescence energy transfer using a terbium chelate: improvements on fluorescence energy transfer. *Proceedings of the National Academy of Sciences*, 91:10024–10028, **1994**.

[139] W A Hendrickson, A Pähler, J L Smith, Y Satow, E A Merritt, and R P Phizackerley. Crystal structure of core streptavidin determined from multiwavelength anomalous diffraction of synchrotron radiation. *Proceedings of the National Academy of Sciences of the United States of America*, 86:2190–4, **1989**.

[140] Sujit Kumar Ghosh and Tarasankar Pal. Interparticle Coupling Effect on the Surface Plasmon Resonance of Gold Nanoparticles: From Theory to Applications. *Chemical Reviews*, 107:4797–4862, **2007**.

[141] M.N. Berberan-Santos, E.N. Bodunov, and B. Valeur. Mathematical functions for the analysis of luminescence decays with underlying distributions 1. Kohlrausch decay function (stretched exponential). *Chemical Physics*, 315:171–182, **2005**.

[142] D. C. Johnston. Stretched exponential relaxation arising from a continuous sum of exponential decays. *Physical Review B*, 74:184430, **2006**.

[143] J. M. Zwier, G. J. Van Rooij, J. W. Hofstraat, and G. J. Brakenhoff. Image calibration in fluorescence microscopy. *Journal of Microscopy*, 216:15–24, **2004**.

[144] Matthew Newville, Antonino Ingargiola, Till Stensitzki, and Daniel B. Allen. *LMFIT: Non-Linear Least-Square Minimization and Curve-Fitting for Python.* **2014**.

[145] T. L. Jennings, J. C. Schlatterer, M. P. Singh, N. L. Greenbaum, and G. F. Strouse. NSET Molecular Beacon Analysis of Hammerhead RNA Substrate Binding and Catalysis. *Nano Letters*, 6:1318–1324, **2006**.

[146] T. L. Jennings, M. P. Singh, and G. F. Strouse. Fluorescent Lifetime Quenching near d = 1.5 nm Gold Nanoparticles: Probing NSET Validity. *Journal of the American Chemical Society*, 128:5462–5467, **2006**.

[147] Yan Chen, Meghan B. O'Donoghue, Yu-Fen Huang, Huaizhi Kang, Joseph A. Phillips, Xiaolan Chen, M.-Carmen Estevez, Chaoyong J. Yang, and Weihong Tan. A Surface Energy Transfer Nanoruler for Measuring Binding Site Distances on Live Cell Surfaces. *Journal of the American Chemical Society*, 132:16559–16570, **2010**.

[148] Xia Zhang, Cristian A. Marocico, Manuela Lunz, Valerie A. Gerard, Yurii K. Gun'Ko, Vladimir Lesnyak, Nikolai Gaponik, Andrei S. Susha, Andrey L. Rogach, and A. Louise Bradley. Wavelength, concentration, and distance dependence of nonradiative energy transfer to a plane of gold nanoparticles. *ACS Nano*, 6:9283–9290, **2012**.

[149] Suraj Saraswat, Anil Desireddy, Desheng Zheng, Lijun Guo, H. Peter Lu, Terry P. Bigioni, and Dragan Isailovic. Energy Transfer from Fluorescent Proteins to Metal Nanoparticles. *The Journal of Physical Chemistry C*, 115:17587–17593, **2011**.

[150] Anshika Kapur, Fadi Aldeek, Xin Ji, Malak Safi, Wentao Wang, Ada Del Cid, Oliver Steinbock, and Hedi Mattoussi. Self-Assembled Gold Nanoparticle–Fluorescent Protein Conjugates as Platforms for Sensing Thiolate Compounds via Modulation of Energy Transfer Quenching. *Bioconjugate Chemistry*, 28:678–687, **2017**.

[151] Ming Li, Scott K. Cushing, Qiaoyi Wang, Xiaodong Shi, Lawrence A. Hornak, Zhanglian Hong, and Nianqiang Wu. Size-Dependent Energy Transfer between

CdSe/ZnS Quantum Dots and Gold Nanoparticles. *The Journal of Physical Chemistry Letters*, 2:2125–2129, **2011**.

[152] Wenjuan Guo, Yanhong Wei, Zhao Dai, Guangping Chen, Yuanyuan Chu, and Yifei Zhao. Nanostructure and Corresponding Quenching Efficiency of Fluorescent DNA Probes. *Materials*, 11:272, **2018**.

[153] Igor Medintz and Niko Hildebrandt. *FRET - Förster Resonance Energy Transfer*. Wiley-VCH Verlag GmbH and Co. KGaA, Weinheim, Germany, **2013**.

[154] A del Campo and C Greiner. SU-8: a photoresist for high-aspect-ratio and 3d submicron lithography. *Journal of Micromechanics and Microengineering*, 17:R81–R95, **2007**.

[155] Dong Qin, Younan Xia, and George M Whitesides. Soft lithography for micro- and nanoscale patterning. *Nature Protocols*, 5:491–502, **2010**.

[156] Martinus H V Werts, Vincent Raimbault, Matthieu Loumaigne, Laurent Griscom, Olivier Français, Julien R G Navarro, Anne Débarre, and Bruno Le Pioufle. Optical microscopy and spectroscopy of analyte-sensitive functionalized gold nanoparticles in microfluidic systems. *Proc. SPIE*, 8595, **2013**.

[157] C. Midelet, J.-Y. Lin, S. Tsang, C.-l. Sun, J. Midelet, A. G. Kanaras, B. Le Pioufle, O. Français, and M. H. V. Werts. Effects of biomolecules on the electrokinetics of colloidal nanoparticles in liquid suspension. *Proc. SPIE*, **2017**.

[158] F. G. Halaka. Dielectrophoretic dynamic light-scattering (DDLS) spectroscopy. *Proceedings of the National Academy of Sciences*, 100:10164–10169, **2003**.

[159] Gerard H. Markx, Juliette Rousselet, and Ronald Pethig. DEP-FFF: Field-Flow Fractionation Using Non-Uniform Electric Fields. *Journal of Liquid Chromatography and Related Technologies*, 20:2857–2872, **1997**.

[160] Y. Huang, X.B. Wang, F.F. Becker, and P.R. Gascoyne. Introducing dielectrophoresis as a new force field for field-flow fractionation. *Biophysical Journal*, 73:1118–1129, **1997**.

[161] Peter R.C. Gascoyne and Jody Vykoukal. Particle Separation by Dielectrophoresis. *Electrophoresis*, 23:1973–1983, **2002**.

[162] K. D. Hermanson, S. O. Lumsdon, J. P. Williams, E. W. Kaler, and O. D. Velev. Dielectrophoretic assembly of electrically functional microwires from nanoparticle suspensions. *Science*, 294:1082–1086, **2001**.

[163] Christian Leiterer, Steffen Berg, Antti Pekka Eskelinen, Andrea Csaki, Matthias Urban, Päivi Törmä, and Wolfgang Fritzsche. Assembling gold nanoparticle chains using an AC electrical field: Electrical detection of organic thiols. *Sensors and Actuators, B: Chemical*, 176:368–373, **2013**.

[164] Orlin D. Velev and Shalini Gupta. Materials Fabricated by Micro- and Nanoparticle Assembly - The Challenging Path from Science to Engineering. *Advanced Materials*, 21:1897–1905, **2009**.

[165] Nicolas G. Green and Hywel Morgan. Dielectrophoresis of Submicrometer Latex Spheres. 1. Experimental Results. *The Journal of Physical Chemistry B*, 103:41–50, **1999**.

[166] Ming Tzo Wei, Joseph Junio, and Daniel H. Ou-Yang. Direct measurements of the frequency-dependent dielectrophoresis force. *Biomicrofluidics*, 3:012003, **2009**.

[167] T. Honegger, K. Berton, E. Picard, and D. Peyrade. Determination of Clausius-Mossotti factors and surface capacitances for colloidal particles. *Applied Physics Letters*, 98:181906, **2011**.

[168] D J Bakewell and H Morgan. Quantifying dielectrophoretic collections of submicron particles on microelectrodes. *Measurement Science and Technology*, 15:254–266, **2004**.

[169] D J Bakewell. Modelling nanoparticle transport in dielectrophoretic microdevices using a Fourier–Bessel series and applications for data analysis. *Journal of Physics D: Applied Physics*, 44:085501, **2011**.

[170] Werner Ebeling and Igor M Sokolov. *Statistical Thermodynamics and Stochastic Theory of Nonequilibrium Systems*, volume 8 of *Series on Advances in Statistical Mechanics*. World Scientific, **2005**.

[171] Eric B. Cummings and Anup K. Singh. Dielectrophoresis in Microchips Containing Arrays of Insulating Posts: Theoretical and Experimental Results. *Analytical Chemistry*, 75:4724–4731, **2003**.

[172] Asuka Nakano, Tzu-Chiao Chao, Fernanda Camacho-Alanis, and Alexandra Ros. Immunoglobulin G and bovine serum albumin streaming dielectrophoresis in a microfluidic device. *Electrophoresis*, pages 2314–2322, **2011**.

[173] William Sutherland. LXXV. *A dynamical theory of diffusion for non-electrolytes and the molecular mass of albumin. The London, Edinburgh, and Dublin Philosophical Magazine and Journal of Science*, 9:781–785, **1905**.

[174] A. Einstein. Über die von der molekularkinetischen Theorie der Wärme geforderte Bewegung von in ruhenden Flüssigkeiten suspendierten Teilchen. *Annalen der Physik*, 322:549–560, **1905**.

[175] Johanna Midelet, Afaf H. El-Sagheer, Tom Brown, Antonios G. Kanaras, and Martinus H. V. Werts. The Sedimentation of Colloidal Nanoparticles in Solution

and Its Study Using Quantitative Digital Photography. *Particle and Particle Systems Characterization*, 34:1700095, **2017**.

[176] Jonathan E. Guyer, Daniel Wheeler, and James A. Warren. FiPy: Partial Differential Equations with Python. *Computing in Science and Engineering*, 11:6–15, **2009**.

[177] Laura Barsanti, Valtere Evangelista, Anna Maria Frassanito, Nicoletta Vesentini, Vincenzo Passarelli, and Paolo Gualtieri. Absorption microspectroscopy, theory and applications in the case of the photosynthetic compartment. *Micron*, 38:197–213, **2007**.

[178] Robert Byron Bird, Warren E. Stewart, and Edwin N. Lightfoot. *Transport phenomena*. Wiley, New York, rev. 2. ed edition, **2007**.

[179] Kwang W Oh, Kangsun Lee, Byungwook Ahn, and Edward P Furlani. Design of pressure-driven microfluidic networks using electric circuit analogy. *Lab on a chip*, 12:515–45, **2012**.

[180] Mattijs Koeberg, Martinus H. V. Werts, Hendrik J. van Ramesdonk, and Jan W. Verhoeven. Two-dimensional transient absorption spectroscopy using a streak camera for detection and singular value decomposition for data analysis. *EPA Newsletter*, 71:21–34, **2001**.

[181] Chi Chen, Clyde Midelet, Shashi Bhuckory, Niko Hildebrandt, and Martinus H. V. Werts. Nanosurface Energy Transfer from Long-Lifetime Terbium Donors to Gold Nanoparticles. *The Journal of Physical Chemistry C*, 122:17566–17574, **2018**.

[182] Jonathan Cottet, Alexandre Kehren, Soufian Lasli, Harald Lintel, François Buret, Marie Frénéa-Robin, and Philippe Renaud. Dielectrophoresis-assisted creation of

cell aggregates under flow conditions using planar electrodes. *Electrophoresis*, 40:1498–1509, **2019**.

[183] Kuo-Tang Liao and Chia-Fu Chou. Nanoscale Molecular Traps and Dams for Ultrafast Protein Enrichment in High-Conductivity Buffers. *Journal of the American Chemical Society*, 134:8742–8745, **2012**.

[184] Asuka Nakano and Alexandra Ros. Protein dielectrophoresis: Advances, challenges, and applications: Nanoanalysis. *Electrophoresis*, 34:1085–1096, **2013**.

[185] Leonardo Lesser-Rojas, Petra Ebbinghaus, Ganesh Vasan, Ming-Lee Chu, Andreas Erbe, and Chia-Fu Chou. Low-Copy Number Protein Detection by Electrode Nanogap-Enabled Dielectrophoretic Trapping for Surface-Enhanced Raman Spectroscopy and Electronic Measurements. *Nano Letters*, 14:2242–2250, **2014**.

[186] Ali Rohani, Bankim J. Sanghavi, Armita Salahi, Kuo-Tang Liao, Chia-Fu Chou, and Nathan S. Swami. Frequency-selective electrokinetic enrichment of biomolecules in physiological media based on electrical double-layer polarization. *Nanoscale*, 9:12124–12131, **2017**.

[187] Logeeshan Velmanickam, Michael Fondakowski, Ivan T. Lima, and Dharmakeerthi Nawarathna. Integrated dielectrophoretic and surface plasmonic platform for million-fold improvement in the detection of fluorescent events. *Biomicrofluidics*, 11:044115, **2017**.

[188] Sagnik Basuray and Hsueh-Chia Chang. Induced dipoles and dielectrophoresis of nanocolloids in electrolytes. *Physical Review E*, 75:060501, **2007**.

[189] Sagnik Basuray, Hsien-Hung Wei, and Hsueh-Chia Chang. Dynamic double layer effects on ac-induced dipoles of dielectric nanocolloids. *Biomicrofluidics*, 4:022801, **2010**.

Titre: Diélectrophorèse de nanoparticules en système microfluidique: étude par vidéo-microscopie numérique et application à l'analyse par spectroscopie optique

Mots clés: Diélectrophorèse, nanoparticules d'or, résonance plasmon, spectroscopie

Résumé: La manipulation de micro- et nano-particules en solution peut être réalisée grâce aux interactions de ces objets avec des champs électromagnétiques. La lumière ou bien encore les champs électriques continus (DC) ou alternatifs (AC) peuvent être utilisés. Dans le cas d'un champ électrique non uniforme appliqué entre deux électrodes séparées par quelques micromètres, des gradients de champs très intenses et localisés sont ainsi créés. Ces gradients de champ localisés au niveau des électrodes engendrent la création de mouvements de charges composant la solution (effets électro-hydrodynamique). Mais aussi des charges confinées au niveau des particules à l'interface liquide/solide. Les particules en suspension subissent alors une force attractive ou répulsive appelée diélectrophorèse. Cette force est décrite dans la littérature pour des particules isolantes de taille supérieure à 200 nm. Dans cette étude par détection optique (videomicroscopie par champ sombre ou spectroscopie en microfluidique) la gamme de taille de particules est élargie (40-150 nm) pour étudier leurs réponses diélectrophorètique. En effet la diélectrophorèse dépend de la taille des particules, de son environnement et des paramètres du champ appliqué (fréquence, amplitude, topologie) La diélectrophorèse est mise en compétition avec le mouvement Brownian pour des particules d'or d'aussi petites tailles. La réponse pour des nanoparticules d'or en solution alors connue, il est envisageable de faire varier les paramètres, comme l'environnement de la particule ou bien la complexité des systèmes étudiés.

Title: Dielectrophoresis of nanoparticles in microfluidic systems: investigation using digital video microscopy and application to optical spectroscopic analysis

Keywords: Dielectrophoresis, gold nanoparticles, plasmon resonance, spectroscopy

Abstract: The manipulation of micro- and nano-particles in solution can be achieved through the interactions of these objects with electromagnetic fields. Emitted light, continuous (DC) or alternating (AC) electric fields can be used. In the case of a non-uniform electric field applied between two electrodes separated by a few micrometers, very intense and localized field gradients are created. These field gradients localised close to the electrodes generates a motion of the mass solution (electro-hydrodynamic effects). The charges confined onto particles at the liquid/solid interface are also subjected to motion. Suspended particles undergo an attractive or repulsive force called dielectrophoresis. This force is described in the literature for insulating particles larger than 200 nm. In this study optical detection was used (dark field videomicroscopy or microfluidic spectroscopy) to expand the range of particle size (40-150 nm) and to study their dielectrophoretic responses. Indeed, the dielectrophoresis is dependent on the size of particles, their environment and the parameters of the applied electric field (frequency, amplitude, topology). The dielectrophoresis is in competition with the Brownian motion of these gold nanoparticles. By, knowing the dielectrophoretic response of these particles in solution, it is possible to vary parameters, such as the suspension composition of the particles or the complexity of the systems studied.